Study of External Kink Modes in Shaped HBT-EP Plasmas

Patrick J. Byrne

Submitted in partial fulfillment of the

requirements for the degree

of Doctor of Philosophy

in the Graduate School of Arts and Sciences

COLUMBIA UNIVERSITY

2017

ABSTRACT

Study of External Kink Modes in Shaped HBT-EP Plasmas

Patrick J. Byrne

The first study of magnetohydrodynamic (MHD) equilibria and external kink modes in shaped plasmas on the High Beta Tokamak - Extended Pulse (HBT-EP) is described. A new poloidal field coil and high-current, low-voltage capacitive power supply was designed and installed. The new coil significantly modifies the shape of the plasma cross section and provides a new research tool for the study of kink mode structure and control. When fully energized, the coil creates a magnetic separatrix, which defines the boundary between confined and unconfined plasma. The separatrix is set by a poloidal field null called an "X-point", which is on the inboard side of the torus, above the midplane. Several arrays of magnetic sensors observe and characterize the plasma equilibrium and the MHD fluctuations from kink modes. Free-boundary plasma equilibria are reconstructed using standard methods that minimize the mean-square error between the numerically reconstructed equilibria and various measurements. Reconstructions of shaped plasma equilibria show the creation of fully diverted plasmas with shaped outer boundaries. The reconstructions are confirmed by direct measurements using arrays of magnetic sensors and a moveable Langmuir probe to measure the outermost closed flux surface. Measurements of individual kink modes are obtained from the magnetic fluctuations using a technique known as biorthogonal decomposition. External kink modes that naturally arise in shaped plasmas are observed and described. The poloidal structure of modes in shaped plasmas are found to be similar to those that arise in circular plasmas, except near the X-point. The magnetic signature of kink modes on the surface of the plasma are calculated using the ideal MHD code DCON. For plasmas with an X-point, DCON shows a short-wavelength, low amplitude structure near the X-point. The code VALEN is used to calculate the perturbed magnetic field measured at the sensors due to the DCON mode at the plasma surface. VALEN includes the effects of sensor/plasma separation and eddy currents induced in conducting structures by rotation of the modes. Good agreement is found between the measured mode structures and the ideal kink mode structures calculated at the sensors by VALEN. A distributed array of forty active control coils was used to perturb the plasma equilibria, and for both shaped and circular equilibria, the structure of the response to the perturbation was found to be the same as the that of the dominant naturally occurring mode in that equilibrium. Finally, the magnitude of the plasma's response to applied

magnetic perturbations was found to be comparable between shaped and unshaped plasmas, even though separation between the sensors and the boundary of the shaped plasmas increases relative to circular plasmas with the same plasma current and radial positions. In addition to demonstrating a new research tool for study of kink modes on HBT-EP, this research demonstrates the importance of accurate electromagnetic calculations, including eddy currents, when comparing measured and predicted mode structure.

Contents

List of Figures

List of Tables

Acknowledgements

My time at Columbia has been a time of struggle and intellectual challenge, as well personal and intellectual growth. I owe a debt of gratitude to Professors Navratil and Mauel for their leadership and guidance of the lab through a time of difficulty for the field. Jeffrey Levesque has been an invaluable resource, first as senior graduate student sharing knowledge and experience, then as post-doc and later a staff scientist. He is the front line of management, keeping research on schedule and the grad students sane. Without the support of Nicholas Rivera and Jim Andrello, there would simply not be a functioning tokamak on which to perform research. Beyond that, such hardware intensive work would have been impossible without their constant consultation on mechanical and electronic issues that arose during the research. Jim Bialek of the Princeton Plasma Physics Lab performed the VALEN simulations on which much of the analysis in this thesis depends. The former students Qian Peng, Max Roberts, and Daisuke Shiraki all provided invaluable assistance to me during the research, to say nothing of their friendship. The support of my family and friends gave me the confidence to spend a quarter of my life chasing such an idealistic career path, and carried me through the hard times. I consider myself extremely lucky to have found work, with the DIII-D tokamak, that so thoroughly suits my skills and interests, and would like to thank Gerald Navratil for making me aware of the opportunity as I began my job search. This work was supported by US DOE Office of Fusion Energy Sciences Grant DE-FG02-86ER53222.

"There is a theory which states that if ever anyone discovers exactly what the Universe is for and why it is here, it will instantly disappear and be replaced by something even more bizarre and inexplicable.

There is another theory which states that this has already happened."

- Douglas Adams, The Restaurant at the End of the Universe

Chapter 1

Introduction

Energy is inextricably linked to the advancement of human welfare[1]. However, energy supplied through combustion of hydrocarbons creates pollution that degrades the health of millions, while the effect of carbon dioxide on climate threatens the food supply as well as the geography on which our urban centers are based. Furthermore, the supply of fossil fuels is fixed while consumption is growing exponentially. A scaleable, carbon-neutral, high energy-density solution is necessary[2].

Fusion energy may provide the solution to the long term problem of finding a carbon-neutral, cheap, reliable, and abundant power source[3]. The most easily achieved fusion reaction requires an isotope of hydrogen, tritium, that is not available naturally due to its short half life of 12 years. Fortunately it can be bred by bombarding commonly available lithium with neutrons. The other reactant, the hydrogen isotope deuterium, is abundantly available in quantities to last millenia, as does the lithium used to breed tritium. Unlike nuclear power generated by fission, a failure of control cannot lead to a runaway meltdown, and as a novel technology, it does not suffer from the mistrust attached to fission.

Thermonuclear fusion for weapons use was demonstrated in the 1950's, but achieving controlled, steady-state fusion reactions has been an outstanding problem for 60 years[4]. There are multiple approaches to solving this problem, that mostly fall in one of two categories. Either a steady state fusion reaction is sustained by confining the plasma fuel with magnetic fields, or pulsed reactions are generated by rapidly compressing fuel pellets. Among the magnetic confinement solutions, the tokamak concept is most developed and well-studied. A number of magnetic confinement experimental campaigns that generated significant fusion power have already concluded, as shown in

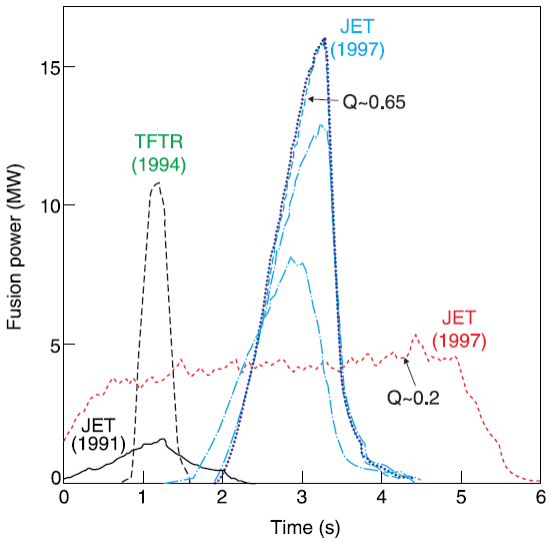

Figure 1.1: Fusion power obtained in historical Deuterium-Tritium discharges at the TFTR (US) and JET (UK/EU) tokamaks. Figure 7 in reference [6]. Q is the ratio of input heating power to fusion output power. Engineering efficiencies are not considered. The high power discharges are all limited by MHD instabilities, in particular edge localized modes.

Figure 1.1, and development continues with a $20 billion international experiment intended to study steady-state, reactor scale fusion plasmas under construction[5].

One of the major factors limiting the performance of a tokamak fusion reactor is magnetohydrodynamic (MHD) stability[6]. A class of MHD instabilities known as kinks, which are driven by the plasma current necessary for a tokamak plasma, create one of the strictest MHD limits on performance of a fusion plasma[7]. It has been understood for some time that creating a non-circular cross section plasma can affect the MHD stability[8], and all present and planned advanced tokamak experiments control the plasma cross section, both to enhance stability and to handle heat and plasma particle exhaust. With sufficient shaping, heat and particles leaving the confined region of a plasma can be preferentially exhausted away from sensitive instruments and diagnostics, and directed toward an area designed specifically to accept the heat and particle flux, known as a divertor[9, 10]. A diverted configuration arises naturally in high-performance plasmas[11], making the study of diverted tokamak equilibria highly relevant to magnetic confinement fusion studies.

1.1 Magnetic Plasma Confinement

1.1.1 Toroidal Geometry

The temperatures required for fusion are above one hundred million degrees Kelvin, a temperature far exceeding the melting point of any known material. There is therefore a need for a sharp temperature gradient between the core region of a fusion plasma and any nearby containing material. As the plasma is fully ionized at fusion temperatures, magnetic and electric fields can be used to apply forces at a distance, confining the plasma without physical contact. The equation of motion for a plasma fluid element is:

$$\rho \frac{d\vec{v}}{dt} = \vec{J} \times \vec{B} - \vec{\nabla} P \tag{1.1}$$

With ρ the mass density of the plasma element, $\vec{v}$ the velocity, P the pressure, $\vec{J}$ the current density, and $\vec{B}$ the magnetic field.

For the plasma to exist in a static equilibrium,

$$\vec{J} \times \vec{B} = \quad \vec{\nabla} P \tag{1.2}$$

and so

$$\vec{J} \cdot \vec{\nabla} P = \quad 0 \tag{1.3}$$

$$\vec{B} \cdot \vec{\nabla} P = \quad 0 \tag{1.4}$$

which requires that surfaces of constant pressure in a confined plasma volume be defined by non-aligned magnetic fields and currents tangent to those surfaces. As magnetic fields lie on constant pressure surfaces, poloidal flux Ψ integrated from the magnetic axis of the torus to a given surface of constant pressure will be a constant everywhere on the surface. Therefore the surfaces of constant pressure, as well as all other quantities that vary from the core to the edge, can be defined in terms of Ψ, which is often normalized to 0 at the magnetic axis of the plasma, and 1 at the last closed flux surface.

Transport of plasma along field lines, and thus along a surface, is much more rapid than transport across field lines, due to the Lorentz force acting on charged particles moving perpendicular to field

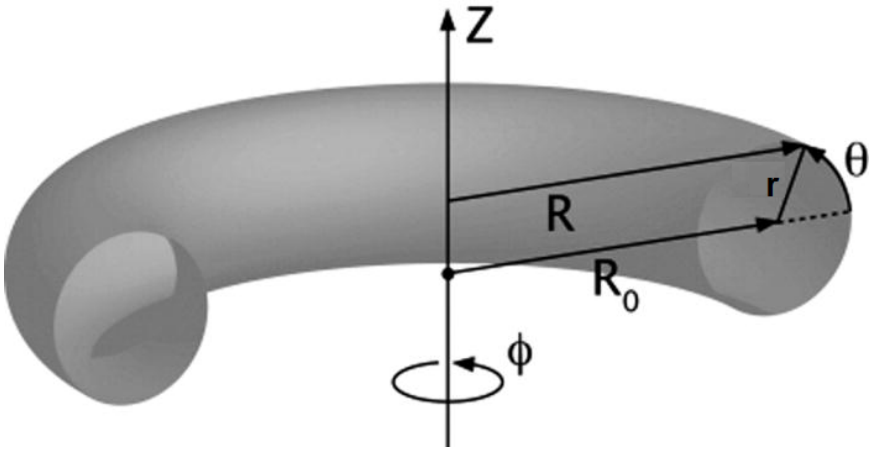

Figure 1.2: Essential features of toroidal geometry. Figure 1 in Reference [12].

lines. It is therefore important that field lines be prevented from intersecting a material surface, as rapid diffusion parallel to the field would transfer enough energy out of the plasma to quickly quench the discharge. A topologically toroidal surface allows arbitrarily long paths to be traced along it without ever leaving the surface.

Figure 1.2 shows the geometry of a toroidal system, with reference to a cylindrical coordinate system. In a toroidal coordinate system, the azimuthal angle ϕ is referred to as the toroidal direction, and R and Z are specified using the major radius, R_0, the minor radius, r, and the poloidal angle, θ.

Figure 1.3 shows how this magnetic geometry is created in a tokamak. A toroidal field (blue arrow in Figure 1.3) is imposed by external coils (blue coils), and a toroidal ring current (green arrow inside the pink plasma region) will be driven along the toroidal direction to create a poloidal field that links the toroidal current (green arrows, outside the plasma). The combination of the two fields trace helical paths that describe nested toroidal surfaces.

1.1.2 Positional Stability

Thermal pressure in the plasma column and the magnetic pressure differential between the inboard side of the plasma and the outboard side cause a toroidal plasma to expand along its major radius. If this expansion is not arrested, the plasma will grow until it collides with the container's walls, loses thermal energy, and neutralizes. This tendency is counteracted by a vertical poloidal field that forces the toroidal current radially inwards. The coils that provide this field are annotated in Figure

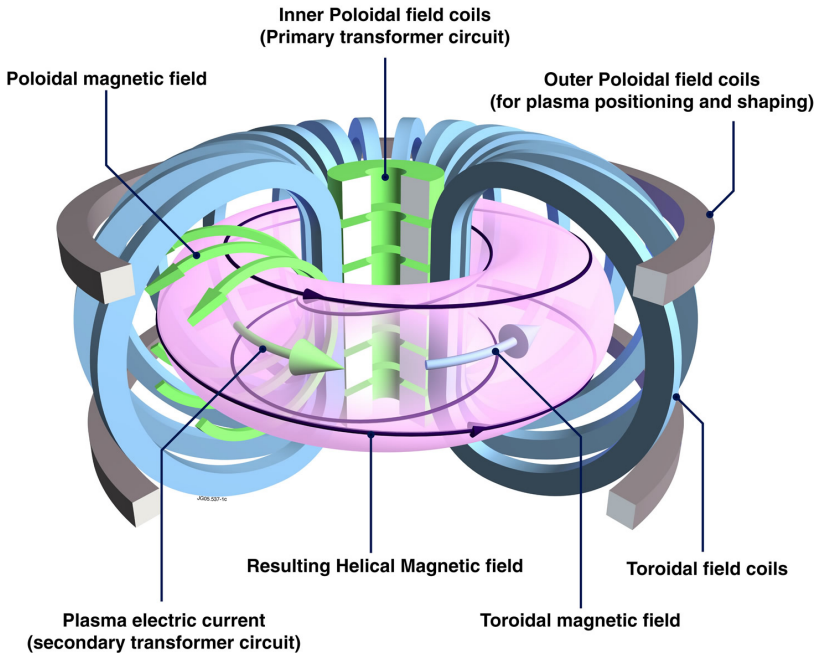

Figure 1.3: Schematic view of a typical tokamak plasma. Poloidal fields link the torus through the central hole, toroidal fields travel along the torus the long way. Four toroidal transits are completed in one poloidal transit in this diagram.
Credit: EUROfusion.

1.3.

As the plasma moves radially outward, the expansionary force will decrease. If the strength of the vertical field decays more slowly with radius than the expansionary force, the plasma will find a point where the forces equilibrate. If the vertical field is slightly curved, when the plasma column is displaced from the midplane it will feel a vertical force as it interacts with the radial component of the field (see Figure 1.4). An appropriate vertical field geometry stabilizes the plasma in the vertical direction as well as in the radial direction, and the figure of merit for this field geometry is known as the decay index, n.

$$n = -\frac{R}{B_Z}\frac{\partial B_Z}{\partial R} \tag{1.5}$$

The condition on the decay index for positional stability is[14]:

$$0 < n < 1.5 \tag{1.6}$$

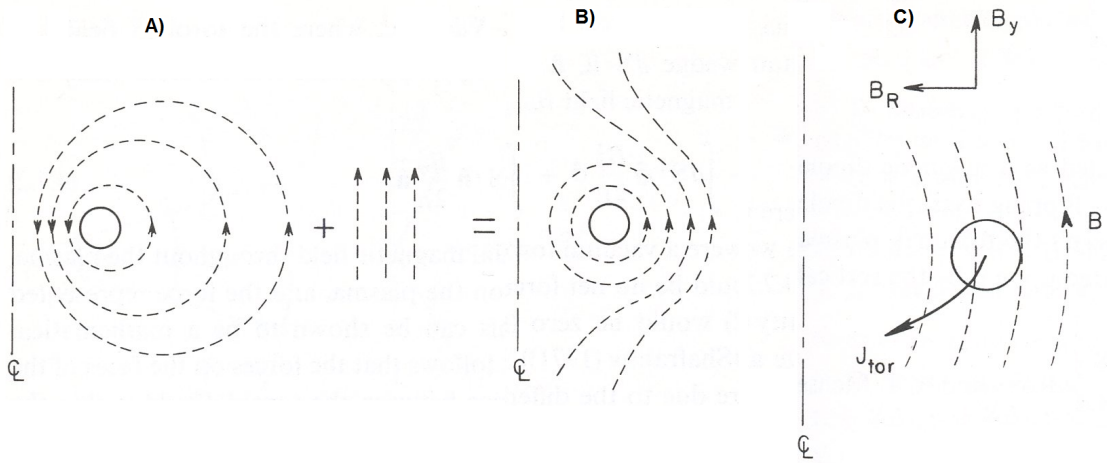

Figure 1.4: Figures 4.9 and 4.10 in reference [13] A) The flux surfaces of a toroidal loop of current. Note the greater magnetic pressure near the centerline (CL). B) The flux surfaces after introduction of a radially stabilizing vertical field. C) vertical Field curvature that provides vertical positional stability for toroidal plasma current.

Negative n denotes vertical instability, and $n > 1.5$ denotes a radial instability. In the event of instability, the plasma motion will be retarded by eddy currents induced by the motion of the current ring relative to conducting structures[15, 16]. This slowing can be significant, lengthening the growth of the instability enough for the discharge to be terminated in another manner.

1.1.3 Efficiency and β

The energy inputs required to generate the toroidal and poloidal fields establish a minimum condition on the efficient generation of fusion power. The figure of merit for energy generation in a fusion plasma is the value of the so called 'triple product'[17, 18]:

$$nT\tau_E \geq 5 * 10^{21} \frac{keV \cdot s}{m^3} \tag{1.7}$$

With n the plasma density, T the temperature, and τ_E the characteristic energy confinement time. Given that the triple product for power generation is dependent on density and temperature, confined pressure is a valuable figure of merit.

The efficient use of the magnetic field that confines the plasma is quantified as β, or the ratio of confined thermal plasma pressure p to the pressure of the confining magnetic pressure, $B^2/(2\mu_0)$. β

can be written with respect to either the toroidal or poloidal (or total) magnetic field:

$$\beta_t = \frac{\langle p \rangle}{B_t^2/2\mu_0} \tag{1.8}$$

$$\beta_p = \frac{\langle p \rangle}{\langle B_p \rangle^2/2\mu_0} \tag{1.9}$$

Where $\langle p \rangle$ is the volume averaged pressure, B_t is the toroidal magnetic field at the magnetic axis, $\langle B_p \rangle$ is the average poloidal field at the plasma surface. In a tokamak, B_t is much larger than B_p, so β_t is a good representation of the total β of a tokamak plasma. Fusion power density scales as $\langle p \rangle^2$, and therefore:

$$P_{fusion} \propto B^4 \beta^2 \tag{1.10}$$

β_t can be normalized[19] against the plasma current, I_p, the minor radius of the last closed flux surface a,

$$\beta_N = \frac{\beta_t a B_t}{I_p} \times 10^8 \tag{1.11}$$

A limit of $\beta_N \leq 3.5$ has been found empirically to be consistently achievable, though exceeding that limit is a topic of active research and high β plasmas with $\beta_N \sim 5$ have been achieved[20, 21]. Rewriting Eq. 1.11 using Eq. 1.10 gives

$$P_{fusion} \propto \frac{\beta_N^2 B_t^2}{a^2} I_P^2 \tag{1.12}$$

Given that β_N is limited, and that the toroidal field strength represents a cost that must be minimized, increasing I_P at the limit of β_N is the most direct way to increase the power output of a fusion plasma towards breakeven.

It is worth noting that with the imposition of a vertical field, the plasma poloidal field is strengthened on the outboard side, while it is reduced on the inboard side (Figure 1.4). If pressure is increased without an increase in plasma current, i.e. β_p is increased, a larger vertical field will be required to confine the plasma to a stable major radius, and the poloidal field strength on the inboard side of the plasma will be further reduced. Eventually, the inboard poloidal field will be completely canceled inside the vacuum vessel[11], at which point β_p cannot be increased further. This 'maximak'

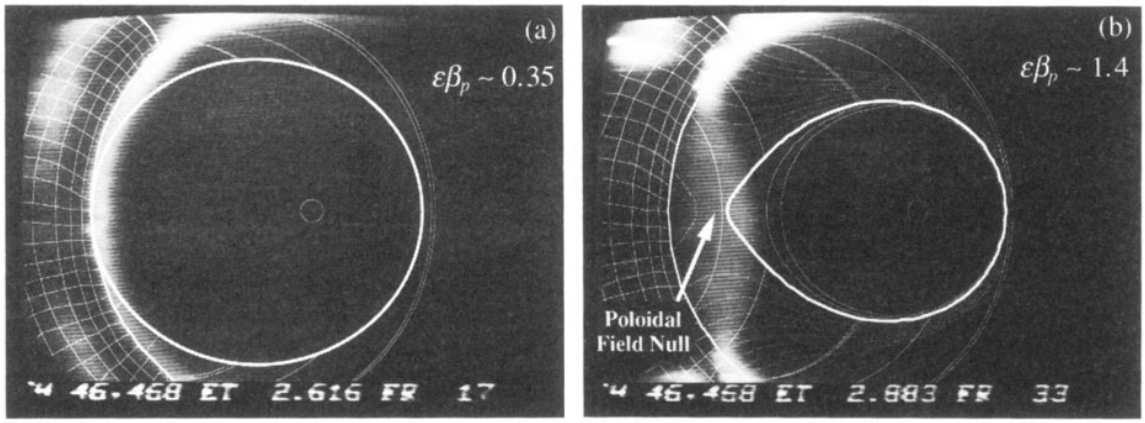

Figure 1.5: Figure 3 in reference [11]. Video still of the visible light emission, superimposed with the reconstructed LCFS, of two TFTR discharges. A) A low-β_p plasma in the TFTR tokamak. B) A plasma in which β_p has increased such that a naturally diverted plasma equilibrium has arisen.

configuration[14] (see Figure 1.5) suggests that diverted operation, or at least a non-circular cross section, can naturally result from generating a high-performance fusion plasma.

1.2 MHD Instabilities

If there exists a perturbation to the equilibrium quantities of a plasma that increases the free energy of the equilibrium, that perturbation will grow unless stopped by a non-linear damping mechanism, or until a disruption occurs. The eigenmodes of a perturbation can be represented as $\xi(r)e^{i(n\phi+m\theta+\omega t)}$, with ϕ the toroidal angle, θ the poloidal angle, ω the (complex) mode frequency, and $\xi(r)$ the radially dependent mode amplitude.

As β is increased, the MHD stability of the plasma will decrease until an MHD eigenmode is fully destabilized. There are different families of instabilities, but the form of the instability studied in this thesis is a helical kinking of the resonant flux surface of the plasma, seen in Figure 1.6. The MHD stability and structure of different eigenmodes throughout the cross section of a given plasma equilibrium can be calculated using ideal MHD stability codes, such as DCON[22, 23]. We restrict our focus throughout this thesis, both in measurement and simulation, to instabilities that distort the plasma edge, called external kink instabilities. HBT-EP is operated in a way that creates a broad current profile with a portion of the total current conducted in the edge region of the confined plasma volume. This type of current profile is more susceptible to external kink instabilites, and causes those instabilities to dominate the MHD physics.

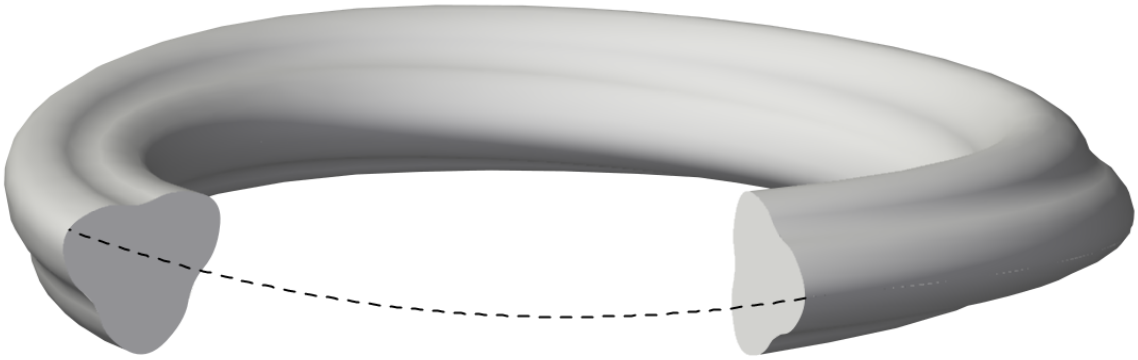

Figure 1.6: External kink deformation of a toroidal surface. The kink mode is characterized by a toroidal wave number $n = 1$, and a poloidal wave number $m = 3$.

1.2.1 Safety Factor

The helical twist of the field lines on a given surface is quantified by q, known in tokamak physics as the 'safety factor'. The safety factor is defined as the number of toroidal transits required for a field line to complete a single poloidal transit of a plasma surface (see Figure 1.3). If q is rational, the helical pitch is such that a field line on that surface will form a closed loop after completing m toroidal transits and n poloidal transits, $q = m/n$. Surfaces with rational values of q will be subject to resonant instabilities[13] with the same toroidal and poloidal wavenumbers m and n. Kink modes have long toroidal wavelength, frequently $n = 1$ or perhaps $n = 2$. The growth rate of the external kink is largest when a surfaces with rational q lies just beyond the plasma edge[18]. The name 'safety factor' is due to the fact that low rational q is associated with greater susceptibility to disruptive kink instabilities.

If the major radius R_0 of the plasma is significantly larger than the minor radius a, we can approximate the plasma as cylindrical and the toroidal field as roughly constant over the plasma cross section, and q at the plasma edge can be approximated as q_*:

$$q_* = \frac{2\pi a B_t}{2\pi R_0 B_p(a)} \tag{1.13}$$

or

$$q_* = \frac{2\pi a^2 B_t}{R_0 \mu_0 I} \tag{1.14}$$

If the plasma is not circular in cross section, the distance required to traverse a full poloidal circuit becomes larger. If the plasma is elliptical, we define an elongation κ such that the the relation between the vertical semi-axis, b, and the horizontal semi-axis, a, is:

$$b = \kappa a \tag{1.15}$$

κ can vary from 0 to ∞, with $\kappa = 1$ defining a circular cross section. For cross sections that are not highly ellipsoidal, we can approximate the poloidal circumference $C_p = 2\pi a\sqrt{(1+\kappa^2)/2}$ to arrive at a definition of the safety factor for an elliptical plasma[24]:

$$q_* = \frac{2\pi a B_t \sqrt{(1+\kappa^2)/2}}{2\pi R_0 B_p(a)} \tag{1.16}$$

For a circular cross section plasma, increasing κ while holding all other equilibrium parameters constant, q_* will increase. This allows larger currents to be run through appropriately shaped plasmas while keeping the safety factor above a value that would endanger the stability of the plasma column. At the separatrix of a diverted plasma q_* is formally infinite due to the poloidal field null at the X-point, so q_{95}, the value of q at the the $\Psi = .95$ flux surface is used in its place.

On HBT-EP, a broad current profile created by rapid inductive startup and strong current ramp is the primary driver of the kinks observed[25]. Plasma current, toroidal field strength, major radius, and minor radius are chosen such that $2 \leq q \leq 5$, which permits strong $n = 1$ and $n = 2$ kink instabilities.

1.2.2 Resistive Wall Modes

Given the assumptions of ideal MHD, in which all conductors have zero resistivity, the growth time of an unstable external kink is of the same order as the plasma Alfvén timescale τ_A. On HBT-EP this timescale is is $\tau_A \sim 0.1\mu s$. Below a critical β, the ideal kink can be stabilized by a nearby perfectly conducting wall, and the closer the wall is placed to the plasma, the greater the degree of stabilization provided.

Ideal theory is generally sufficient to predict global stability of plasmas and the structure of unstable eigenmodes[22, 23], but in reality, both the plasma and any nearby conducting structures have finite resistivity. The need to account for the effect of conducting structures with nonzero

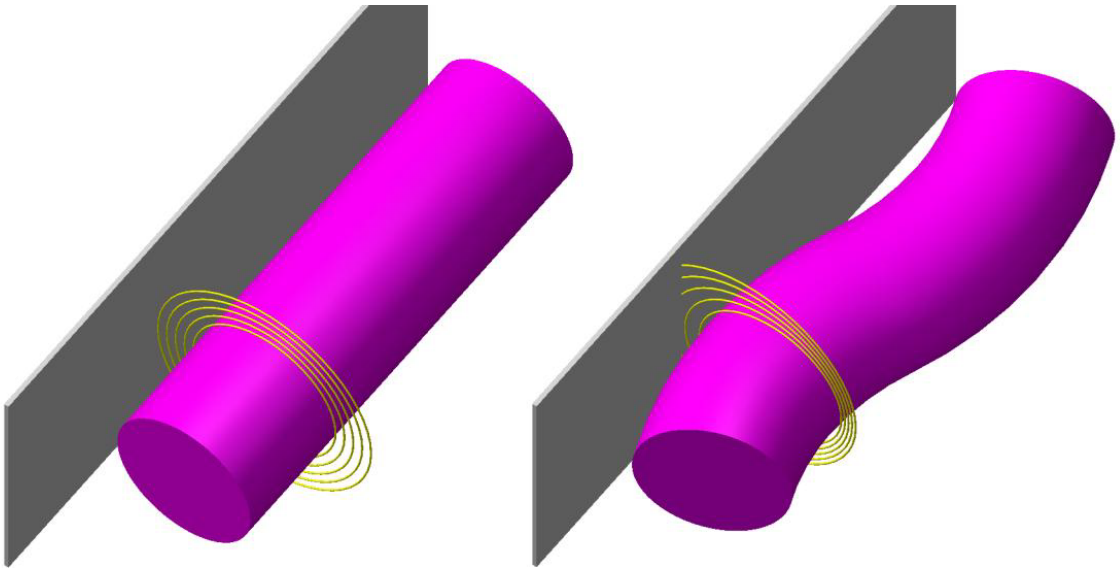

Figure 1.7: The magnetic field lines of a straight cylindrical plasma, and those of a kinked cylindrical plasma, in the presence of a conducting wall. The penetration of the field lines into the conducting wall will be opposed by eddies generated by the changing normal flux, and will be slowed to the timescale of the resistive decay of the eddies. The eddies that oppose the normal field will enhance the strength of the poloidal field as they compress the poloidal flux between the plasma surface and wall.

resistivity on the mode has been recognized as necessary for accurate reproduction or prediction of measurements for some time[26, 27].

The Resistive Wall Mode (RWM)[28] arises from the same physics as the ideal kink but with the plasma in the presence of a nearby resistive conducting structure, and has been observed on HBT-EP and elsewhere[29, 30]. As the mode grows, the perturbation of the flux surfaces will be slowed by eddy currents in the conductors opposing the changing flux through their surface, as shown schematically in Figure 1.7. The RWM has nearly identical stability boundaries as an ideal kink with no wall stabilization[31], but the growth rate of the RWM is of the order of 1ms, depending on the inductive and resistive timescale τ_w of nearby conductors.

To calculate accurately the susceptibility of diverted plasmas, with their infinite edge q, to destabilization by kink modes with low m and n requires computation of resistive MHD effects[32, 33], including the tearing of magnetic surfaces, near the separatrix. If the mode rotates relative to the the resistive wall[34, 35], the eddies generated will oscillate at the frequency of the mode. At frequencies higher than τ_w^{-1} eddies in the conductor will not decay significantly during a rotational period, and the stability boundaries of the mode will approach that of a plasma stabilized by an

ideal wall.

1.2.3 External Perturbations

In the presence of external fields resonant with MHD eigenmodes the natural mode can be driven or suppressed[30, 36, 37], depending on the relative phasing of the applied fields and mode. With an effective control algorithm these currents can supplement or replace the naturally suppressive eddies[25, 29] in resistive walls, slowing or stopping the growth of the instability. In a diverted configuration, applying resonant perturbations for the purposes of maintaining plasma stability can affect the field geometry and performance of a divertor[38–40], and soft X-ray observations of the plasma response near the X-point indicate short wavelength kink-like response just inside the separatrix[41]. For this research, these fields are applied in such a way as to excite the modes[42–44], and the response of the mode to perturbation is measured.

1.3 Plasma Shaping

The external fields that are imposed on the plasma column in HBT-EP in the absence of shaping create a cross section that is circular. The plasma will grow in minor radius until a is equal to the distance from the magnetic axis to the nearest limiting surface. Plasma that migrates to field lines beyond the flux surface that is in contact with the limiting surface enters an annulus known as the 'scrape-off layer' (SOL), and will impinge in a very short time on a material surface, lose thermal energy, and recombine. Depending on the location of the plasma in the vessel, the point at which plasma recombines will vary, but there will always be a flux surface beyond which the plasma is no longer confined. This surface is known as the last closed flux surface (LCFS).

Beginning in the 1970's[8, 45, 46], external coils were added to tokamaks specifically to modify the plasma cross section, changing the shape of the plasma from circularity. If a coil carries toroidal current in the same direction as the plasma current, a field null (X-point) in space between the plasma and the coil is created. The flux surface that contains this X-point is known as the separatrix. If the separatrix flux surface on the plasma side does not impinge on a material surface, the separatrix defines the LCFS. In this case, the plasma is said to be 'diverted'. Refer to Figure 1.8 for the definitions of the terms separatrix, last closed flux surface, and scrape-off layer as they pertain to limited and diverted plasmas.

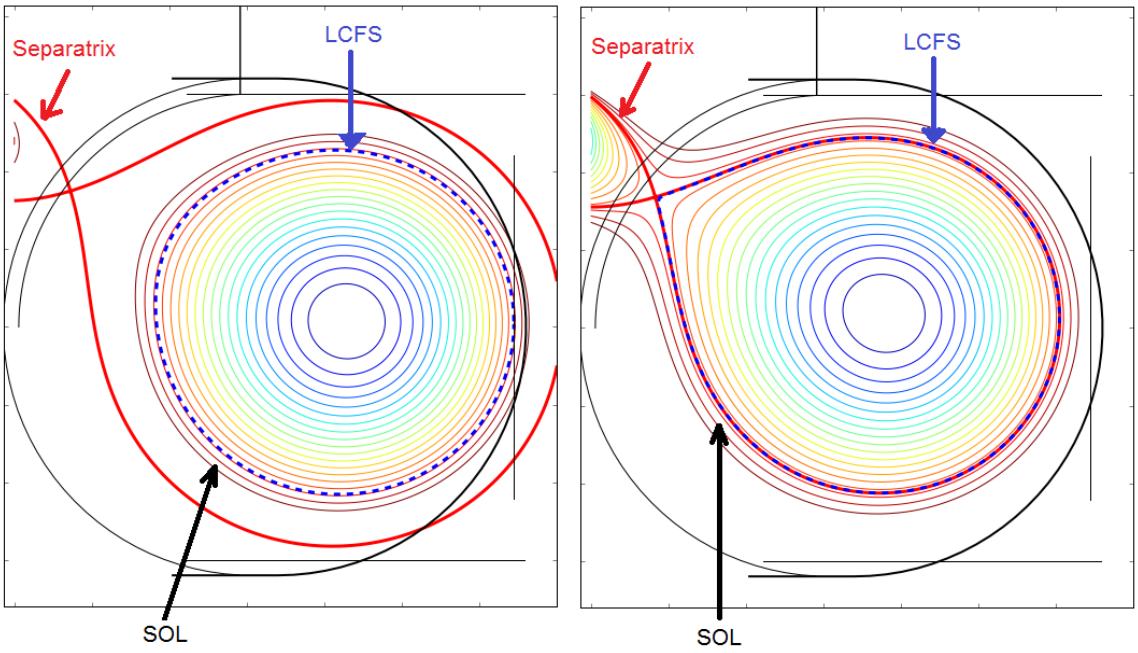

Figure 1.8: Flux surfaces of a shaped, limited plasma and a shaped, diverted plasma. Last Closed Flux Surface (LCFS), Scrape-off Layer (SOL) and Separatrix are indicated.

Flux surfaces in the SOL intersect a material surface, and any plasma located on that flux surface will rapidly collide with and recombine on that surface. In the case of a shaped, limited equilibrium, plasma that migrates into the SOL will impinge on any limiting surface that extends to that particular SOL flux surface. In the case of a diverted equilibrium, SOL plasma will flow towards the X-point, and strike the wall mainly in a poloidally narrow toroidal band, known as the divertor region.

Diverted plasma operation is a feature of all modern advanced tokamak concepts, primarily to control the heat and particle exhaust of a fusion power reactor[9, 10]. Sensitive instruments can be placed away from the divertor region to limit damage from plasma-material interaction, while at the divertor, the recombined gas can be efficiently pumped while the heat flux can be spread as widely and evenly as possible[38] onto a region of the vacuum vessel specifically designed to accept the influx of energy.

In addition to diversion, most advanced tokamaks actively shape the plasma cross section in order to optimize plasma parameters or probe new physics. Experiments have demonstrated effects of different plasma shapes on such parameters as beta[47], edge localized mode control[48, 49], divertor power loading[40, 50] bootstrap current fraction[51], MHD Stability [7, 52], and even bulk

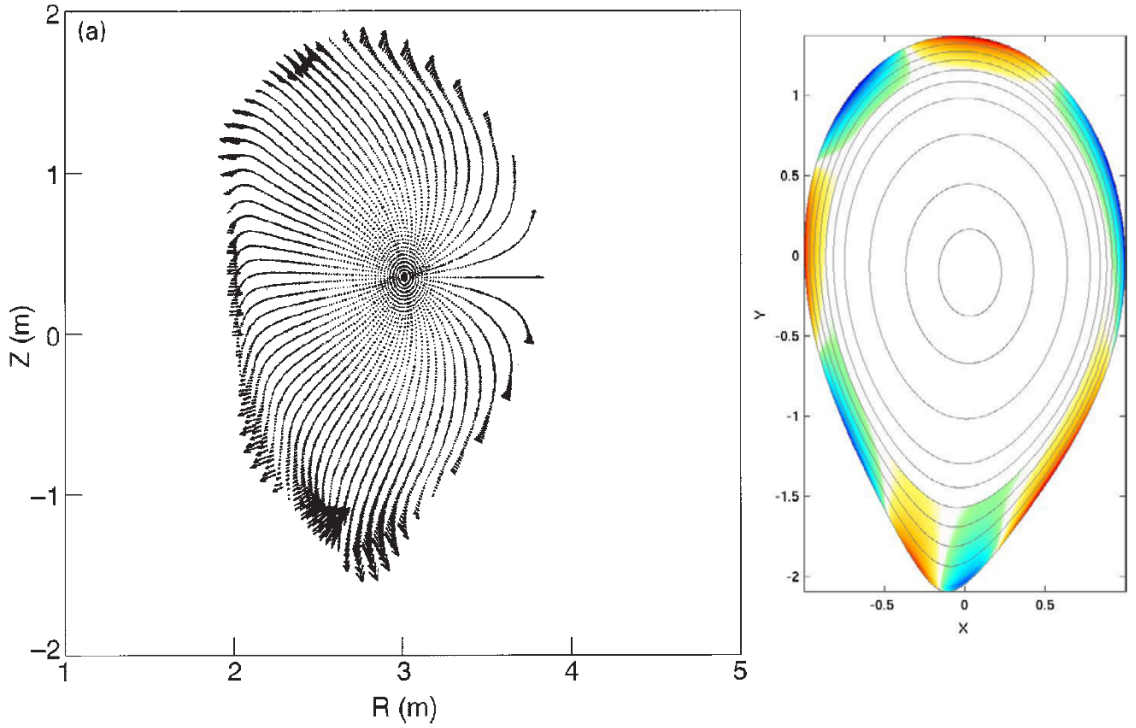

Figure 1.9: Calculated kink mode structure in two diverted JET equilibria. The plot on the left, taken from Reference [54], shows an $m = 5$, $n = 1$ kink mode, while the plot on the right, taken from Reference [33] shows an $m = 4$, $n = 1$ mode. In both cases, the mode amplitude is largest at the edge of the plasma, and near the X-point, the wavelength of the mode is locally shortened. Both calculations are performed over the region $0 \leq \Psi \leq .99$.

plasma rotation [53].

The structure of the external kink is calculated to have short-wavelength features near the X-point, which can have significant amplitude with respect to the mode along rest of the poloidal circumference. Figure 1.9 shows the calculated structure of an external kink in two diverted equilibria in JET. The plot on the left side calculated using ideal MHD, and the equilibrium was examined using soft X-ray diagnostics with line of sight to the X-point[54]. Though the potentially important near-edge region[33] (normalized $\Psi \leq .98$) was not observable due to a minimum energy cutoff in the SXR diagnostic, the phase of the measurements agreed well with the calculations. The plot on the left is the result of resistive MHD calculations of a similar equilibrium.

1.4 The High Beta Tokamak - Extended Pulse

The High Beta Tokamak-Extended Pulse (HBT-EP) is a tokamak experiment used to observe and control marginally stable and unstable MHD kink and resistive wall modes[55]. It is a high aspect-ratio, ohmically heated tokamak that usually generates a limited plasma with a circular cross section. It has a moveable modular wall for passive MHD stabilization, actively driven saddle coils to allow excitation and suppression of MHD eigenmodes, and a high-resolution set of magnetic diagnostics for observing the structure and evolution of external kink instabilities and their response to magnetic perturbations. During 2009-2010[56], all these systems were upgraded. In 2013, ferromagnetic tiles were added[57] as plasma-facing components on the passive shells.

The published research that has been performed since this upgrade includes:

- Magnetic sensors were calibrated in-situ using currents driven in well-positioned conductors in the vacuum vessel[58].
- The structure of the external kinks have been characterized using magnetic[59–61] diagnostics, and the response of external kinks to static RMPs has been observed using magnetic[43, 59–61] as well as optical[62] diagnostics and characterized.
- Studies of active mode stabilization using a low-latency[63], parameterized, adaptable feedback control system[36, 37] have demonstrated suppression of external kink modes.
- The effects of ferritic material on plasma disruptivity, plasma response to resonant magnetic perturbations, the growth rate of MHD instabilities, and the effectiveness of mode suppression have been studied[64].

Previously, HBT-EP experiments did not include control of the geometry of the plasma cross section. This thesis describes the creation of diverted plasma equilibria and the investigation of kink instabilities in diverted plasmas. This research answers the following four questions:

1. Can the HBT-EP cross section be shaped to allow the study of external kink modes and their control in stable diverted equilibria?
2. What are the effects of plasma cross sectional shape on the structure of external kink modes?
3. What are the effects of plasma geometry and mode-coupled eddy currents on the magnetic

measurements of the structure of the external kink, and can these effects be quantified to permit comparison between measurement and theory on shaped and unshaped plasmas?

4. When external magnetic perturbations are applied, is the response of a diverted equilibrium different from that of a circular equilibrium?

All four of these questions have been successfully answered. In particular:

1. Shaped plasma equilibria are numerically determined to be fully diverted and stable for many growth times of the no-wall positional instability, allowing study of shaped plasmas in HBT-EP.

2. Naturally occurring external kink modes are measured in diverted plasmas and compared to those in circular cross section plasmas. Their structure is found to be similar to circular plasmas when q_95 of the shaped plasmas is close to q_* of the circular plasmas, but with a short-wavelength feature near the X-point that is not observed in circular plasmas. These modes are observed to rapidly grow before the plasma disrupts, and maintain large amplitudes throughout the disruption. Shaped plasmas are found to have shorter lifetimes, more rapid loss of magnetic and thermal energy during disruptions, and qualitatively different MHD behavior during disruption.

3. The ideal MHD stability code DCON[22, 23], used in combination with the finite-element electromagnetic code VALEN[27], accurately predicts the measured structure of the modes in both circular and diverted equilibria.

4. Circular and shaped equilibria are actively perturbed with external magnetic perturbations and the static response in both geometries is seen to have the structure of the naturally occurring, rotating kink mode. Shaped equilibria are observed to have a similar response level to perturbations, as measured at the sensors as circular plasmas with similar plasma current and major radius.

1.5 Organization of Thesis

In Chapter 2 the extended systems of HBT-EP with the exception of the shaping coil are described, along with the diagnostics necessary for this research. Chapter 3 describes the new shaping coil, including design constraints, the power supplies, and the qualification of the coil performance and

impact on other systems. Chapter 4 presents the equilibrium of a shaped plasma, including the axisymmetric stability of the shaped plasma column, simulations of the shape of the LCFS, and experimental verification of full diversion via magnetic measurements. Chapter 5 explains the analysis performed on signals gathered from HBT-EP's magnetic diagnostics, and the structure of the external kink modes as determined from the measurements. Chapter 6 concerns the suite of software available for reconstruction of plasma equilibria, calculation of resonant modes structure, and eddy currents induced by mode rotation. These computational methods model the effects of eddy currents generated by the fluctuating modes, as well as sensor/plasma coupling on measurements and the results are compared to our results. Chapter 7 discusses the results of perturbing the plasma surface with actively driven saddle coils. Chapter 8 summarizes the conclusions of this thesis and suggests possible future work. Appendix A describes the semi-permanent limiters and coil holders installed on HBT-EP as part of the installation and operation of the coil, as well as circuit diagrams and a partslist for the shaping coil power supply.

Chapter 2

HBT-EP Capabilities

HBT-EP is an ohmic tokamak with a set of equilibrium field coils that drive plasma current and maintain a radial equilibrium position. It is designed to generate a plasma that is circular in cross section, with the last closed flux surface determined by a limiter. Prior to the introduction of shaping on HBT-EP, limiters defined the plasma minor radius and with it, the plasma cross section. Detection of magnetic mode activity and MHD response to feedback is accomplished via a set of 216 in-vessel Mirnov coils. These sensors measure radial and poloidal fields, and are distributed in two poloidal rings and five toroidal rings. Measurements provided by these sensors are the basis for all MHD mode analysis in this thesis. MHD kink modes can be stabilized by inserting or retracting one or more of 20 modular, conformal shell segments. On each shell segment are mounted two sets of three poloidally offset saddle coils. Any subset of up to 40 of the 120 total saddle coils can be energized to create resonant magnetic perturbations with rich spatial and temporal structure. A Langmuir probe is used to diagnose the location of the edge of plasma equilibria.

This chapter presents an introduction to the basic operating parameters of HBT-EP as it existed at the outset of this research, describes the set of plasma diagnostics used to examine plasma equilibria and MHD fluctuations, and discusses the instruments available to passively and actively stabilize or perturb the equilibria.

2.1 Magnet Systems

The plasma is confined and positioned in tokamaks by magnetic fields. These externally applied magnetic fields are generated by current carrying coils external to the chamber in which the plasma is created, that persist for much longer than the timescales of eddies generated in the chamber. In HBT-EP, plasma current is driven and the plasma is heated by an applied toroidal loop voltage generated by a solenoid that links its changing flux with the plasma. The flux surfaces of a limited plasma in equilibrium with the vertical field tend to be circular, but can be shaped by the addition of further coils. These coils are visible and annotated in Figure 2.1, the individual coils are discussed in brief below, and plots of the currents in a representative shot are displayed in Figure 2.2.

2.1.1 Toroidal Field (TF)

The toroidal field is generated by 20 coils, regularly spaced about the torus. These coils enclose the vacuum vessel, and define the toroidal geometry of the system. The field on the nominal plasma axis, at a major radius of 92cm, is 0.33T and is essentially unchanging on the timescale of the plasma lifetime. Due to the geometry of the currents that create the field, the magnitude of the field in the vacuum vessel is inversely proportional to radius from the machine axis. The radially outboard half of the chamber is therefore referred to as the 'low field side', with the inboard half referred to as the 'high field side'.

2.1.2 Ohmic Heating (OH)

A solenoid passes through the center of the torus, and is connected to a three-stage capacitive power supply. This acts as the primary of a transformer to which the plasma column is the secondary. A sharp rise in coil current drives an avalanche breakdown of gasses in the plasma chamber[65], and a sustained ramping of the coil current causes a steady increase in the plasma current after breakdown. The poloidal field due to the ohmic heating coils has a null along the midplane at 89cm. During breakdown, the plasma current forms along this closed loop of purely toroidal field. As the plasma current grows, the sum of the poloidal field and the toroidal field forms closed helical magnetic flux surfaces. These nested flux surfaces define a tokamak's magnetic geometry. As the discharge progresses, the current resistively diffuses towards the core region of the plasma, peaking the current distribution. By driving a ramping current throughout the discharge, current in the edge

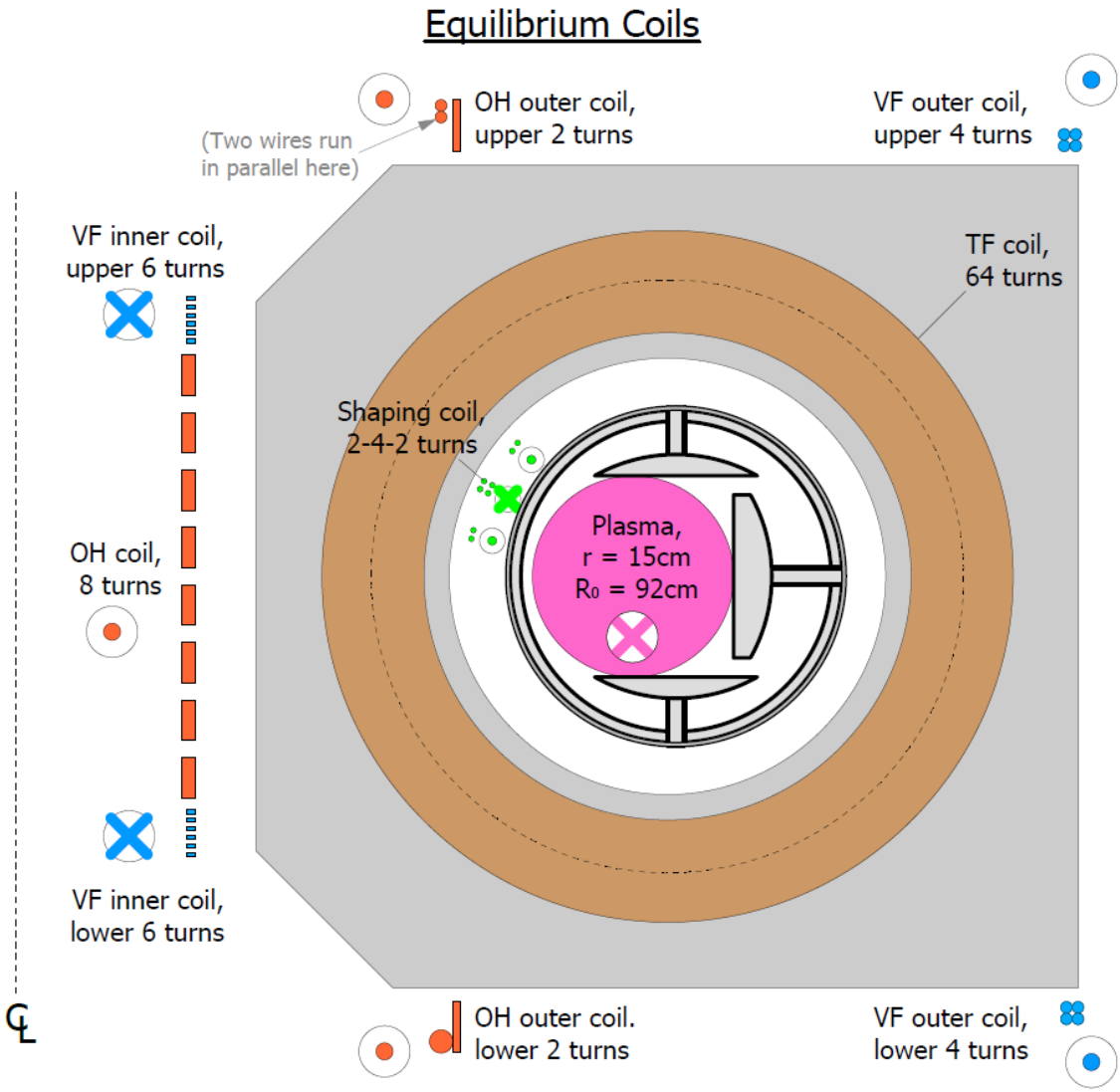

Figure 2.1: A cross section of the HBT-EP Tokamak, with all field generating coils annotated. Toroidal field direction is opposite to the plasma current direction, which is the pink 'x' in the plot. The top, bottom and outboard limiters are present at two toroidal locations, while the inboard limiting surface is provided by the flanges which mate the sections of the vacuum vessel to one another. These flanges extend into the chamber in 20 locations.

region remains sufficiently large to destabilize external kink modes[29].

2.1.3 Vertical Field (VF)

The plasma's tendency to expand in major radius is counteracted by a vertical magnetic field that applies and inward force on the toroidal current. The plasma column is centered at a location

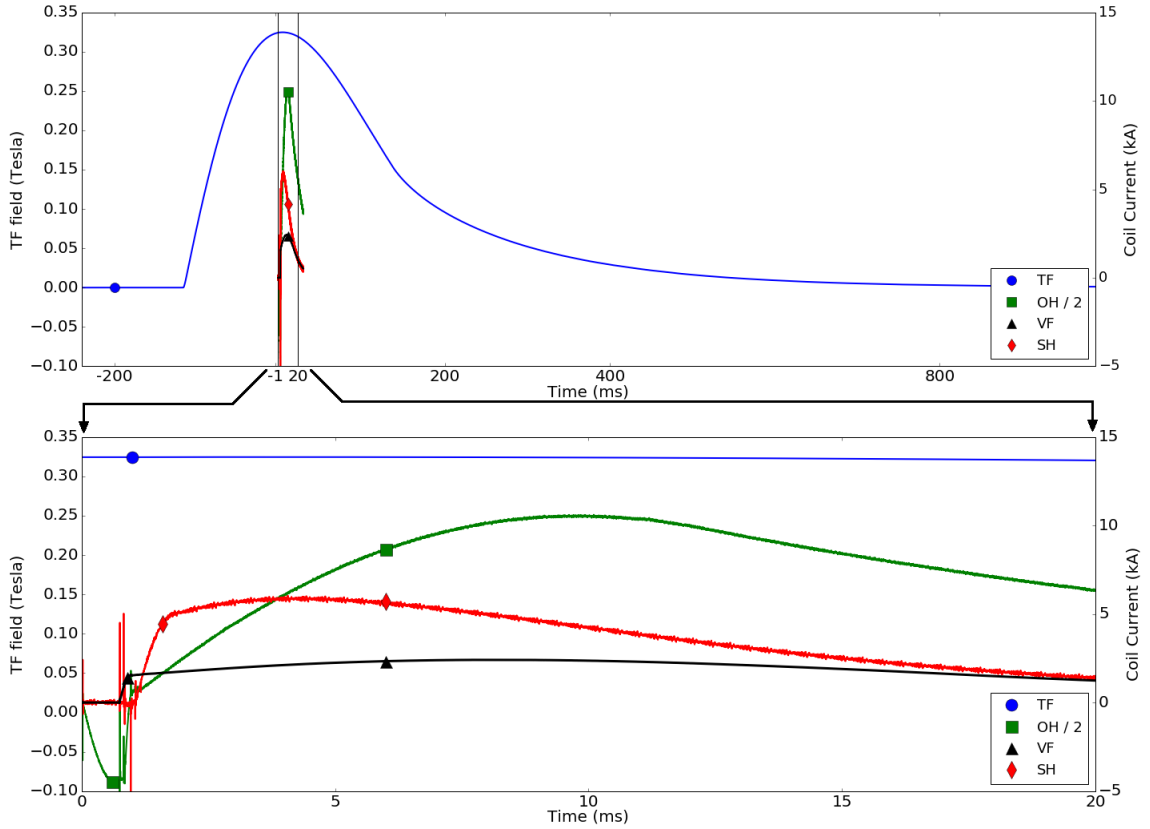

Figure 2.2: Time traces of coil currents and coil fields during a representative non-plasma discharge at the beginning of a run day. On HBT-EP, the currents of the ohmic heating, vertical field, and shaping coil are measured, while the field of the toroidal field coil is measured. Two timescales are shown, accentuating the constancy of the toroidal field during the plasma lifetime. Plasma lifetime is typically from 1ms to no later than 10ms, with shaped plasmas disrupting generally before 5ms. Ohmic Heating current is scaled down by 50% for readability.

where the inward force of the vertical field balances with the outward plasma thermal and magnetic pressure forces. If the vertical field is appropriately curved, as in Figure 1.4, then the off-axis radial component provides a vertically restoring force in the event of a vertical displacement of the plasma column. These considerations are discussed at greater length in Chapter 4.2

2.1.4 Shaping Coil (SH)

The shaping coil is discussed in more detail in the following chapter, but the basic principle of operation is that a strong current is driven in the same (co-I_p) direction as the plasma current, with the poloidal fields of the two currents in opposition in the region between the currents. At some location, the poloidal fields of the two currents exactly cancel. If this poloidal field null "X-point"

is located on a flux surface that intersects with no material surfaces, the plasma edge becomes decoupled from material surfaces. This condition is referred to as "diverted operation".

2.2 Limiters

The plasma edge is fixed by one of four limiters, located above and below the plasma and towards the outboard and inboard regions of the chamber. The 11mm thick, stainless steel flange of each chamber section serves as the inboard limiter and extends 2.5cm from the chamber wall. There are two sets of three blade limiters, located 144° toroidally from each other in the chamber. These can be seen in Figure 2.3. The blade limiters are 9.5mm thick plates of stainless steel. The blade limiters can be inserted or retracted without breaking the vacuum, though their position was not varied for this research.

The limiting surfaces in HBT-EP and the shape assumed by a circular cross section plasma at different major radii can be seen in Figure 2.3. The inboard and outboard limiters are separated by 31.7 cm, and the top and bottom limiters are separated by 30cm. The maximum minor radius is thus 15cm and all sensitive components are positioned in the chamber such that they are further than 15cm from the center of any full-size circular plasma that could be generated.

When the plasma major radius is located between 90.3 and 92 cm from machine center, it is limited by either the top or bottom limiter and can thus change its major radius without a change in minor radius. Outside this region, the minor radius of the plasma varies with major radius, and is equal to the distance from the major radius of the plasma to the nearest limiter.

2.3 Measurement of Equilibrium Parameters

In this section, the diagnostics used to measure the equilibrium parameters of major radius, R_0, and plasma current, I_p, as well as their theory of operation are outlined. Both quantities are measured by Rogowski coils with task-specific windings. Fields from currents not linked by the Rogowskis will be excluded unless they possess sharp spatial gradients on the scale of the coil winding[66]. The shaping coil, due to its close-set contra-directed current bundles, has such a field. The shaping coil field influence on these diagnostics is quantified and eliminated in post-processing where necessary.

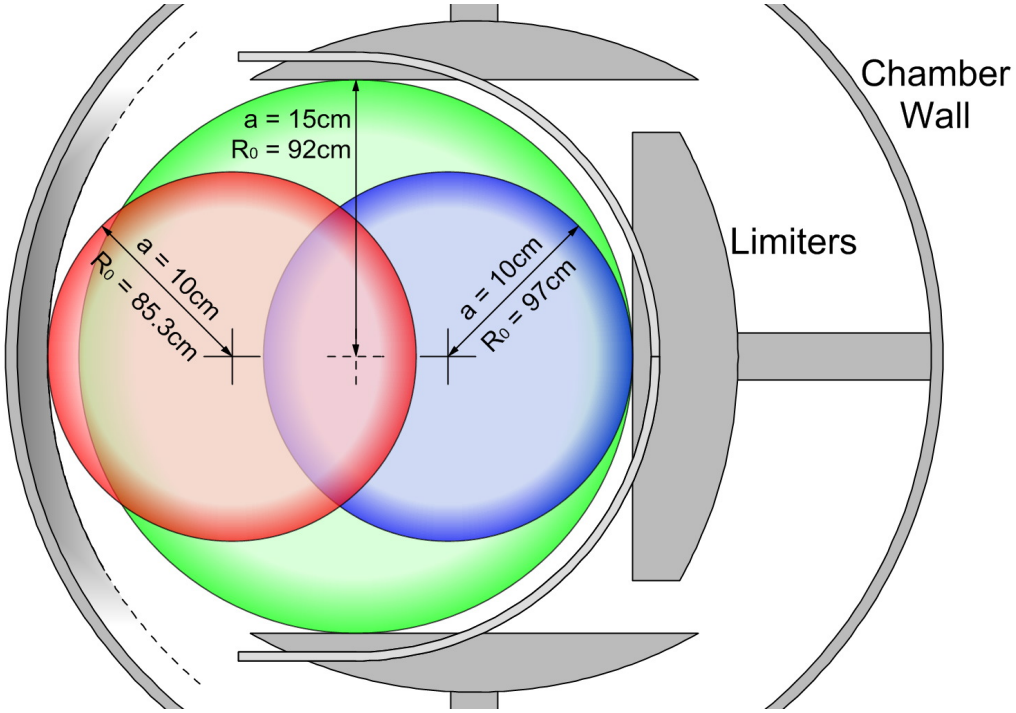

Figure 2.3: Poloidal cross section of plasma in chamber and limiting surfaces. As plasma moves inboard or outboard, minor radius is constrained to the distance between the major radius and the nearest limiting surface.

2.3.1 Plasma Current

The plasma current is measured by a Rogowski coil that poloidally links the plasma column, and is wrapped around the insulating break between vacuum vessel segments at 198° of toroidal angle. The coil has uniform windings, and the exclusion of the shaping field is observed to be satisfactory; a spurious signal equivalent to $\leq$ 100A is observed during a high-current ($\sim$ 6kA) discharge of the shaping coil. As HBT-EP plasma currents are generally 10-15kA, this represents $\leq 1\%$ error on the measurement.

2.3.2 Major Radius

The radial location of the plasma is determined using a Rogowski coil with a winding density that varies as the cosine of poloidal angle. The basic formula[66] for measured signal from a cosine Rogowski coil, including pickup from external coils, is

$$V_{resp} = \frac{d}{dt}(A(R_0 - R_{ref})I_p) + \Sigma_i f(I_i) \tag{2.1}$$

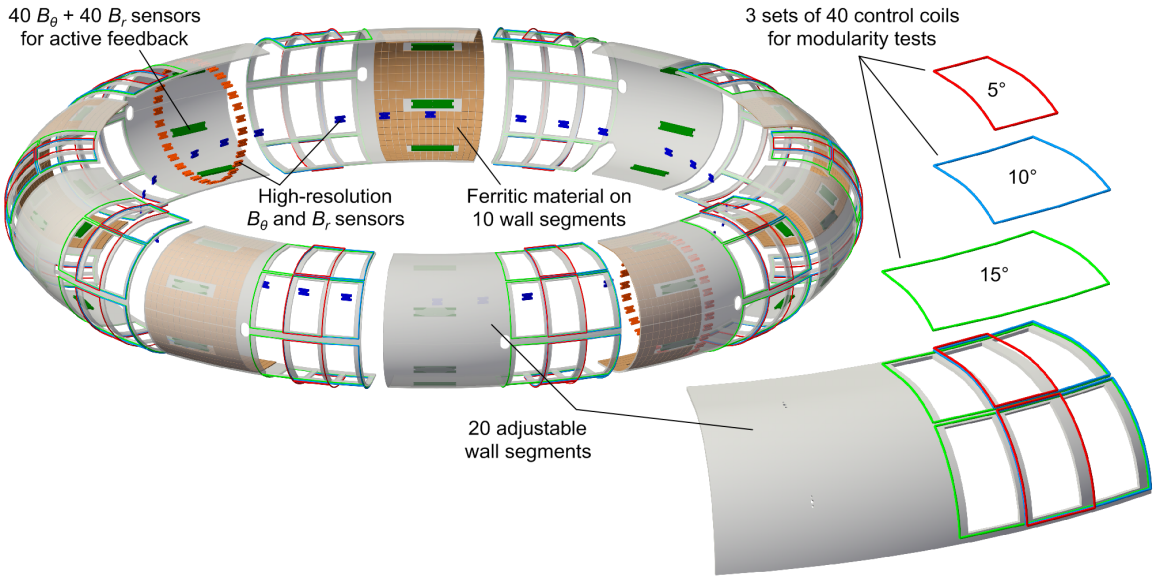

Figure 2.4: Schematic of HBT-EP's full complement of magnetic diagnostics and feedback equipment. Poloidal arrays are in red, toroidal array is in blue, and feedback arrays are in green. The 15° wall-mounted coils are used exclusively to perturb the plasma equilibria in this thesis.

with A a constant multiplier, R_0 the major radius, R_{ref} a reference location, I_p the plasma current, and $f(I_i)$ is the pickup due to the mutual inductance of the Rogowski to the i^{th} external current. Strongly coupled currents include the vertical field, ohmic heating, and and shaping coil currents, as well as eddies driven in the vacuum vessel. Due to the non-uniform winding density and the low nominal signal, this coil is more strongly coupled to external currents than the plasma current Rogowski. During calibration of the coil[42, 58], A and the pickup functions $f(I_i)$ for the vertical field and ohmic heating coils were empirically determined. The determination of the pickup function for the shaping coil is described in more detail in Chapter 3.

2.4 Mode Detection

HBT-EP is instrumented with three sets of Mirnov coils, which measure $\dot{B}$ oscillations in both the poloidal and radial magnetic fields. There are five toroidal rings of sensors at different poloidal locations, and two poloidal rings, spaced toroidally 180° from each other. After passive integration, signals are digitized at a 2μsec sampling rate. The sensors are in-vessel and mounted close to the plasma edge. They are shielded by 64μm thick shimstock[42] made of stainless steel. The shimstock is spot-welded to the shells, which are themselves electrically connected to the vacuum vessel. These

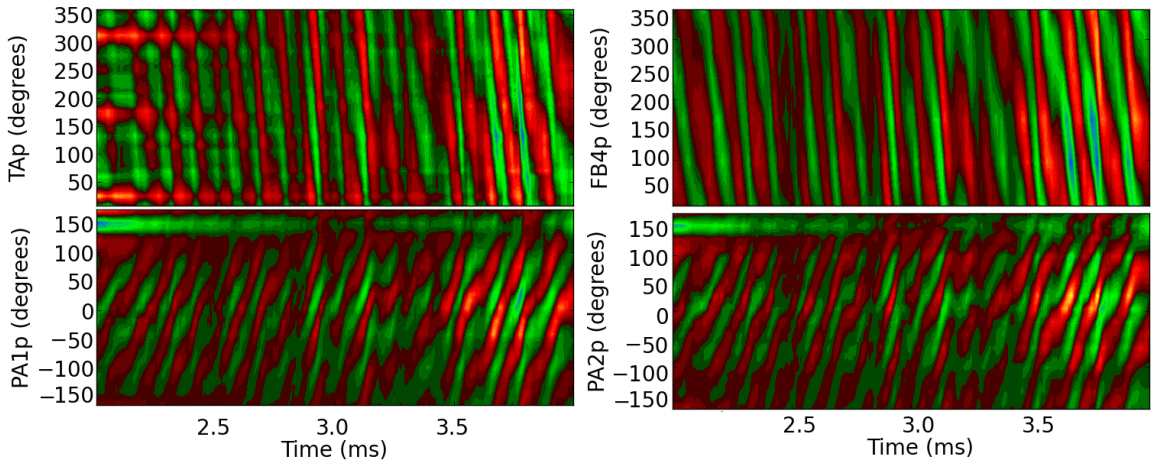

Figure 2.5: B_p fluctuations in shaped shot 90837. The toroidal array (TAp) and feedback array (FB4p) line the inboard and outboard edge of the chamber toroidally. Poloidal arrays 1 and 2 (PA1p, PA2p), line the poloidal cross section of the chamber. Fluctuation frequency and helicity can be determined from this data. X-point is located at 150°.

shields absorb and dissipate the heat flux of any plasma that migrates to a field line intersecting the sensors. The thinness and resistivity of the shimstock permit measurement of MHD modes with frequency $\leq$ 150kHz.

Most of the HBT-EP sensors have windings that measure poloidal field. A subset of these sensors measure perturbed radial field as well. In this thesis, only the poloidal field sensor measurements will be reported for mode analysis. The poloidal field sensors are arranged so as to capture the poloidal and toroidal structure of fluctuations on the plasma surface (see Figure 2.5), and are distributed in three arrays around the torus:

- The Poloidal Array (PA)
  - Two rings that poloidally link the plasma, separated toroidally by 180°, 32 sensors each.
  - Outboard sensors are mounted to the conducting shells, which suppress B_r fluctuations and amplify B_p fluctuations.
  - Inboard sensors are mounted to a thin stainless rib, with minimal eddy current influence.
  - 11.8° of poloidal separation.
  - Red rectangles in Figure 2.4.
- The Feedback Array (FB)
  - Four toroidal rings arranged along outboard surface.

  - Toroidal rings are mounted to the shells and located at ±83.4° and ±29.3°.
  - Toroidal ring consists of ten sensors, regularly spaced.
  - Mounted to conducting shells.
  - Green rectangles in Figure 2.4.

- The Toroidal Array (TA)
  - A toroidal ring of 30 sensors, located 3.8cm below the inboard midplane.
  - Mounted to a thin stainless steel rib.
  - Ten groups of three sensors, 36° inter-group separation, 9° intra-group separation.
  - Blue rectangles in Figure 2.4.

2.5 MHD Interaction via Eddy Currents and External Control Coils

Passive stabilization of MHD instabilities is provided by a set of close-fitting, independently positionable conducting shells. Active probing of MHD instabilities is permitted by a set of shell-mounted saddle coils. Open-loop, feed-forward perturbations can be applied to excite the MHD modes.

2.5.1 Passive Stabilization of MHD Perturbations

HBT-EP is instrumented with twenty 4.75mm thick 316 stainless steel shells. Each of HBT-EP's 10 chamber sections has two shells, an upper and lower, that together cover 180° of outboard poloidal angle. Each shell is independently positionable, and can be positioned 1-5cm from the plasma edge to vary the degree of passive MHD stabilization provided. The shells are designed to be concentric to the outer edge of a circular plasma centered at 92cm. The shells extend horizontally at their top or bottom extent for another 6.35 cm, providing passive stabilization if the plasma moves inboard, or if the shells are retracted. Pictures of the shells during and after construction are shown in Figure 2.6

The PA and FB sensors are mounted on the inner surface of the shells, and their front faces are 5mm from the circular plasma surface. At the time this research was performed, ferromagnetic tiles, shown in Figure 2.4, were attached to the plasma facing side of every other shell[57]. In order to

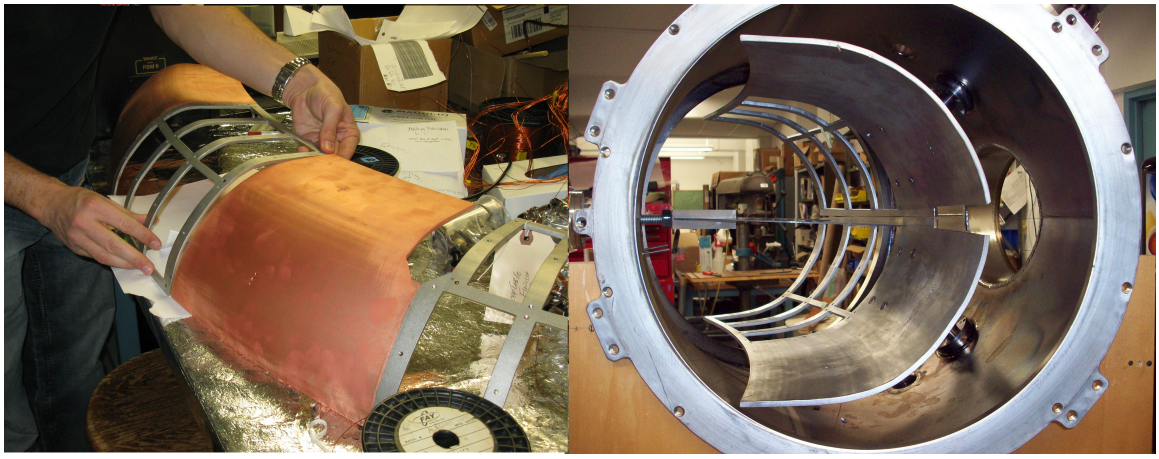

Figure 2.6: Pictures of the shells during construction. On the left, taken before the chrome plating, the copper plating is visible. On the right, two shells mounted in a chamber section for testing before installation. Coils are wound above the cutouts, which allow faster penetration of control fields.

prevent the ferromagnetic material from limiting the plasma, all shells are retracted by 13mm from full insertion[67]. The effect of the ferromagnetic material on the observed and imposed fields, over and above the shell retraction, was not treated in this research.

Viewed from above, the counter clockwise half of each shell is instrumented with control coils, which are described below. The other half of the steel shell is electroplated with 64μm of copper to increase the wall time τ_w, and the copper in turn is coated with a 7.6 μm chrome plating to prevent sputtering. The copper coating thickness was chosen for a wall time of 400μs[42].

2.5.2 Active Control Coils

Each positionable shell is instrumented with two saddle coil sets centered at $\pm 83.4°$ and $\pm 29.3°$, with the sign depending on whether the shell is above or below the machine midplane. The coilsets are arrayed in the same manner as the FB sensors, in ten groups of four, covering about 180° of poloidal angle on the outboard side. Each coil set consists of three coils of equal poloidal extent, and varying toroidal extent, of which only one can be driven at any given time. The coils that make up each triplet have toroidal extents of 5°, 10°, or 15°. Throughout this research, only the 15° coils will be used to energize the plasma, as these provide coverage of nearly 25% of the plasma surface, and have the sharpest mode spectrum with the least sidebands due to the broad coverage of each coil. The location of the coils on the shells and their relative size can be found in Figure 2.4.

Each coil is independently controlled, and can be programmed with an arbitrary current wave-

form, with a maximum amplitude of 40A. For example, the current in the coils, I_i, at toroidal and poloidal angles ϕ_i and θ_i, respectively, create a helical perturbation when the coils are programmed as:

$$I(\phi, \theta, t)_i = A(t)\cos(n\phi_i + m\theta_i + \delta) \tag{2.2}$$

$A(t)$ represents the time varying waveform of the general perturbation and δ represents a phase offset. External kinks with $n \leq 5$, and $|m| \leq 4$ can be strongly interacted with in this manner. Due to our toroidal field direction, plasma current direction, and conventions for measuring poloidal angle, resonant $n = 1$ modes on HBT-EP have negative m-numbers.

The best coupling between coils and plasma is in the case of a circular plasma, centered at 92cm. In this case the shells will be concentric with the plasma column and conformal to the edge, meaning the shell-mounted coils will be conformal as well, and located within 4cm of the plasma surface. The fields applied to the surface of a plasma by an $m = -3$, $n = 1$ coil current perturbation under ideal coupling conditions is modeled in Figure 2.7. In this maximum-coupling condition, 40A of coil current translates to a peak radial field of 60G at the plasma surface. Different plasma locations, LCFS geometries, or coil configurations will all reduce this surface field magnitude, and distort the structure of the applied field. While the general trend of the helicity of the mode is discernible, it is clear that the resonant component of the fields averaged over the entire plasma surface will be much smaller than the peak local perturbation applied.

2.6 Determination of Location of the Plasma Edge

HBT-EP has a 5-tipped radially positionable Mach probe[66, 68], which can give information on the plasma temperature, density and flow in the poloidal and toroidal directions along a flux surface. In this research, only the central probe is utilized, and is used as a floating Langmuir probe. We determine the location of the plasma edge in shaped plasmas by first characterizing the floating voltage of the edge region of circular plasmas. Determination of the probe location relative to the edge region of a circular plasma depends only on probe insertion and plasma major radius, as the plasma cross section is well defined in the absence of shaping. A set of shaped plasmas with different major radii are then created, and when the previously obtained floating voltage is observed, this is

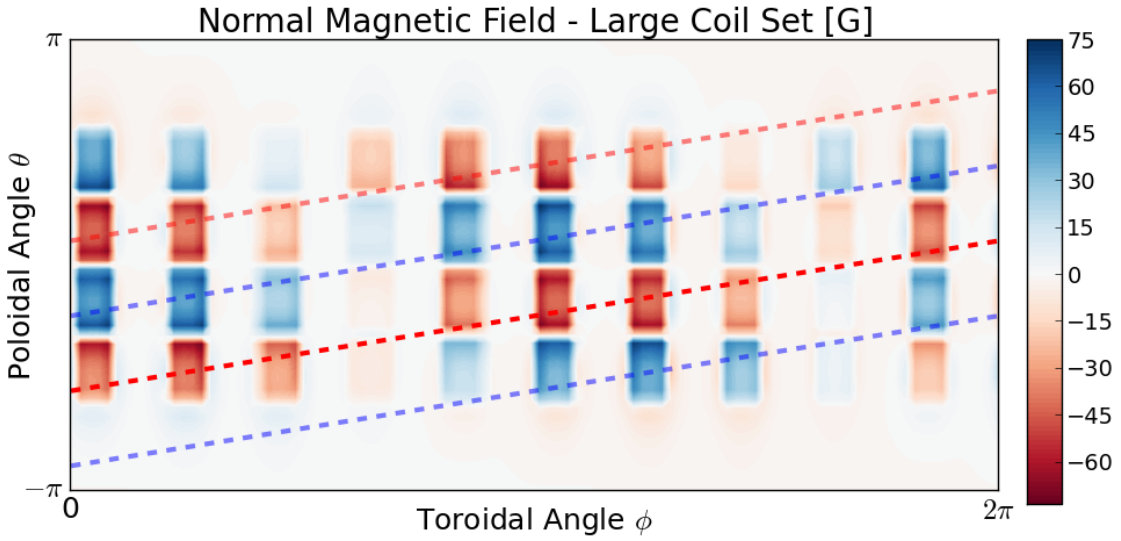

Figure 2.7: Contour plot of the radial field strength due to control coils applying an $m = -3$, $n = 1$ perturbation with the current amplitude of 40A on the surface of a circular toroidal plasma centered at 92cm. Eyeguides show the pitch of an $m = -3$, $n = 1$ field line.

taken as an indication that the probe is in the edge region of the plasma. From this the outboard minor radius of a shaped plasma can be determined, and used as a constraint on equilibrium models of the plasma shape. This is discussed in more detail in Chapter 4.

2.7 Summary

This chapter briefly discussed the systems used to create, control, and measure plasmas in HBT-EP. Additional information appears in References [37, 58–63]

External coils create a toroidal, ohmically driven, circular cross section plasma. The limiters that define the plasma shape and protect sensitive components from the plasma are described. The diagnostics that measure equilibrium parameters of plasma current and major radius, and the assumptions on which their use depends are explained. The sensor set used to observe MHD fluctuations has been described, as well as the methods by which the sensors are shielded from heat flux leaving the plasma edge. The ability of HBT-EP to explore passive stabilization of MHD modes through a variable wall configuration, and to actively probe the MHD spectrum through the use of control coils was discussed. Finally, the floating Langmuir probe used to determine the location of the plasma outboard edge, and the method by which this is achieved, are explained.

Chapter 3

The Shaping Coil

A new poloidal field coil, called the "shaping coil" was installed above the HBT-EP inboard midplane. Powered by a capacitor bank capable of rapid startup and sustained operation at high current, the coil is designed to allow HBT-EP to study diverted plasma equilibria and their associated MHD instabilities. A limiter was machined and installed in order to protect sensors from changes in the deposition of plasma particle and heat flux, which may be enhanced around the X-point. The shaping coil is restrained at several points against the forces imposed on the coil during operation. Between these support locations, the coil is self-supported. The maximum displacement of the coil during a plasma discharge was calculated and is found to be small. The error fields during the steady state period of a coil discharge are studied and found to be largest at locations far from coil holders, and in a manner consistent with displacement calculations.

This chapter describes the assembly of the shaping coil, and the qualification of the coil's performance post-installation. Hardware considerations such as coil connections, the shaping coil power supply, and a new limiter that protects sensors in the divertor region are discussed. We outline the data processing procedures required to accurately calculate the plasma's equilibrium position in the presence of shaping fields. Finally, the methods by which the coil is restrained from moving due to magnetic forces during operation are described, the maximum possible coil displacement is calculated, and the toroidal symmetry of the control coil field is measured.

3.1 Leads And Bundle Connections

The shaping coil is made from a single continuous piece of 14mm diameter, 1/0 welding cable, wrapped eight times toroidally between the inner ring of the toroidal field magnet cases and the vacuum vessel. The coil has zero net current through any poloidal plane, as the eight windings are grouped into a bundle of four, carrying co-I_p current, which is flanked on either side by two bundles of two windings, carrying contra-I_p current. The zero-net current winding reduces the self-inductance of the coil, allowing high coil currents to be driven by low voltages. It also reduces mutual inductances to the VF and OH coils preventing the shaping coil from inducing currents in or having having currents induced by the other poloidal field coils, and reducing coil-to-coil forces. The magnitude of the shaping field will decay rapidly with distance from the coil, so shaping of the plasma cross section will be local, with much of the poloidal circumference remaining circular. Calculated flux surfaces of a diverted HBT-EP plasma is shown in Figure 3.1, with the last closed flux surface and the surface enclosing 95% of the confined plasma poloidal flux, Ψ_{95}, and a circle superimposed for comparison.

The tight spaces involved with the in-situ installation precluded installing the three bundles separately and splicing them in such a way that the chance of arcing could be eliminated. This issue was solved with the choice of flexible cabling which allowed the three cable bundles composing the coil to be wound from a single insulated conductor. Each bundle was connected in series to the next by bending the cable up and over. The leads reach the bundle as a twisted pair, but separate at the coil to join the lower and the top bundle. The lead that joins to the top is tied to the interbundle connections between the bottom and top bundle in order to provide error-field cancellation and reduce any motion induced by magnetic forces. See Figure 3.2 for a schematic of the windings and connection of the leads.

3.2 The Power Supply

The 8-turn coil has a total inductance of 50μH and a resistance of $11\text{m}\Omega$. Large currents ($\leq$ 9kA) can be driven in the coil by a power supply that requires lower voltage than any other HBT-EP coil system. The shaping coil is energized by a pre-programmed two-stage capacitive bank supply. A 7.5mF, 900V bank provides the startup current, with a time to peak current of $800\mu s$. As this bank discharges, a high current diode passively switches a second 'crowbar' bank into the circuit. This

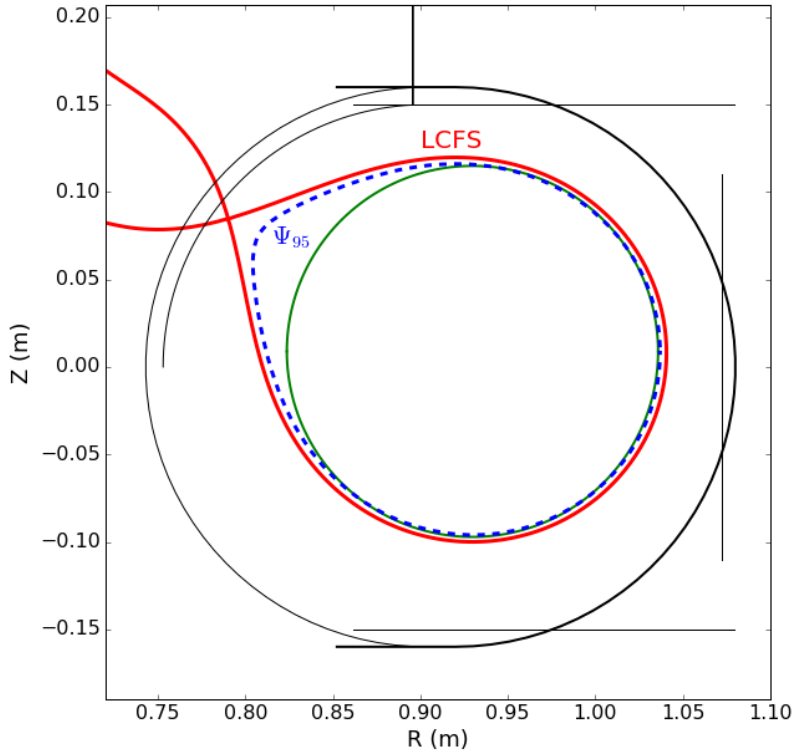

Figure 3.1: Flux surfaces of a diverted HBT-EP plasma, using a filamentary model. Last closed flux surface (red, solid) and the surface enclosing 95% of the plasma poloidal flux (blue, dashed), with a circle of radius equal to the outboard minor radius superimposed (green, solid).

bank has a capacitance of 0.6F, and a maximum voltage of 250V. This much larger bank is capable of sustaining a current of ∼8kA to within 5% for ∼5ms. By selecting different voltages on each bank, a variety of different current profiles can be developed. The 'soft start' of the crowbar bank due to the use of a diode allows for a smooth transition between the two power banks. This smoother switching reduces eddies in the vacuum vessel, and permits the equilibrium field to establish itself near the plasma more rapidly. The shaping coil current trace is compared to the current trace of the actively switched vertical field coil in Figure 3.3. There are a variety of other safety measures used in the bank's construction, descriptions of which, along with full partslist and circuit schematic, can be found in Appendix A.

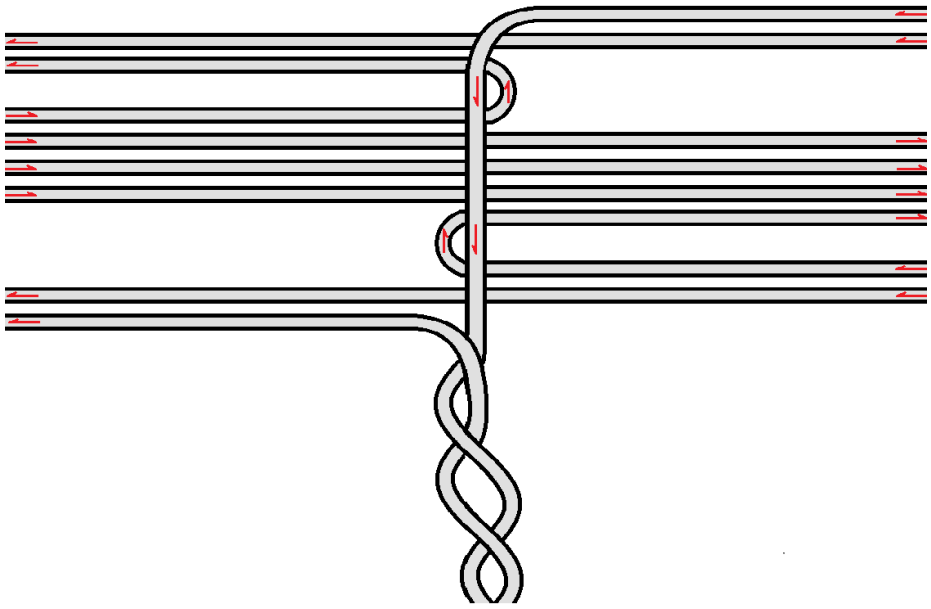

Figure 3.2: Schematic of the current direction, inter-bundle connections and coil leads, looking towards machine center. The toroidal direction is left/right, poloidal is up/down.

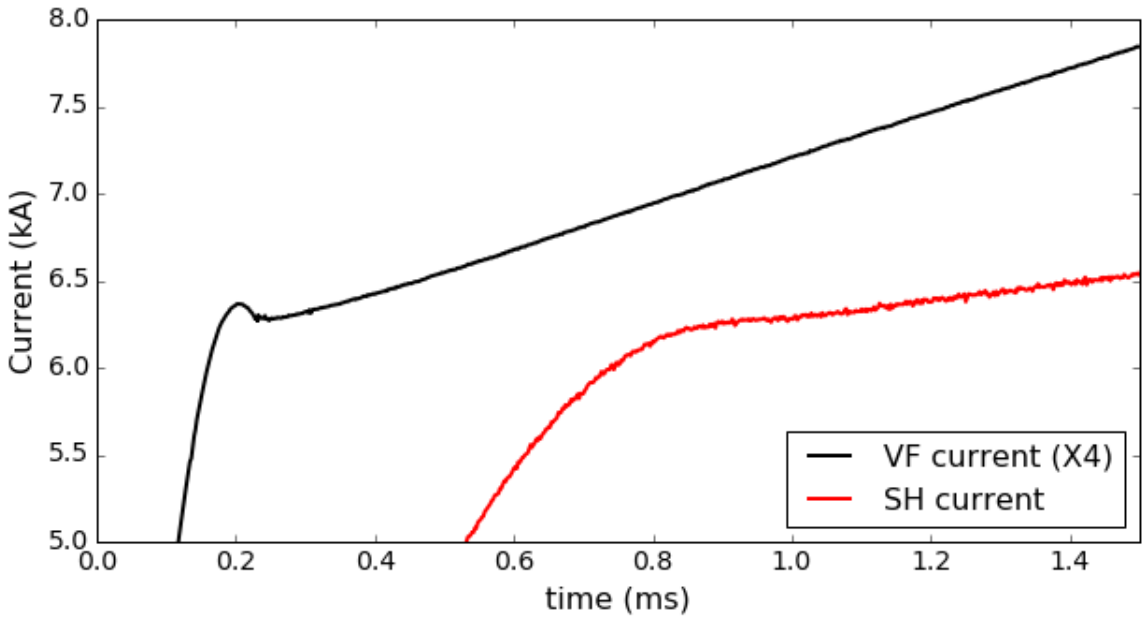

Figure 3.3: Traces of vertical field and shaping field coil currents. Soft-switching via diode prevents switch bounce at the start/crowbar transition, giving a smoother ramp and reducing eddy currents. VF current scaled up by a factor of 4 for easier comparison.

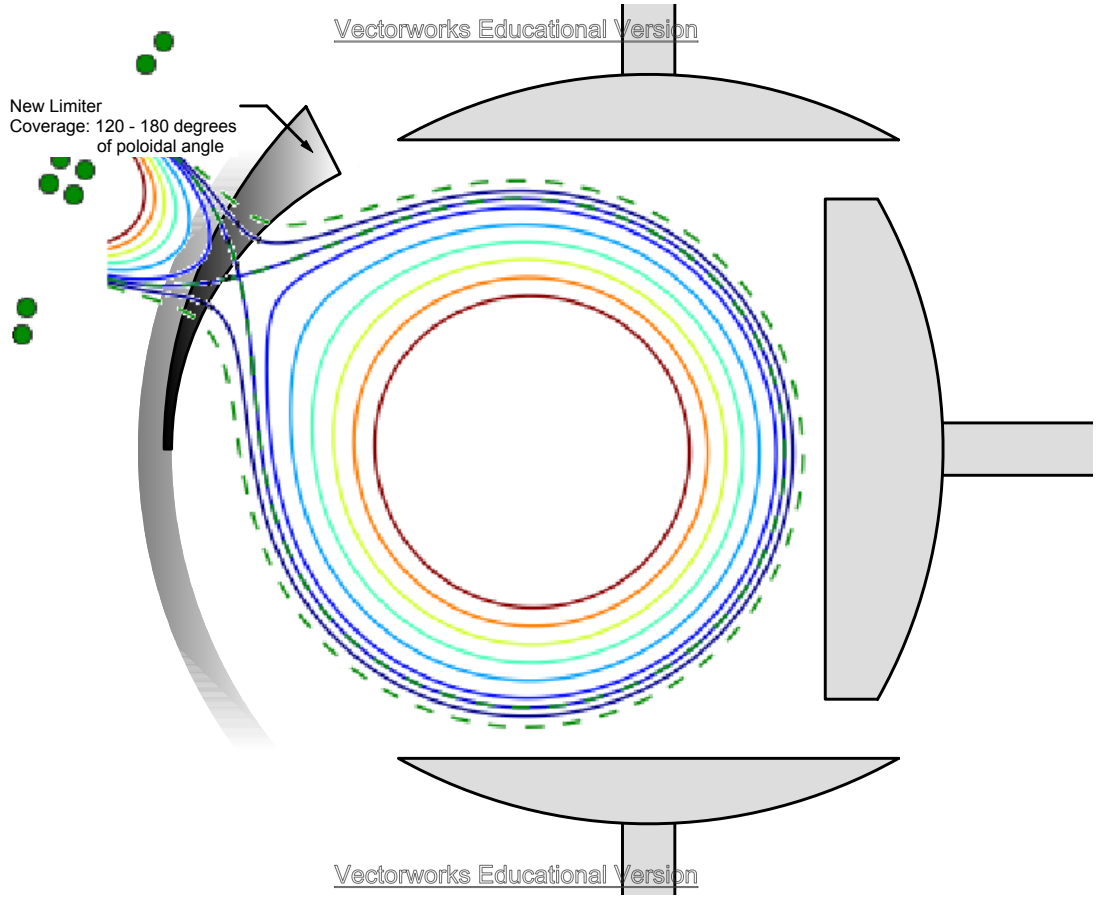

Figure 3.4: Poloidal cross section of shaped plasma in the chamber and limiting surfaces, with new limiter included. The limiter is conformal to the inboard poloidal array sensors above the midplane.

3.3 The New Strike-Point Limiter

The coil is located above the inboard midplane, at $\theta = 150°$. This is the location with highest coupling to the plasma that has a fully unobstructed run and is accessible without dismantling the tokamak. During diverted discharges, the plasma will change the location into which its heat and particle flux is primarily directed, into the area near the X-point.

The poloidal array sensors have protection in the form of 64μm stainless steel shimstock. This thin metallic shield protects against damage to the wires or ablation of the plastic forms by plasma impingement. Under circular operating conditions the plasma flux is low, as the pre-existing limiters maintain a separation between the LCFS of the plasma and sensors of at least 3mm, and absorb most scrape-off layer plasma flux before it can migrate out to the sensors. During diverted operation, sensors that are near the location of the X-point may be damaged as SOL plasma is preferentially

exhausted towards them without protection of a limiter. Additionally, during disruptions, there will be an upward component to the forces on a shaped plasma, causing the plasma energy to be deposited asymmetrically above the midplane. To ensure that this additional heat load does not cause harm to the sensors, a new pair of 6.35mm thick 316 stainless steel limiters was machined and installed. These limiters are attached to threaded rods spot-welded to the flanges of the chamber pieces. These limiters trace an arc concentric with the inboard poloidal array sensors, and extend radially inward 5mm from the inner edge of the sensors. Protection from plasma impingement is provided from $120° \leq \theta \leq 180°$. The location of the limiter relative to the plasma and vacuum vessel is shown in Figure 3.4.

3.4 Elimination of Shaping Coil Pickup For Magnetic Diagnostics

The shaping coil creates local fields with large magnitudes and strong spatial gradients. During the startup phase, the equilibrium field applied by the shaping coil changes on a rapid timescale. Given that the majority of diagnostics measure magnetic fields, or provide measurements based on magnetic fields, the effect on measurement of the shaping coil field must be accounted for and eliminated where necessary.

The Mirnov coils are only affected to the degree that the rapid turn-on of the coil and the associated eddies preclude isolation of magnetic fluctuations from equilibrium signal until the coil reaches steady-state. The plasma current and major radius cosine Rogowski coils' successful use requires elimination of pickup from any coils external to the Rogowski coil's loop, and erroneous calculations of these equilibrium quantities will result unless such pickup is eliminated.

The plasma current Rogowski sees an effect of order 100A at 6kA of shaping current a 1% error when measuring the 10kA diverted equilibria that are analyzed in this research. Pickup on the major radius Rogowski is significant, however, introducing errors in plasma major radius of over 1cm, due to its $cos(\theta)$ winding.

Subtraction of the cosine Rogowski's pickup of the shaping coil field requires a model that includes the shaping coil current as well vacuum vessel eddy currents induced by the coil current. This model was used during the original calibration of HBT-EP's magnetic sensor set, including the cosine Rogowski[43]. The formula for the model is the sum of a linear multiple of the coil current,

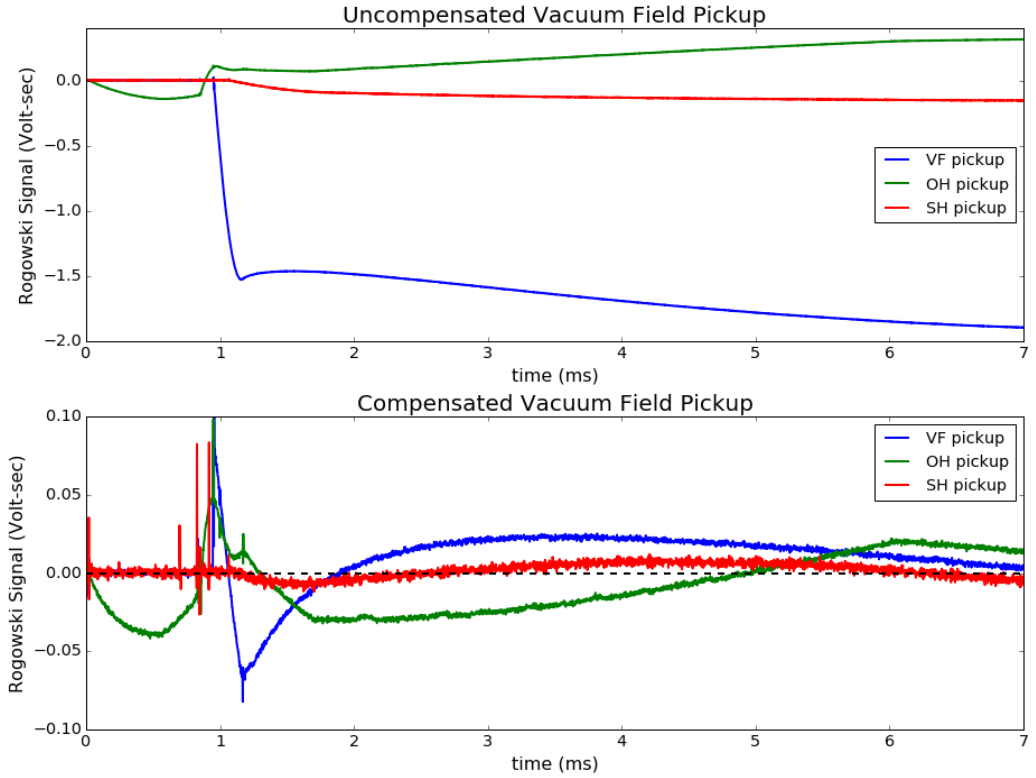

Figure 3.5: Subtraction of the external coil pickup on the major radius Rogowski. Residual error is seen to be much less than any other coil.

and a number of decaying exponentials related to the change of the current in the coil. The form of such an equation is:

$$V(t) = A * I(t) + \sum_i \int_0^t B_i * e^{-(t-\tau)/\alpha_i} * \dot{I}(\tau) d\tau$$

By fitting the parameters A, B_i, and α_i, we arrive at a model of the pickup signal for an arbitrary shaping current. For good removal of pickup, a single exponential term is found to be sufficient.

Figure 3.5 shows the exclusion of the shaping coil pickup with a single pole model, as compared to the simple linear subtraction method used to remove VF and OH coil pickup. The level of residual pickup correlates to a change in calculated major radius of $\leq$ 1mm, biased in the outboard direction. As the residual error of the shaping coil pickup subtraction method is much less than the residual errors from the subtraction of other vacuum field coils' pickup, the major radius of shaped plasmas can be calculated as precisely as that of circular plasmas.

3.5 The Shaping Coil Holders

The shaping coil is supported against gravity and magnetic forces by a set of ten G-10 fiberglass/epoxy composite supports, which are themselves bolted to the TF cases. CAD drawings are available in Appendix A. The bolts are the original structural bolts that clamp the TF cases shut. Nuts located at the point of attachment have been removed, and the bolts now thread into tapped holes in the supports. The previous bolt torque of 40 ft-lbs is applied, with no ill effects on the G-10 holder mounts, providing the same clamping force to prevent any leaks of insulating oil. Due to the closeness of the coil to the chamber, certain locations lacked enough extra space to install a holder. The holders were attached to every other TF case, with a spatial staggering such that they are only on the side of each case that does not face a chamber flange. This is illustrated in Figure 3.6. The coil was then threaded sequentially through each hole in each holder. As such, any modifications or repairs to the coil or any locations on the tokamak obstructed by the coil will require the coil to be either cut or completely unwound. Unwinding represents 2-3 business days of work, as would re-winding, but cutting will make it difficult or impossible to safely reinstall the original cabling given the tight confines of its run and the necessity of good electrical insulation.

The coil holders are further supplemented by a set of ten clamps which link all three winding bundles and hang from the coil itself. These clamps provide no resistance to gravity or net magnetic forces on the coil as a whole, but they ensure correct interbundle separation by opposing the magnetic repulsion between the oppositely-directed currents in each bundle of the coil.

3.6 Coil Motion Due to Magnetic Forces

Between the fixed holders, the flexible shaping coil will move under the influence of external forces, with the constraint that radial expansion is prevented by the strength of the copper conductor. Hanging supports located between the fixed holders constrain the interbundle separation, but still allow the coil as a whole to move relative to the rest of the machine. In order to get an estimate of how the coils move during a shot, the forces on each coil are calculated, and a simple test of the maximum interbundle separation is performed.

The forces on the shaping coil windings are calculated by assuming each current carrying coil on the tokamak is an axisymmetric filament. As all coils carry toroidal currents, the only forces are in the R/Z plane. The toroidal field was not considered in this treatment. The inter-bundle attractive

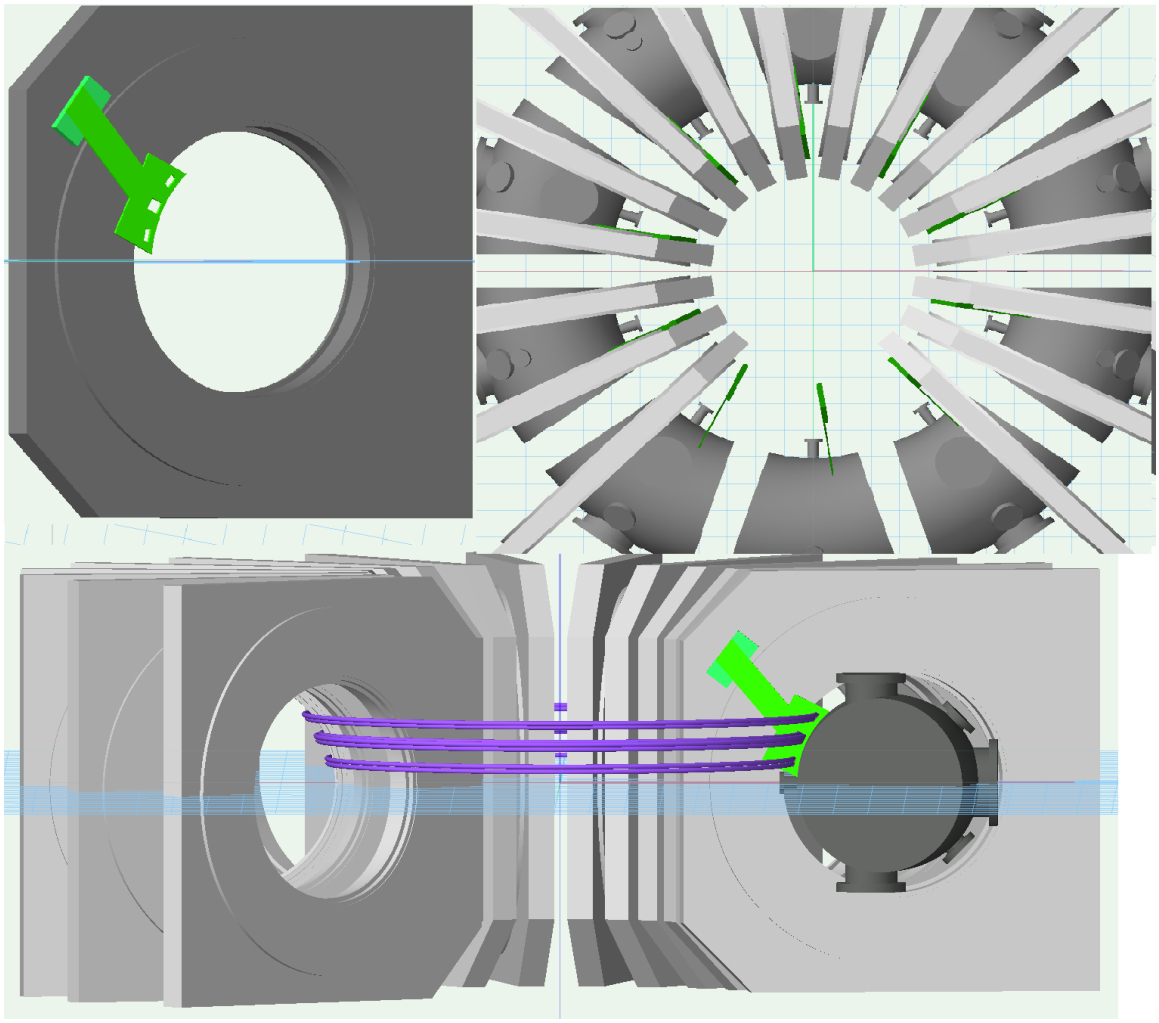

Figure 3.6: Three views of the coil holders in relation to the rest of HBT-EP. Clockwise from top left, a view in the toroidal direction of a single holder attached to a TF case, the view from above showing the staggering of the holders and relation of the holders to chamber segments, and a toroidally directed view of the coil, a holder, several TF cases and a chamber piece to demonstrate the placement of the coil in relation to the superstructure of the tokamak.

forces are so large that each of the three bundles can be modeled as a single body.

The forces on the shaping coil during shot 91486, during the flat-top phase of the discharge when the rate of change of the current is minimized, are modeled in Figures 3.7 and 3.8. The forces on the shaping coil windings due to other poloidal field coils (including the plasma) are plotted separately from the forces due to the shaping coil windings (including each winding's self-induced hoop force). The net force from all sources on a bundle's windings are then plotted as red squares to give a sense of the net motion of each bundle. We see the forces on any given shaping coil conductor are

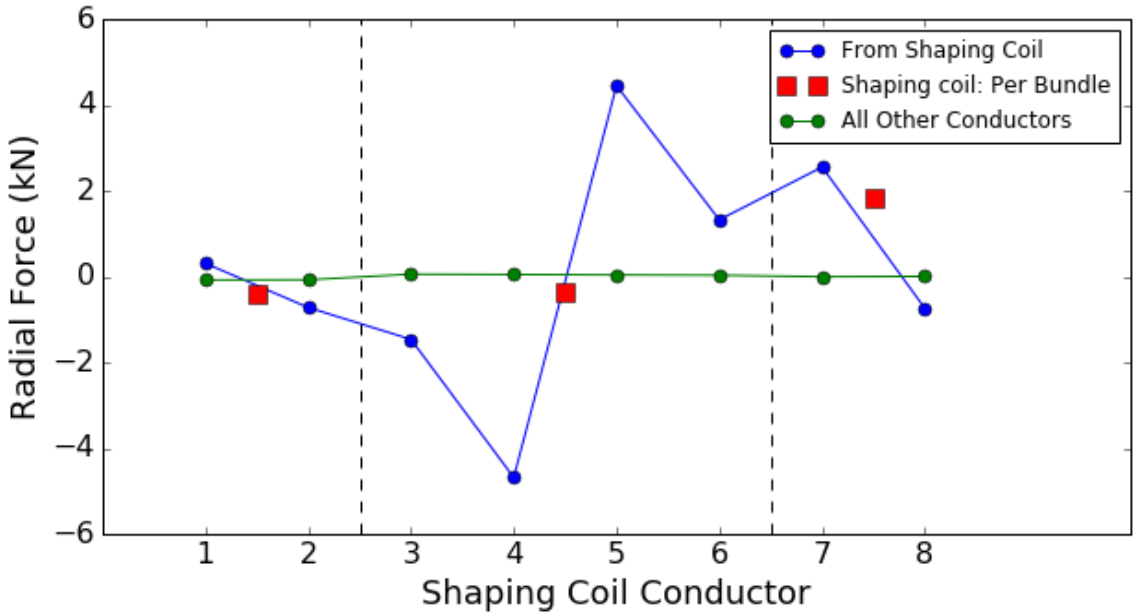

Figure 3.7: Total radial force on each shaping coil conductor due to currents in all conductors, including plasma current and self inductance, for shot 91486 at 3ms. Squares represent the net force on each winding bundle considered as a single object. Dashed lines demarcate separate coil bundles.

dominated by contributions from the other shaping coil bundles, due to the closeness of the bundles to one another and the large currents run through each winding. This means that the dominant motion of the bundles will be to separate from one another, with the flanking bundles moving away from the central bundle.

To understand the motion of the coils during a shot, it is first worth noting that the radial force on the top bundle, windings 7 and 8, is positive, and the resistance of the copper coil to stretching will effectively counteract this force, while the 2.5kN upward force will be unbalanced. The lower bundle, windings 1 and 2, and central bundle, windings 3 through 6, both feel net inward radial forces. The net radial force on the central bundle is comparatively small, as is the net upward vertical force. The net force is 370N 130° off the outboard midplane. The lower bundle feels a primarily downward force, and the radial component is inward, giving a total force of 2.3kN, -100° from the outboard midplane.

The maximum unbalanced force is found to be of order 2.5kN. The cabling itself has a mass per meter of 0.55 kg/m, and so we find both flanking bundles have a vertical acceleration of $\sim$ 1km/s^2, while the central bundle is an order of magnitude less at $\sim$ 100 m/s^2. Assuming a plasma lifetime of 4ms after the imosition of shaping, kinematics equations give a maximum displacement of

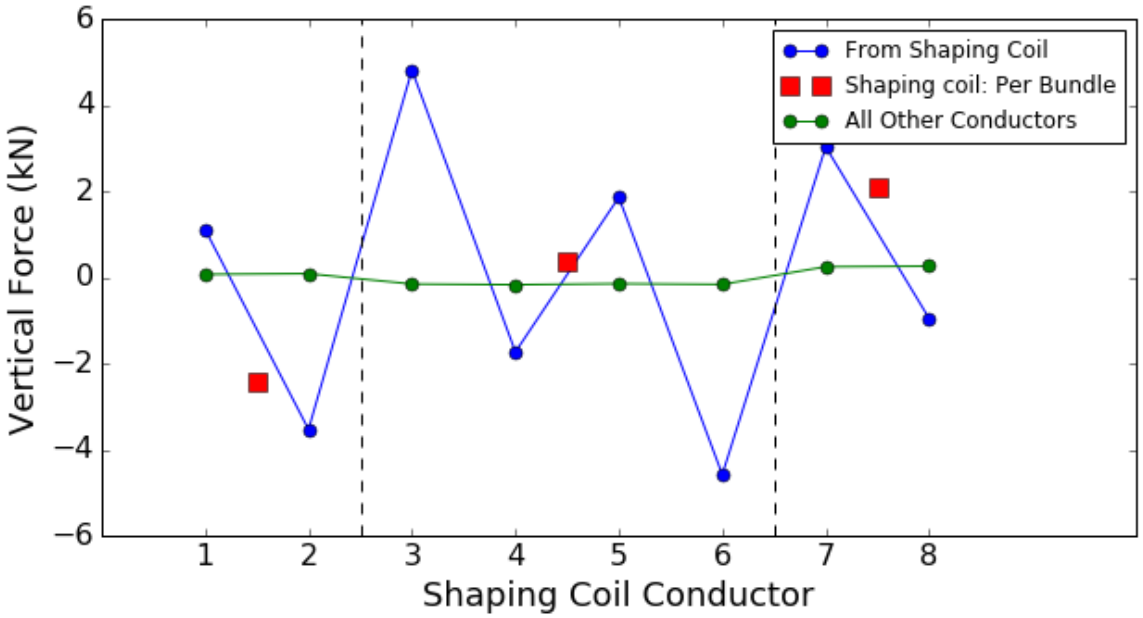

Figure 3.8: Total vertical force on each shaping coil conductor due to currents in all conductors, including plasma current and self inductance, for shot 91486 at 3ms. Squares represent the net force on each winding bundle considered as a single object. Dashed lines demarcate separate coil bundles.

10mm for the flanking bundles, and 1mm for the central bundle, during the plasma's lifetime. This result rests on the following assumptions: the maximum shaping current was immediately delivered with no startup phase, the increased separation under acceleration of the bundles was small, and the positional constraints of the fixed and hanging coil holders were unimportant. These numbers, therefore, represent the worst case displacement.

A second, direct, test involved linking the center bundle and the flanking bundle with precisely known lengths of paper, and observing the length at which the coil begins to rip the paper. The precision in length was achieved by printing mm-scale rulers at scale onto sheets of A-14 paper. These rulers were then cut out, looped around the top and center bundles, and taped closed with clear cellophane tape. The circumference of the loop could then be simply read off the taped loop. This was performed at three toroidal locations, at toroidal angles 0°, 108°, and 288°. With the tape snugly wrapped around the bundles, the total length of tape required was 25cm. It was found that a tape length of 28cm, 26.5cm, and 27.5cm at chamber segments 2, 4, and 7 respectively was required to prevent the tape from being torn by coil jump-out. This corresponds to a maximum displacement of 15mm, 7.5mm, 12.5mm. This test measured only the ultimate limits of the coil motion, reached at a much later time than the termination of a shaped plasma discharge. During a plasma discharge,

the inertia of the coil limits shaping coil displacement to a few mm.

3.7 Field Errors

Installation of the shaping coil required mechanical flexibility to make installation possible, but this flexibility permitted the coil to sag under gravity, and allowed the coil to move under the influence of magnetic forces. This misalignment of the coil leads to non-axisymmetric error fields.

The toroidal array of sensors provides a diagnostic to examine the axisymmetry of the shaping coil. The array covers a full toroidal loop on the inboard side, near the shaping coil. It is well-coupled to the shaping coil, and has the highest toroidal resolution of the three sensor arrays. This allows detailed measurement of the mis-alignment.

To quantify the effects of misalignment or mispositioning of the sensors, the pickup on the vertical field and ohmic heating coils is first measured. The TA sensor array and all external poloidal field coils are nominally coaxial and circular. Comparing the $n \geq 1$ components of the coupling to both of those coils should give an upper bound on misalignment. To avoid considering eddy fields, the sensors are sampled at the point at which the current has reached its flattop value. The shots that will be considered are: 72915 from 9.5ms - 10.5ms for the vertical fields, 72916 from 10ms - 11ms for the ohmic heating fields, 91644 from 4.5ms-5.5ms for the shaping fields.

A filamentary model is used to calculate the expected fields from the coils at the TA sensors. Since the sensors are nominally identical and displaced along the axisymmetric ϕ-direction, the pickup of each sensor should be exactly the same. The expected pickup on the sensors due to each coil is calculated at the specified time, and is subtracted from each sensor's measurement at that time. The results are shown in Figure 3.9, in which the discrepancy between simulation and measurement is low-level and primarily $n = 0$ for the OH and VF coils. For the shaping coil, the error field tends to be strongest between fixed coil holders, to always diverge from the prediction in the same direction, and to have a high-n structure.

The lower bundle of the shaping coil, closest to the TA array, will apply a positive poloidal field to the TA sensors. If it were to move downwards, as calculated, it would increase its coupling to the sensors. Any motion of this sort would be the largest at points on the coil that are furthest from any fixed support. The consistent sign of the error field and the fact that the disagreement is worst between fixed holders, suggests increasing interbundle separation due to jump-out may be the cause

of the discrepancy.

3.8 Summary

The installation of the new shaping coil on HBT-EP is described. The coil is centered 30° above the inboard midplane. The field created by the coil is strong enough to fully divert a 10kA plasma. A limiter has been installed to absorb any additional heat flux and protect sensitive diagnostics near the X-point during diverted operation. Mutual inductances to other coils and diagnostics are low enough to permit drop-in installation of the coil without further modification to the machine. One exception, the major radius cosine Rogowski, has significant coupling to the coil, which was characterized in the same manner as the coupling to the other vacuum field coils[43] and successfully reduced to a level below that of the coupling to other vacuum coils. Installation required a flexible cable for the choice of coil conductor, which allows some motion of the cable under magnetic forces. Worst case deflections of the coil were calculated and measurements of the error fields confirm that the conductor displacement is largest away from fixed coil holders, with the expected sign and magntiude. As will be discussed in later chapters, the field error, which has high toroidal wavenumber n components, is not seen to impact the $n = 0$ axisymmetric positional stability of the plasma equilibrium, nor does it appear to destabilize rotating low-n MHD modes at the plasma surface.

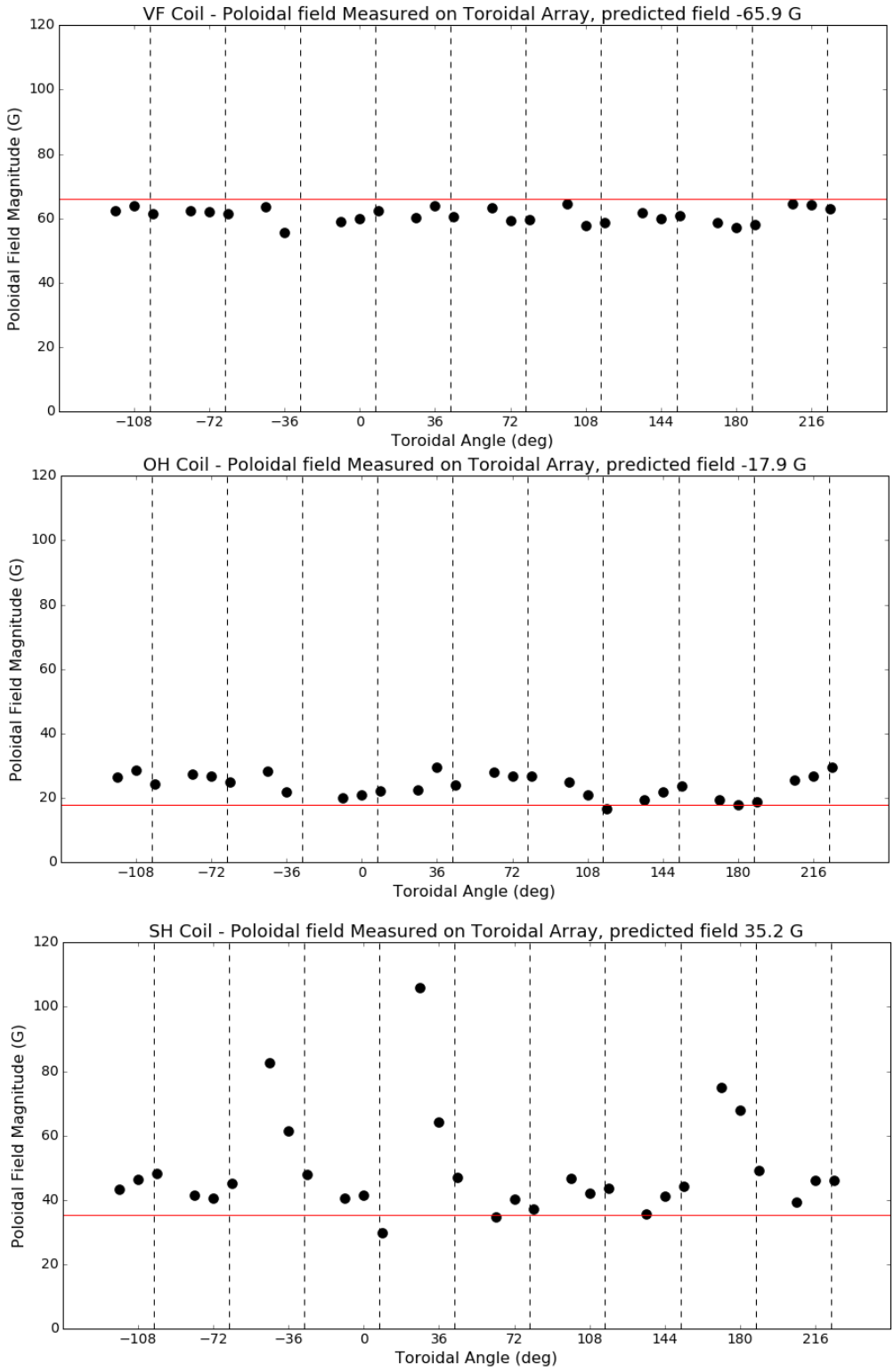

Figure 3.9: Discrepancy between measured and expected poloidal fields from the VF, OH, and SH coils in shots 72915, 72916, 91644 respectively. Worst VF, OH error are 16% and 60%. Worst SH error is 300%. Dashed lines represent the toroidal locations of fixed coil holders.

Chapter 4

Shaped Plasma Equilibria

The first shaped plasma equilibria on HBT-EP are characterized. Equilibrium issues are discussed, including axisymmetric instability, reconstructing the shaped equilibrium, and experimental confirmation of those reconstructions. Energizing the shaping coil affects the decay index of the vertical field during a plasma discharge, and calculations of the stability of a filamentary current on the axis without consideration of stabilizing effects of a nearby conducting wall suggest a horizontal instability. Wall stabilization is calculated to slow the growth of the instability to a timescale that is comparable to or longer than the lifetime of a shaped plasma, and no evidence of a horizontal instability is observed during diverted operation. Equilibrium reconstruction of shaped plasmas is supplemented by determination of the outboard minor radius of the plasma, providing an additional constraint to the reconstruction. The outboard minor radius is determined through the measurement of the floating voltage at varying distances from the magnetic axis of the plasma. Reconstructed equilibria that satisfy the constraint on the plasma edge demonstrate that shaped plasmas are fully diverted when the shaping coil has reached its steady state current, consistent with direct measurement of the equilibrium fields.

This chapter is organized into three sections. First, the positional stability of the equilibrium with and without the stabilizing influence of eddy currents in the nearby conducting wall is calculated. Next, the reconstruction of free-boundary equilibria, including a constraint on the outer minor radius of a shaped plasma is described. Finally, the reconstruction is compared to direct measurements of the poloidal field made by two arrays of sensors that poloidally encircle the plasma.

4.1 Axisymmetric Horizontal and Vertical Stability

The plasma column is subject to major radially expansive forces due to the thermal and magnetic pressures acting on the plasma. This is counteracted by the vertical field, which applies an inward force to the toroidal plasma current, countering this expansion. For a displacement of the plasma column in either the radial or vertical direction, the vertical field can be so arranged as to restore the plasma to its original position[13].

To provide a stable vertical position, the vertical field must curve such that the radial field component of the field off midplane provides a restoring force. To provide horizontal stability, the field strength must decay with major radius more slowly than the plasma's expansionary force, in which case the plasma will be restored to its original position if displaced either inwards or outwards. Both of these requirements on the vacuum field can be expressed by a quantity called the decay index, n:

$$n = -\frac{R}{B_Z}\frac{\partial B_Z}{\partial R} \tag{4.1}$$

and the condition on the decay index for positional stability is:

$$0 < n < 1.5 \tag{4.2}$$

with negative n denoting vertical instability (in either the upwards or downwards direction), and $n > 1.5$ denoting a horizontal instability.

The shaping field changes the decay index of the vacuum field, and can potentially lead to strong positional instabilities. Figure 4.1 displays calculations of the decay index at the midplane for an HBT-EP equilibrium with strong shaping (6.75 kA). This model assumes a simple filamentary plasma, a method that has been used with good success to capture the physics involved in equilibrium modeling and positional stability[69, 70]. It shows that the plasma has a small region of absolute stability between 86 and 89cm.

In the region of ideal positional instability, passive stabilization via image currents in conducting surfaces will slow the growth rate. Extending the results of studies on the effect of passive stabilization[15, 16] to HBT-EP, a decay index of $|n| > 8$ would be required for a mode to have a growth rate of 1000sec^{-1}. As shaped plasmas in HBT-EP disrupt within 4ms of the imposition

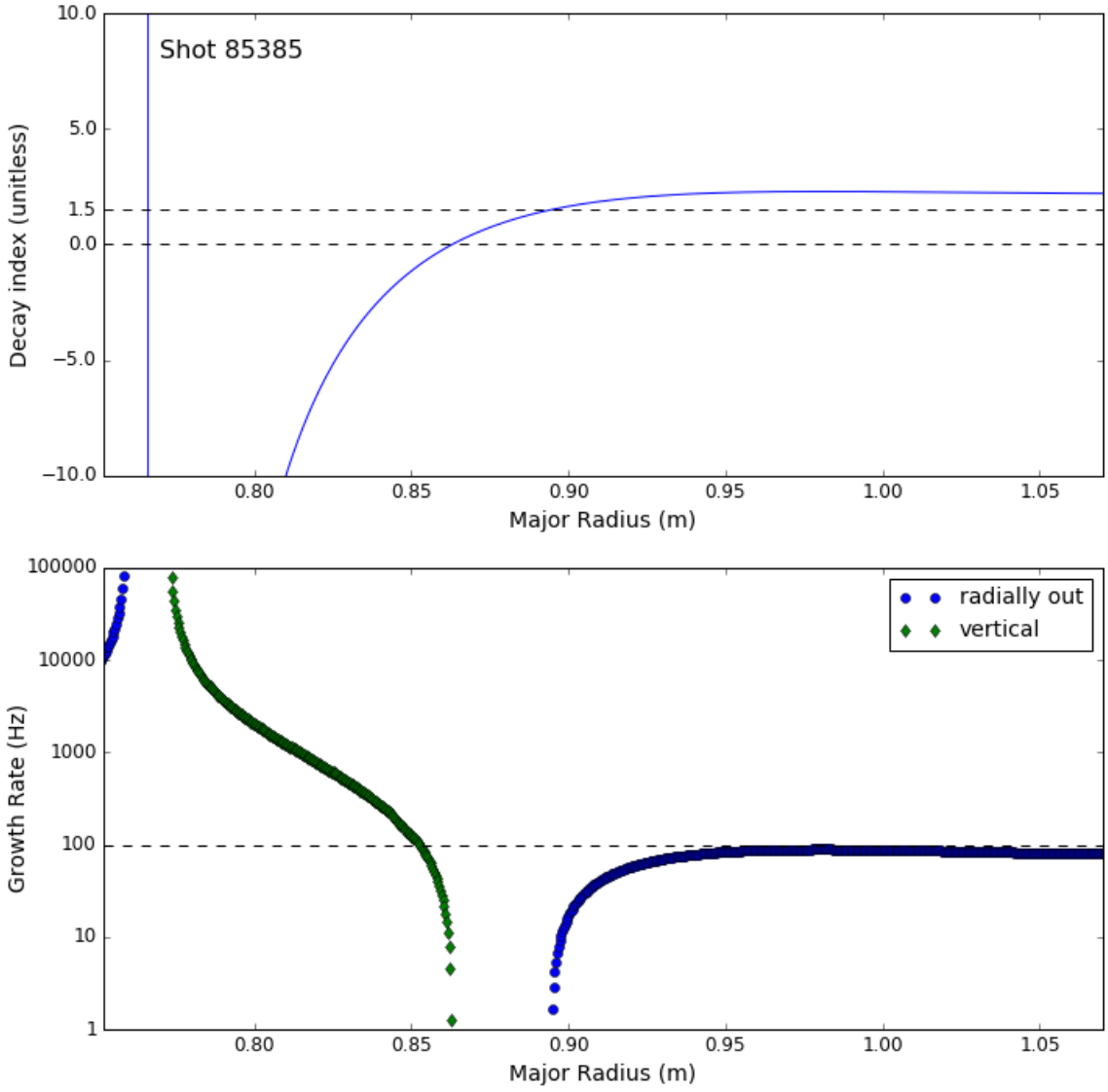

Figure 4.1: Top: Decay index of the vacuum fields for shot 85385, at 3.5ms, on the midplane. Bottom: Growth rates of the associated instabilities. A small region of stability exists, with a slow growing radially unstable region towards the outboard limiters. On the inboard side, there is a strong vertical instability, tending upwards.

of shaping, this growth rate is a practical minimum for the instability to have a noticeable effect. Figure 4.1 plots these growth rates for a filament at various locations on the midplane. We see that the outboard area is radially unstable but the characteristic growth time is greater than 10ms. Radially in from the stable region, within 85cm, there is strong vertical instability, in the upward direction. This inboard region is rarely occupied by the bulk plasma except during the final stages

of a disruption.

4.2 Demonstrating Diversion in Shaped Discharges

Any amount of current in the shaping coil will affect the local fields. This allows studies of limited non-circular cross section plasmas, but the intention of the shaping coil is to modify the fields to the extent that the plasma's outermost flux surface is defined by a magnetic separatrix. This equilibrium configuration is referred to as "diverted operation" throughout the paper. Below we explain the methods by which the plasma equilibrium of a given shot are modeled, in particular the flux surfaces.

4.2.1 Free Boundary Equilibrium Reconstruction

TokaMac is an equilibrium reconstruction code [11, 71, 72] to find a free-boundary equilibrium[73, 74]. Equilibria are reconstructed by seeking a least-squares best fit to equilibrium measurements. The reconstructions take as inputs the locations and currents of the vacuum field coils, the locations of the limiters, and plasma current. Free parameters are the location of the magnetic axis, core pressure, core pressure profile, and current profile.

The magnetic axis is not measured, but the current centroid is measured using the cosine rogowski[58]. As HBT-EP has relatively low poloidal beta, $\beta_p \sim 1$, the current centroid is used as a proxy for the magnetic axis. The pressure profile is not usually measured, but past Thomson scattering experiments[75, 76] on HBT-EP have measured electron densities and pressures that give core pressures in the 300Pa range. As reconstructed equilibria are in global force balance, the total plasma current and vertical field at the plasma midplane can be used to further constrain the total plasma pressure.

The helicity of the kink as measured by our sensor arrays, and the presence or absence of sawtoothing in the core as detected by a soft X-ray fan array, are used to apply upper and lower bounds on the q-profile. The q-profile is returned by TokaMac as output, and used to confirm the computed equilibrium. Figure 4.2 gives a schematic representation of the process of generating a TokaMac model of an HBT-EP equilibrium.

As a check on the accuracy of the equilibrium reconstructions, and to provide a further constraint on the geometry of shaped plasmas, a floating Langmuir probe is used to determine the location of

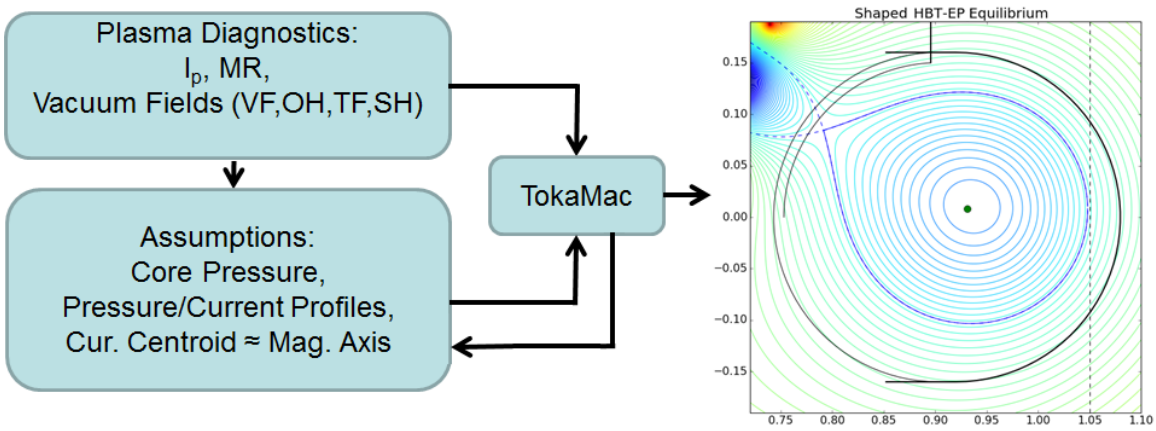

Figure 4.2: Schematic example of the inputs to TokaMac, as well as a plot of the flux surfaces returned for a shaped equilibrium.

the outboard edge in a shaped plasma. The probe is scanned through various flux surfaces of the plasma, the edge region, and/or the scrape-off layer depending on the insertion depth of the probe and the major radial position of the plasma. The voltage measured within 1mm of the plasma edge is taken as a benchmark for measurements of shaped plasmas.

The measured probe voltage is highly variable, as seen in Figure 4.3. In order to control for the variability, the near-edge Mach probe voltage is averaged across a 70 shot ensemble of unshaped plasmas. This ensemble was compiled from a separate run campaign[68], during which the insertion depth of the probe varied, but as the edge of a circular plasma is constrained, the location of the probe relative to the edge, $r - a$ is known. In Figure 4.4 the data is grouped by the distance from probe tip to plasma edge, $r - a$, into 1mm wide bins with red circles representing the average value, and the shaded region signifying a standard deviation in the data above or below. The dashed black line gives the average value of the probe signal when within 1 mm of the plasma edge, -7 V.

A 16 shot ensemble of shaped plasmas was analyzed, with the intention of determining the plasma minor radius by locating the edge voltage V_{LCFS} and determining the probe/major radius separation. As the location of the outboard plasma edge is unknown, $r-a$ is not used, rather $r-R_0$, with R_0 the plasma major radius and $r - R_0 = a$ when the floating voltage is found to be equal or close to V_{LCFS}. For this measurement, the probe tip was fixed at 105cm, and the plasma major radius allowed to vary. We locate the plasma edge by looking for regions where the probe signal is around -7V. This is plotted in Figure 4.5, and the average floating voltage is close to that of the edge region of a circular plasma for a minor radius between 12.8cm and 13.4cm.

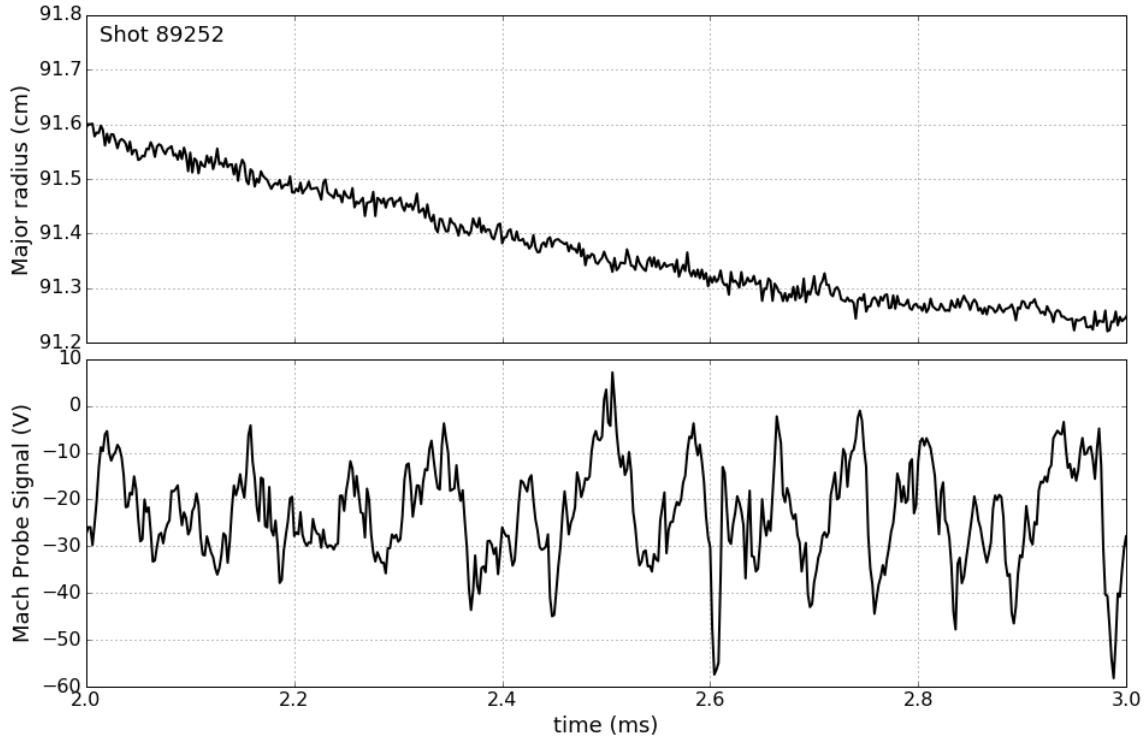

Figure 4.3: Floating Mach probe signal during a stable period of circular shot 89252. Plasma position is bounded within 4mm during a 1ms time window, with voltage varying in a 70V range. The Mach probe tip is located at 104cm, plasma edge is located at ∼106.5cm.

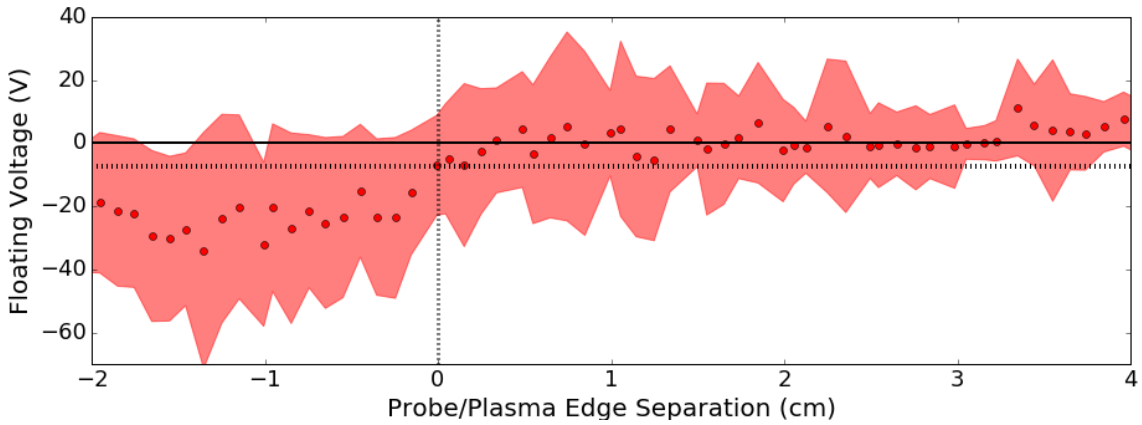

Figure 4.4: Mean and standard deviation of the circular shot ensemble data. X-axis is the distance from probe tip to plasma edge. Red dots are the average value of each bin, red shaded region is a standard deviation in each bin above and below, and the dashed grey line is the voltage found within 1mm of the plasma edge.

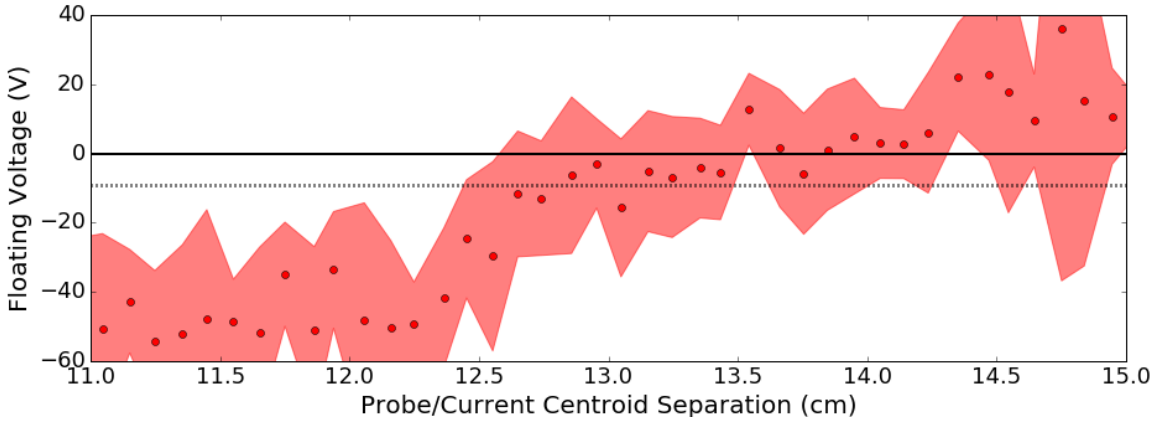

Figure 4.5: Mean and standard deviation of the 16 shot shaped ensemble. X-axis is distance from probe tip to plasma current centroid. Red dots are the average value of each bin, the red shading is one standard deviation above and below, and the dashed grey line is the edge voltage V_{LCFS} found for circular plasmas.

4.3 Representative Equilibrium of Shaped HBT-EP Plasmas

A plasma centered at 92cm and with a ∼13cm minor radius will not contact any limiting surface used to constrain circular plasmas. Contact with the strike-point limiter is ruled out by equilibrium reconstruction. As the value for plasma outboard edge was determined by averaging over an ensemble, the inputs to the equilibrium model are likewise derived from the data ensemble. The ensemble values for plasma current, vertical field current, ohmic heating current, and shaping current are arrived at by extracting those values when the major radius is measured to be between 91.6 and 92.2 cm and averaging. The free parameters in the equilibrium fit, core pressure, current and pressure profile, are constrained by specifying the magnetic axis, the q-profile and locating the outboard edge at 105cm. As seen in Figure 4.6, the X-point is a significant distance from the strike-point limiter, and the plasma is therefore modeled to be fully diverted.

4.4 Confirmation of Diversion via Magnetic Measurements

The existence of a poloidal field null is empirically confirmed by looking at the signal from the poloidal array during a real shot. The vacuum poloidal field is calculated from the gradients of the flux contours of the equilibrium reconstruction. This field is plotted in Figure 4.7, showing a poloidal field reversal at poloidal array sensors 29 and 30. We therefore look for this reversal on

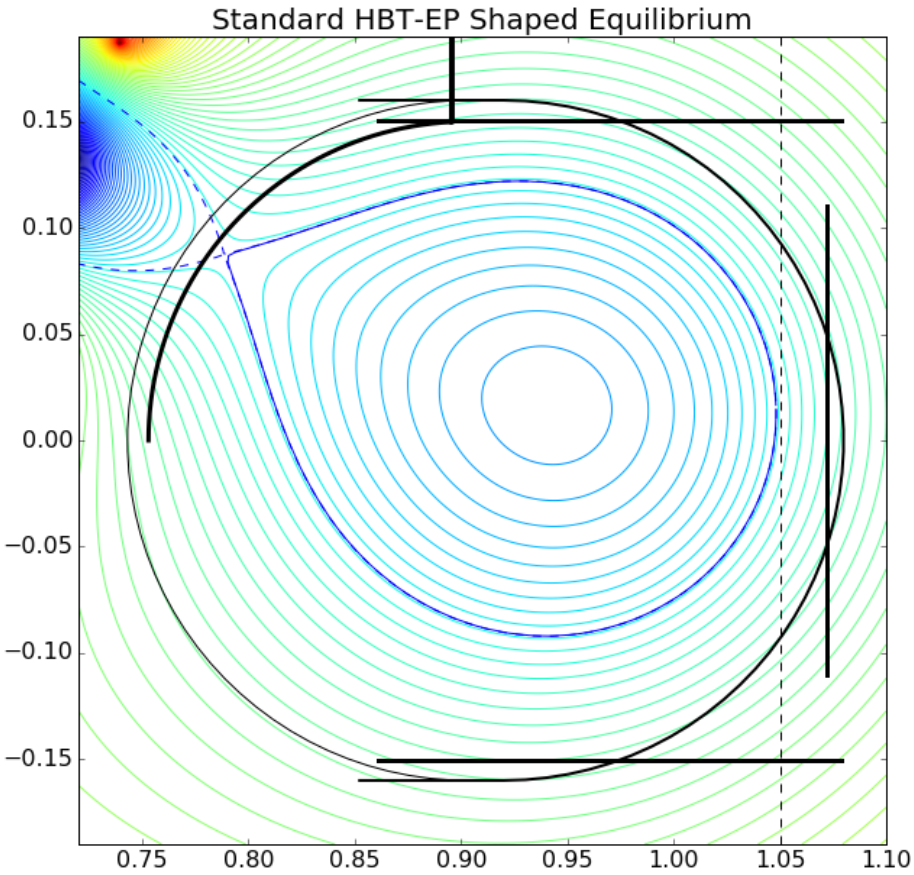

Figure 4.6: HBT-EP shaped equilibrium flux surfaces. Solid black lines are material surfaces. Dashed line is probe location.

those sensors' measurements of poloidal field during shaping experiments.

Shot 90099 is a shaped shot representative of the ensemble. At 3.2ms, the shaping coil has reached its peak value, and the plasma parameters are close to those of the ensemble reconstructed equilibrium. The external coil currents, plasma current and plasma position are similar to the values observed when the plasma edge was observed at the probe location.

The average value of the measured field at each sensor is determined by 3rd order polynomial fit to the signal between 2ms and 4ms. The value of this fit at 3.2ms for each sensor in both poloidal arrays is plotted against the computed equilibrium signal in Figure 4.8. Looking at the measured signal, we see that there is a reversal in the poloidal field where expected, demonstrating that a diverted plasma can be created in HBT-EP.

During a recent upgrade, high precision metrology[77] was performed on HBT-EP that suggests

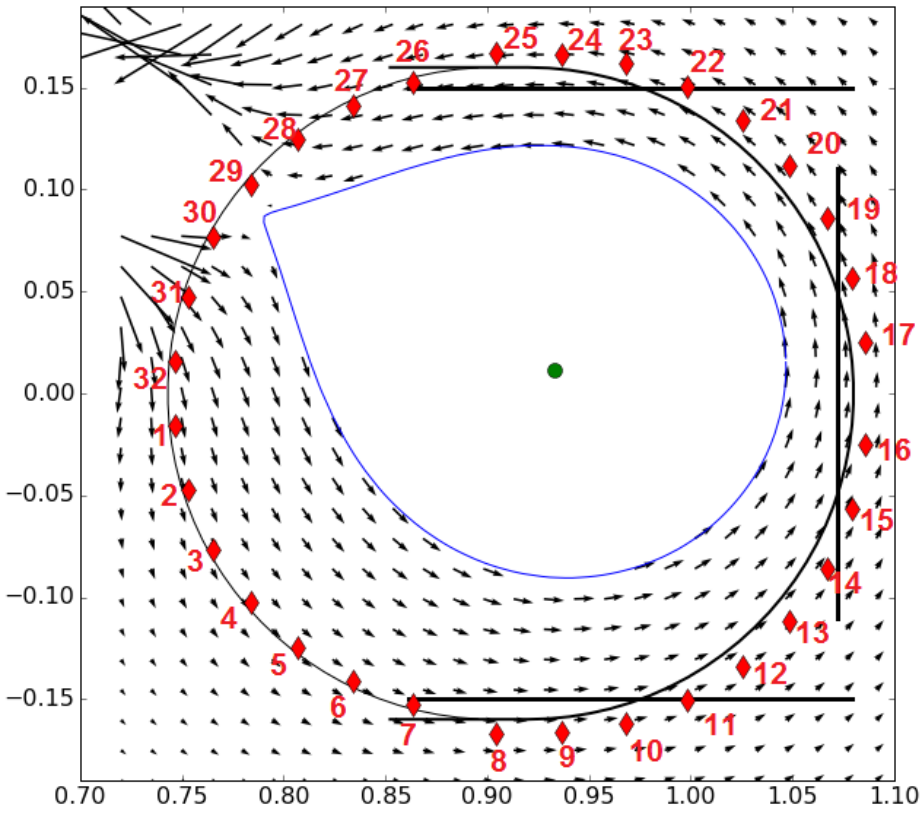

Figure 4.7: Vacuum fields computed from TokaMac model of poloidal flux for a shaped equilibrium. Poloidal array sensors are red diamonds. Sensor numbering scheme begins with the sensor just below the inboard midplane as sensor 1, and proceeding counter clockwise to the sensor just above the inboard midplane, as sensor 32.

that individual poloidal array sensors can be mispositioned by as much as 3mm and misaligned by as much as 5° on HBT-EP. The blue 'x's in Figure 4.8 represent an estimate of the largest measurement errors to be expected from mispositioning and/or misalignment, with an excess disagreement arising from shaping coil mispositioning. The X-point localized errors are larger than can be accounted for by misplaced or misaligned sensors, suggesting that the shaping coil is displaced from its nominal position during the period at which the coil is conducting peak current. Though there is some disagreement between measurement and calculation, both poloidal arrays have sensors well inside the region of poloidal field reversal, i.e. behind the X-point. These sensors see the expected poloidal field reversals, with a reversed field magnitude equal to or larger than what is expected, leaving no doubt that diverted plasmas were created.

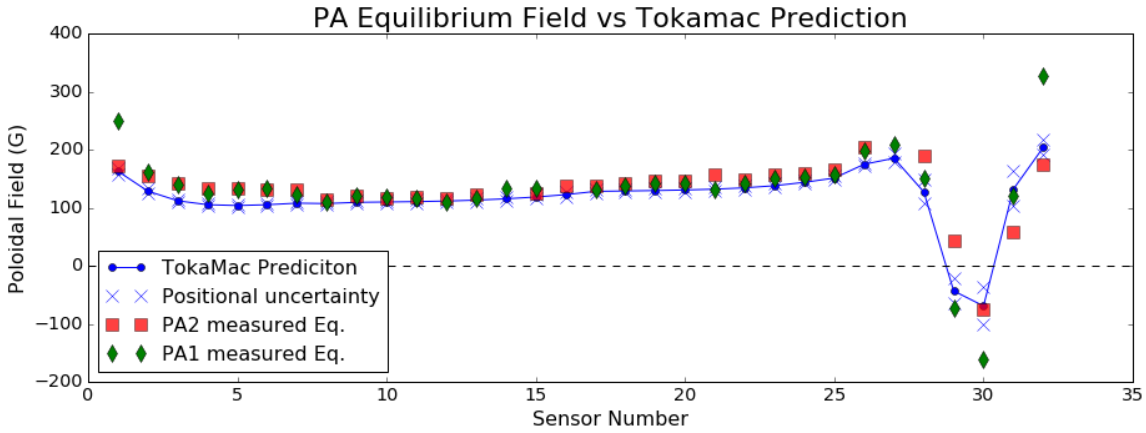

Figure 4.8: B_p calculated by TokaMac compared with the measured equilibrium poloidal field during shot 90099 at 3.2ms, on each of the functioning PA1 and PA2 sensors. Blue 'x's represent the worst case error from sensor mispositioning and/or misalignment.

4.5 Summary

The equilibrium of a shaped plasma is calculated to be ideally unstable to axisymmetric instabilities, but wall stabilization increases the growth time of the instability to the point that it is comparable to the lifetime of the plasma. Free-boundary equilibrium reconstructions of shaped plasmas have been performed, with those reconstructions constrained by direct measurements of the outboard edge region. Equilibrium models incorporating the results of this measurement unambiguously show full diversion in shaped HBT-EP plasmas as measured by poloidal arrays of magnetic sensors. Comparing direct measurements of poloidal field to a TokaMac equilibrium model shows the expected poloidal field inversion near the X-point, and the magnitude of the field inversion is equal to or larger than that of the model. This result establishes that HBT-EP is capable of creating diverted plasma discharges, that the database of shaped shots includes a large number of such discharges, and opens the way for investigation of MHD fluctuations near the X-point of diverted plasmas.

Chapter 5

Kink Modes in Shaped and Circular Plasmas

The structure of kink modes observed in shaped plasmas is compared to that of circular plasmas. Analysis techniques for separating the equilibrium signal from the fluctuations, and individual modes from the bulk fluctuations, are discussed. The most unstable external kink mode often dominates the eigenmode spectrum, permitting description of mode amplitude and structure by inspection. Applying the biorthogonal decomposition to the fluctuations separates the dominant mode from any remaining background signal. The structure of the dominant kink is determined using biorthogonal decomposition and compared across shaped and circular equilibria. It is found that the modes in shaped plasmas tend to have a lower m-number than circular plasmas with similar major radius and plasma current. When compared to circular plasmas with comparable mode helicity, the structure is seen to be similar across most of the poloidal circumference, but with a short wavelength feature localized near the X-point of shaped plasmas.

Diverted HBT-EP plasma equilibria appear to be more susceptible to disruption than circular, limited plasmas. A typical disruption of each equilibrium is discussed, and MHD preceding and following the disruption are observed. The precursors are similar in frequency and amplitude, as is the growth of the kink immediately following the thermal quench, but the post-disruption behavior is qualitatively different. Circular plasmas disrupt in two distinct phases with the large post-disruption external kink signal increasing in amplitude and frequency during the latter half

of the current quench, while in shaped plasmas the post-disruption kink is not observed to change rotation frequency or change in amplitude.

This chapter is organized in five parts. First, three equilibria, two circular and one shaped, are introduced, and their equilibrium parameters estimated to predict the likely structure of the external kink. Then, the equilibrium poloidal field is separated from magnetic fluctuations and the structure is observed. Next, the process by which the biorthogonal decomposition is used to separate the fluctuations of the rotating external kink from any other background signal is described. This is followed by comparison of the structure of the external kink in shaped and circular equilibria using the biorthogonal decomposition. Finally, the manner in which the two types of equilibria disrupt are compared, including the rate of dissipation of internal energy, as well as the amplitude and frequency of the $n = 1$ MHD oscillations before and after the disruption occurs.

5.1 Example Discharges for Mode Comparison

Figure 5.1 shows the basic equilibrium parameters of the plasmas that will be discussed throughout the remainder of this thesis. Shots 89200 and 91329 are circular in cross section, while 90837 is shaped. Shaping is imposed starting at 1ms, and the shaping field has reached its steady state value by 2ms. Shot 91329 has similar plasma current and radius to shaped shot 90837, while shot 89200 has higher I_P, a smaller major radius, and a larger minor radius than 91329. The cylindrical approximation of safety factor q_* is calculated according to Eq. 1.14 for all plasmas in the third subplot, and in the fourth, q_* for shot 90837 is calculated according to Eq. 1.16, using the minor radius and elongation given by equilibrium reconstruction at 3ms. A significant shift in q_* for the shaped plasma is observed, and, edge helicity is expected to be more similar between 90837 and 89200 than between 90837 and 91329 despite the difference in equilibrium parameters.

5.2 Observation of External Kinks

Removing the background equilibrium prior to analysis is crucial for properly isolating MHD modes. This is done by fitting a low-order polynomial to the signal as shown in Figure 5.2. The low degree of the polynomial prevents it from fitting to any but the lowest frequency components of the window under consideration. Shaped plasmas require more care when subjected to this process than circular

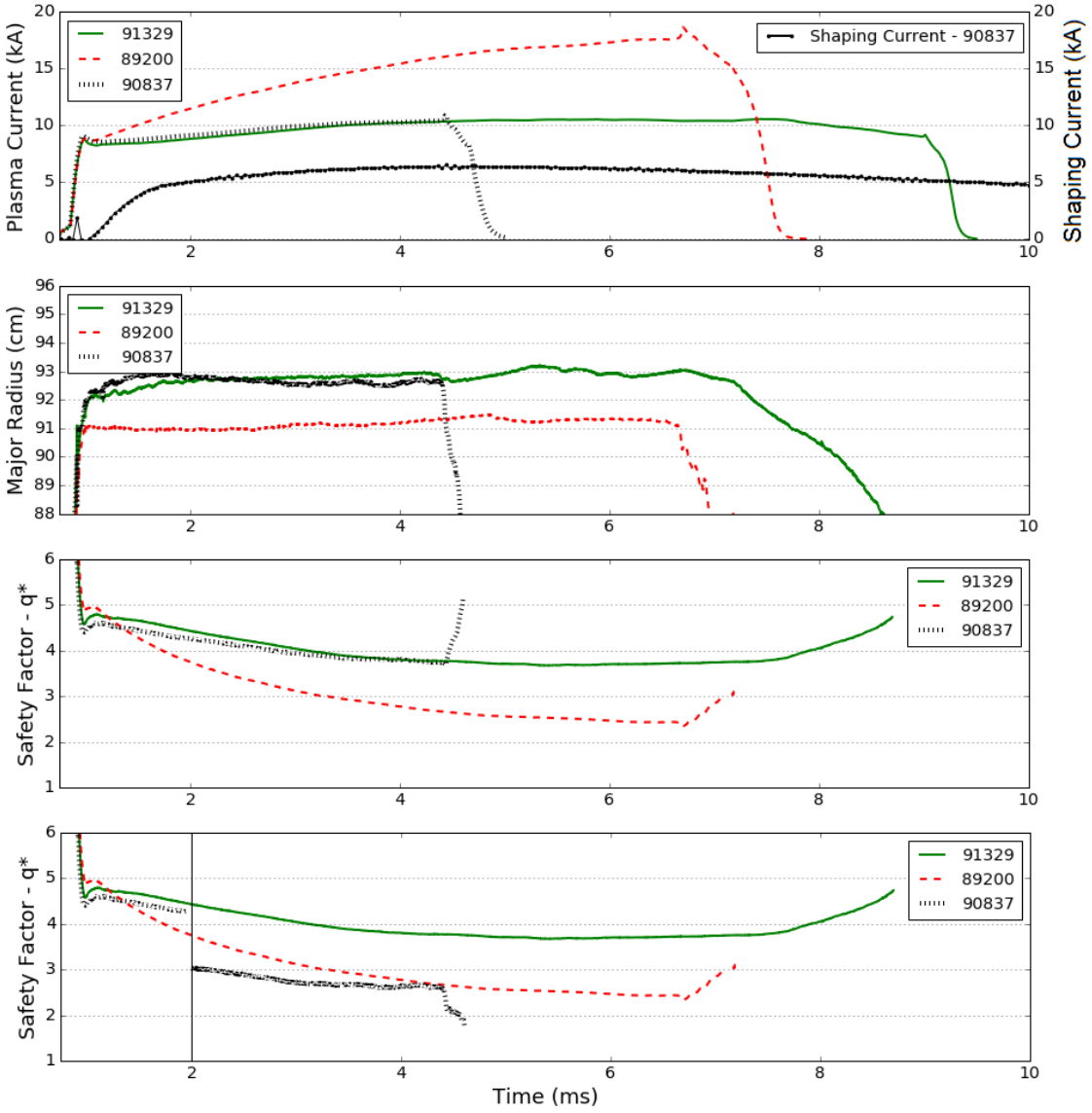

Figure 5.1: Equilibrium parameters for shots 89200, 90837, and 91329. Shots 89200 and 91321 are circular and 90837 is shaped. Full shaping is imposed by 2ms, at which time q_* calculated using circular approximations becomes inaccurate. From the top: Plasma and shaping current, plasma major radius, q_* using circular approximation, q_* using minor radius and κ from equilibria reconstructions.

ones, as the equilibrium undergoes a large change when shaping is imposed, and they tend to be more disruptive and short-lived. To ensure a good fit, the limiting requirement is a long enough time window between the imposition of steady-state shaping and disruption. This method will be discussed again in more detail in a later chapter, when resonant response of the plasma modes to

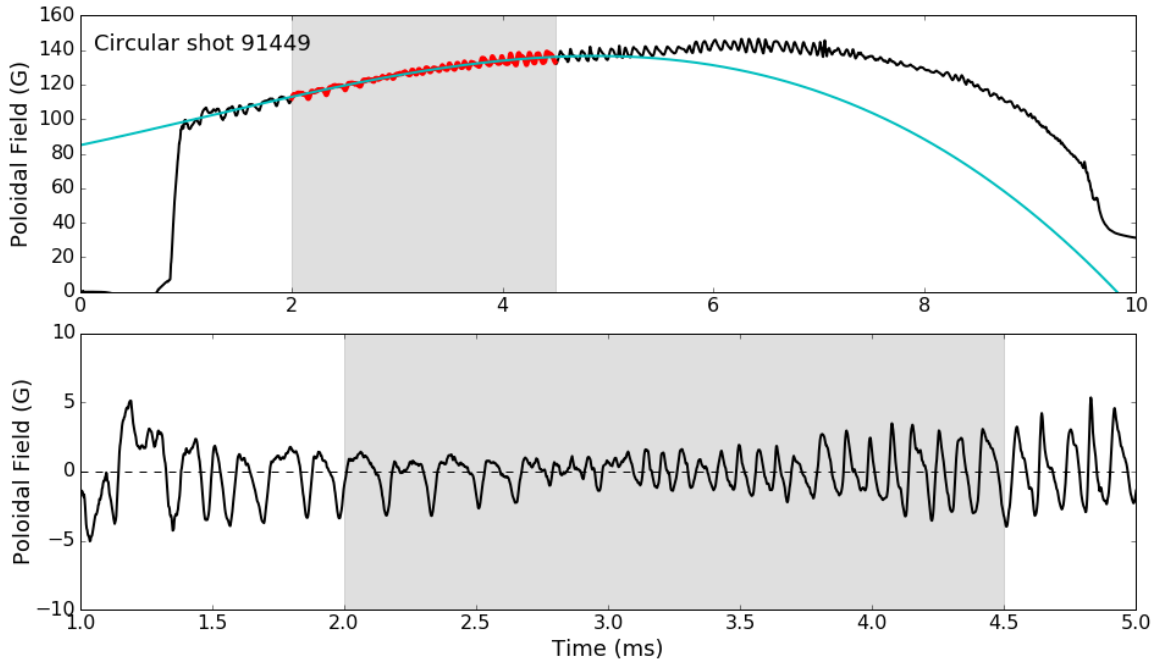

Figure 5.2: Top: Equilibrium subtraction for signal on a poloidal array sensor during circular shot 91449. A 3^{rd} order polynomial (cyan) is fit to the data (red) in the shaded region.
Bottom: The fluctuations after subtraction of the fit to the equilibrium signal. The fit is seen to become unrepresentative outside the fitting window.

external perturbations is discussed.

Frequently the modes under study can be separated from the total signal with no more complicated processing than subtracting the equilibrium signal. Though our plasmas display multimode behavior[60, 76], sub-dominant modes are often small enough in amplitude relative to the dominant mode to be disregarded.

Figures 5.3 and 5.4 display the evolution, as well as the poloidal and toroidal structure, respectively, of the fluctuations in shot 89200 after removing the equilibrium using a polynomial fit. The contour plots are of the time varying signals from our sensor arrays over a time window, and the scatter plots are created by taking sections of the contour in either space or time. As our sensor sets are regularly spaced and toroidally or poloidally complete, depending on the set, mode helicity can be read off the spatial sections. The evolution of the amplitude and fluctuation frequency can be read off the temporal sections. It should be stressed that the contributions of all MHD modes in the plasma's multimode spectrum are observed simultaneously, so for this method of analysis to be valuable, one mode must dominate the spectrum.

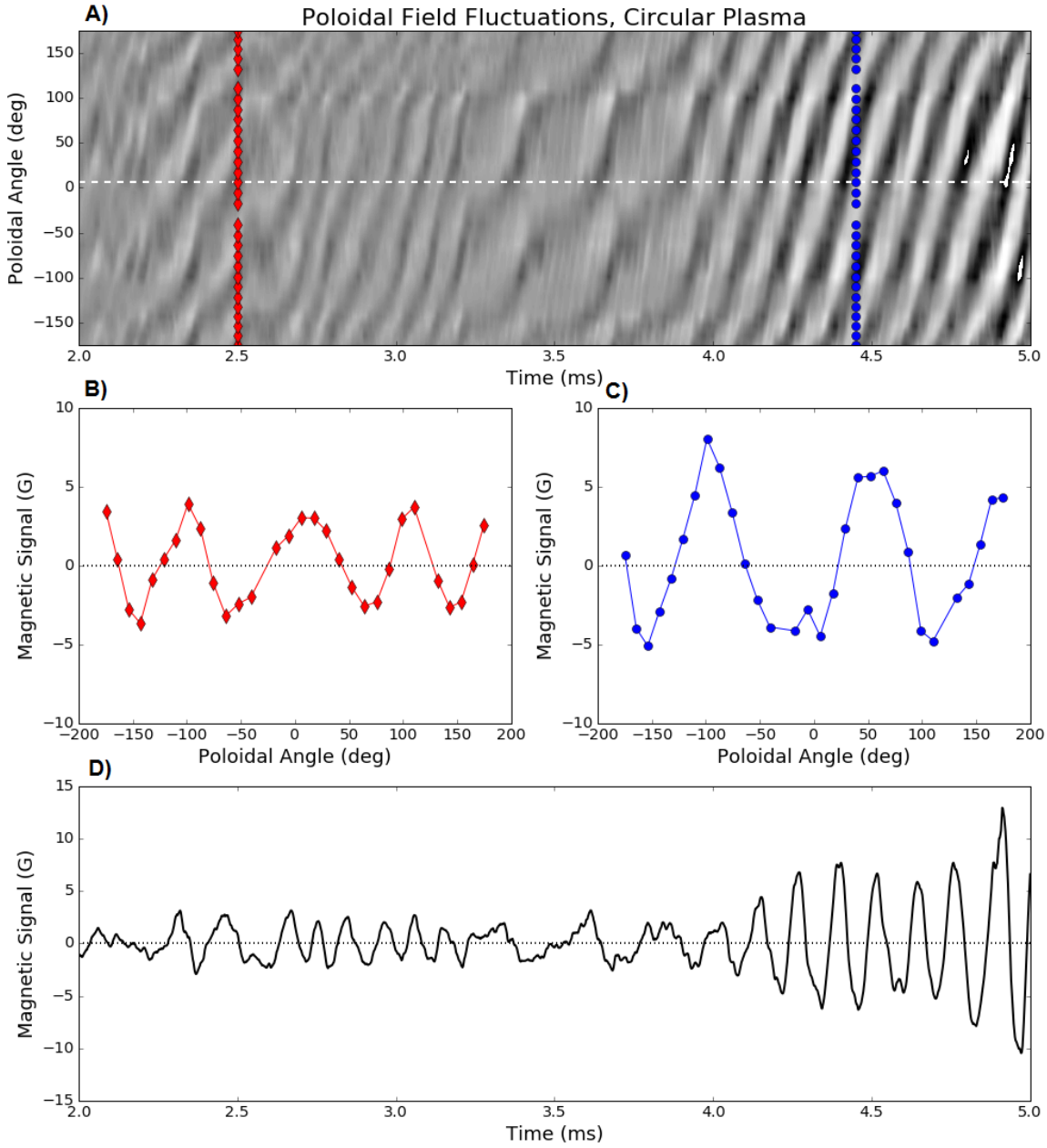

Figure 5.3: Raw B_p fluctuations of shot 89200, as measured on Poloidal Array 2. A) Contour plot of fluctuations obtained using a 3rd order polynomial fit to the equilibrium. Red diamonds and blue circles represent functioning PA2 sensors. B) The signal on the poloidal sensors at 2.5ms. The structure is $m = -4$. C) The same signal at 4.45ms. The structure of the mode has changed to $m = -3$. D) The signal on the sensor at $\theta = 5.9°$ (dashed line in plot A) throughout the time of observation. Mode amplitude is $\leq$5G during the $m = -4$ period, with a slowing and reduction in amplitude of fluctuations before resuming smooth rotation and growing as $m = -3$ to 10G. Note the apparent locking of the mode at 3.5ms during the transition from $m = -4$ to $m = -3$ at 3.5ms

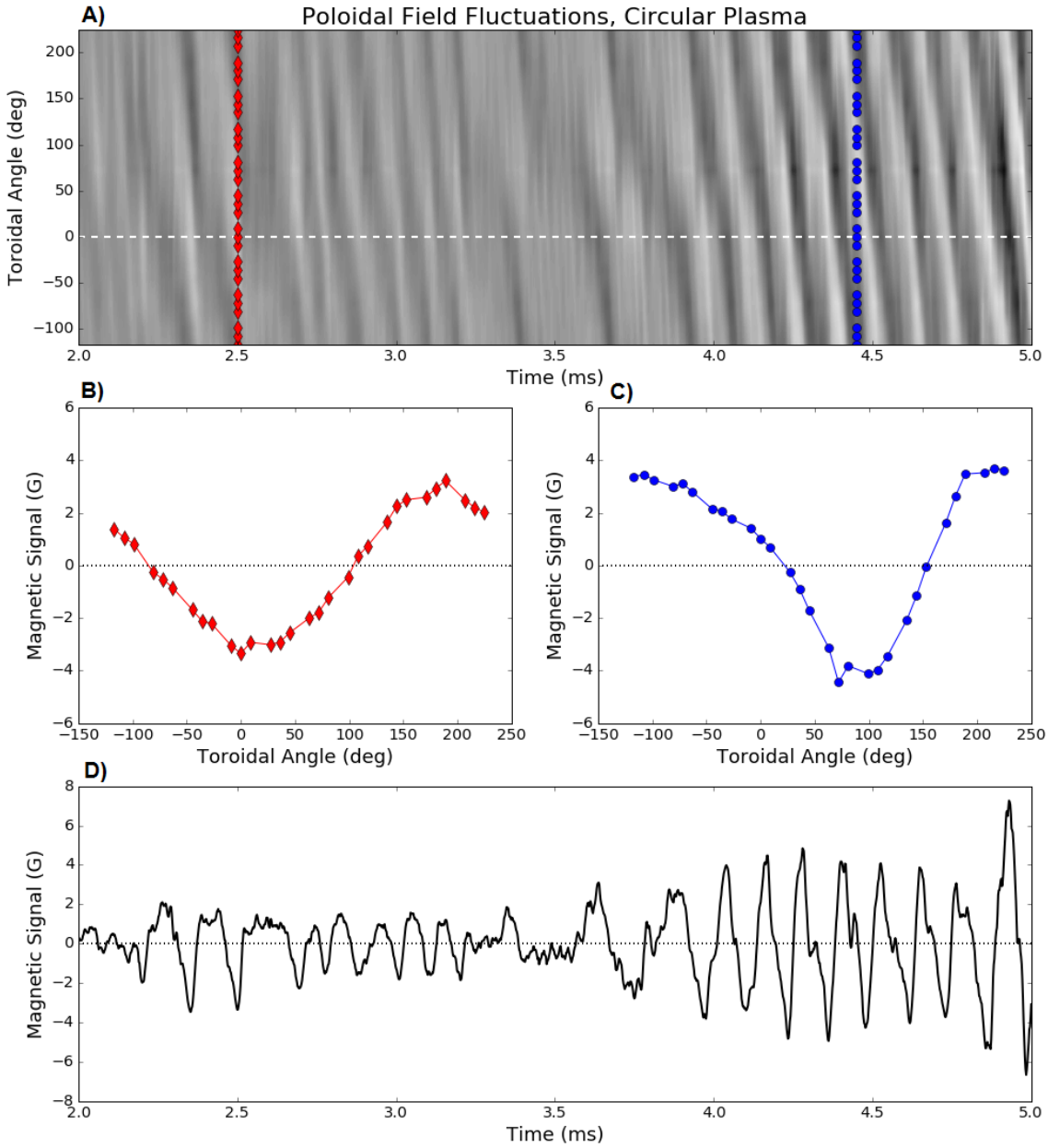

Figure 5.4: Raw B_p fluctuations of shot 89200, as measured on the Toroidal Array. A) Contour plot of fluctuations obtained using a polynomial fit to the equilibrium. Red diamonds and blue circles represent functioning TA sensors. Note that the y-axis is now toroidal angle. B) The signal on the toroidal sensors at 2.5ms. The structure is $n = 1$. C) The same signal at 4.45ms. The toroidal structure of the mode remains $n = 1$. D) The signal on the sensor at $\phi = 0$ (dashed line in plot A) throughout the window of observation. Mode amplitude is $\leq$4G during the $m = -4$ period, with a slowing and reduction in amplitude of fluctuations before resuming smooth rotation and growing as $m = -3$, $n = 1$ to 6G. Note the apparent locking of the mode at 3.5ms.

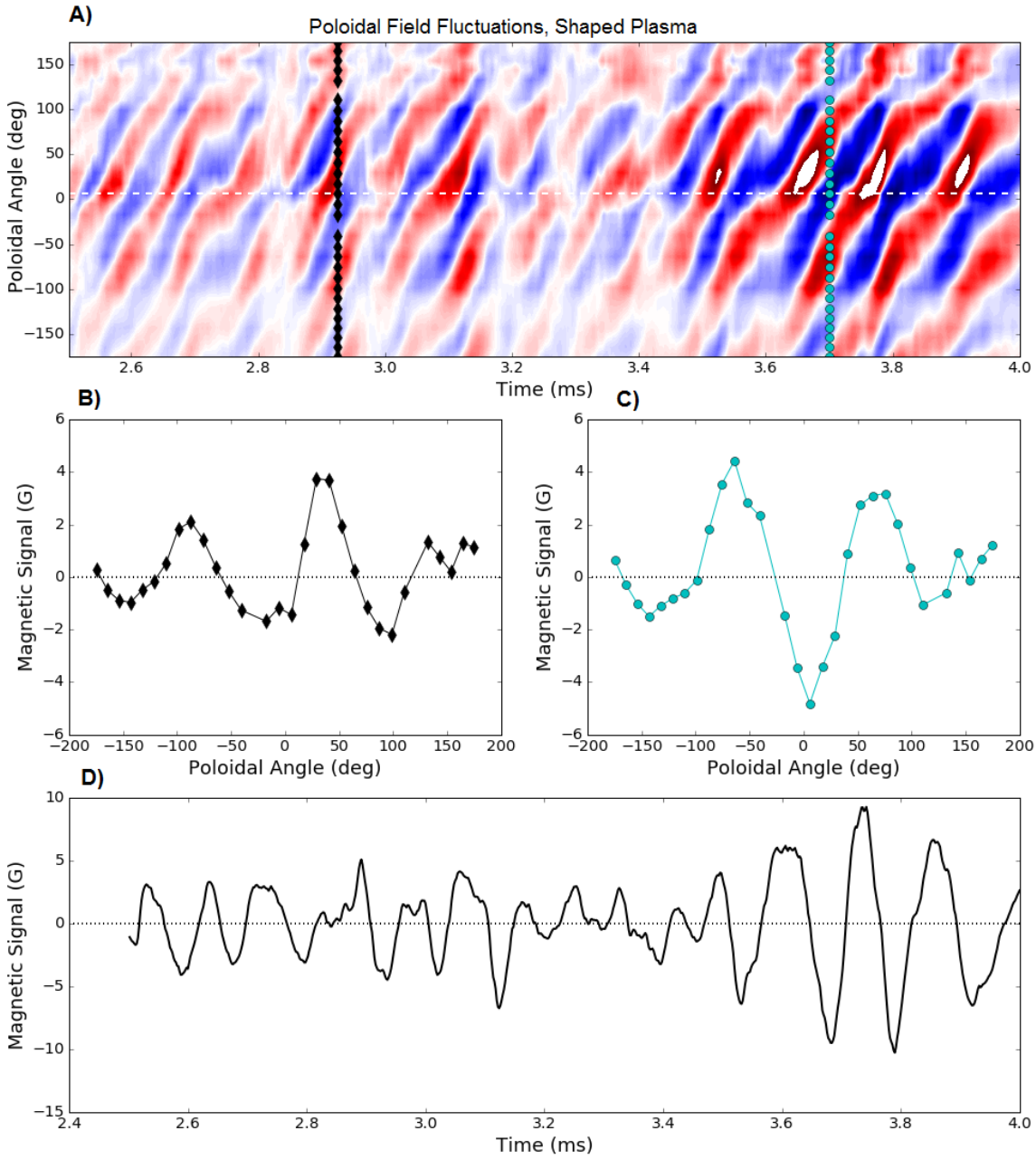

Figure 5.5: Raw B_p fluctuations of shaped shot 90837, as measured on Poloidal Array 2. A) A contour plot of fluctuations obtained using a 3rd order polynomial fit to the equilibrium in the region from 2.5-4.0ms. High-contrast color scheme is used to allow observation of low amplitude fine structure near X-point. X-point localized (140°-150°) feature is oscillating, and therefore not due to SH coil pickup. Black diamonds and cyan circles represent functioning PA2 sensors. The white dashed line is the location of PA2 sensor 17 (outboard midplane). B) The signal on the poloidal sensors at 2.93ms. The structure is $m = -3$, with the structure near the X-point visible. C) The signal on the poloidal sensors at 3.7ms. The structure remains $m = -3$, with the structure near the X-point still visible. D) The signal on the sensor at $\theta = 5.9°$ (dashed line in plot A) during the time of observation. Mode amplitude is $\leq$6G before the minor disruption just after 3.5ms, and rises to $\sim$10G after.

Figure 5.5 shows the evolution of the poloidal structure of the fluctuations from a shaped shot, 90837. As this mode is also $n = 1$, as indeed are the dominant external kinks in all of the equilibria studied in this thesis, the toroidal structure is omitted. Shaping is imposed beginning at 1ms, and is fully established by 1.8ms. The window of observation begins at 2.5ms, to allow vacuum vessel eddies near the X-point sensors to decay, and ends at 4ms, 0.3ms before disruption. We see that the mode structure remains roughly constant, dominated by an $m = -3$ like mode, with fine structure visible near the X-point, in the vicinity of 145°. The contour plot color scheme is changed from the greyscale of Figures 5.3 and 5.4 to add contrast to the low-level X-point detail.

5.2.1 Biorthogonal Decomposition

Though the dominant mode is frequently visible on inspection, subdominant modes or imperfectly subtracted equilibrium signals can affect the apparent mode structure and/or evolution. Isolating the signal of the dominant mode from all background signals is necessary to precisely characterize the structure of the external kink.

The biorthogonal decomposition isolates coherences in a dataset without regard to a preselected basis. A frequently used method in signal analysis[78], it is also known as the singular value decomposition. This method has been used extensively by the plasma physics community[79–82], has been thoroughly investigated for its suitability to HBT-EP[76], and has been integral to much of our subsequent research[42, 83, 84]. Given a set of concurrent time-domain signals sampled at different physical locations, the BD returns a set of eigenmodes orthogonal in both time (chrono) and space (topo), and their associated eigenvalues. Traveling waves are represented as a phase shifted sine/cosine-like pair of modes with very similar singular values, spatial structure, and temporal evolution, though with a 90° phase shift.

With HBT-EP's 216-element sensor set, the basis set will be composed of 216 distinct and mutually orthogonal modes. It is commonly observed that the preponderance of spectral energy is distributed among a few dominant modes. These modes are ordered in terms of their singular value σ_i, which represents the proportionate amount of coherent information each mode represents. The set of eigenvectors will be determined arbitrarily, with no a priori assumptions as to the form of the basis functions. Because of this, the lack of a clear Fourier decomposition for the poloidal structure of the modes, the time-varying amplitude and frequency of the modes, and the non-functional sensors in our array, can all be accommodated with no generation of artifacts or crosstalk between modes[42].

The method is less robust to large changes in the plasma coupling to sensors[76], so all plasmas will be analyzed during periods when the major radius is stable ($\leq$ 1cm/ms), and at least 200 μs from any minor disruption.

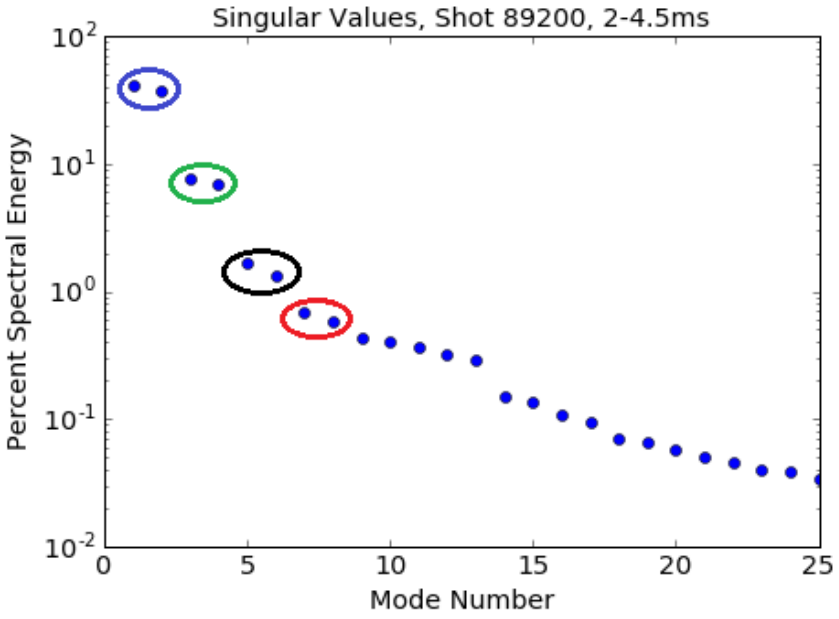

Figure 5.6: First 25 BD singular values, plotted as a percentage of the total spectral power ($100\sigma_i^2/\Sigma\sigma_j^2$) in each mode. Over 97% of the spectral power of the fluctuations is contained in the first eight modes, and over 78% in the first mode pair alone. Pairwise grouping of coherent traveling wave-like modes is highlighted, color code is the same as in Figure 5.7.

Once the modes are separated, it is possible to extract phasing and amplitude information from the chrono, providing the time history of the evolution of the mode strength and fluctuation frequency:

$$\chi_1 \simeq A(t)\cos(\phi(t)) \tag{5.1}$$

$$\chi_2 \simeq A(t)\sin(\phi(t)) \tag{5.2}$$

$$A(t) \simeq \sqrt{\chi_1^2 + \chi_2^2} \tag{5.3}$$

$$\phi(t) \simeq \tan^{-1}(\chi_2/\chi_1) \tag{5.4}$$

As an example, shot 89200 is subjected to Biorthogonal Decomposition over the same window in Figure 5.3. As the kink modes of interest are traveling waves, they are represented as an orthogonal

'sine/cosine' pair with roughly equal singular value (σ) amplitude. When the singular values are plotted logarithmically, as in Figure 5.6, we see that the first eight modes are arranged in four pairs

By selecting and plotting any topo mode one can see the toroidal or poloidal structure of the mode. Likewise, by selecting a chrono, one can observe the time-dependent frequency of periodic fluctuations, as well as the evolution of the modes' amplitude and oscillation frequency over time. With proper shot development, noise and artifacts can be reduced such that as many as six or eight can be isolated for a study of multi-mode physics[60, 76], but only the most dominant two modes of any decomposition, representing the dominant traveling mode, will be considered in this thesis.

Figure 5.7 illustrates this with plots of mode shape and the temporal evolution of the mode amplitude. The dominant mode is the $m = -3$, $n = 1$ mode that was observed at the latter part of the window. The mode initially has small amplitude, and grows until at late times it is of higher amplitude than all other eigenmodes. The secondary mode is the $m = -4$, $n = 1$ mode that we see dominating the spectrum at the beginning of the window, with its amplitude minimal by 3.5ms. The third mode pair, however shows a previously undetectable $m = -6$, $n = 2$ mode that grows in amplitude with the $m = -3$, $n = 1$ mode. Finally, an $m = -7$, $n = 2$ mode is detected with low amplitude.

5.3 Comparison of External Kink Structure Between Shaped and Circular Equilibria

We first compare the structure of the dominant mode in circular shot 91329 to that of shaped shot 90837. The plasmas have similar major radius and plasma current, as seen in Figure 5.8, and the biorthogonal decomposition is performed after the shaping field has reached steady state.

We see that the wavelength of the mode in the shaped plasma is longer than that of the circular plasma, which is expected, due to the smaller cross sectional area of the shaped plasma leading to a q_{95} lower than the circular plasma's q_*. The structures of the modes are displayed in Figures 5.9.

We see the amplitude of the mode is largest at the shell mounted sensors ($|\theta| \leq 90°$) in the modes of both plasmas. This is due to eddies in the shells suppressing the normal component of the modes and amplifying the poloidal component. Both plasmas also have outboard major radii and will couple more strongly to the sensors that they are closer to, which in this case are the shell mounted sensors. We also note a rapid fluctuation in the structure of the shaped mode near the

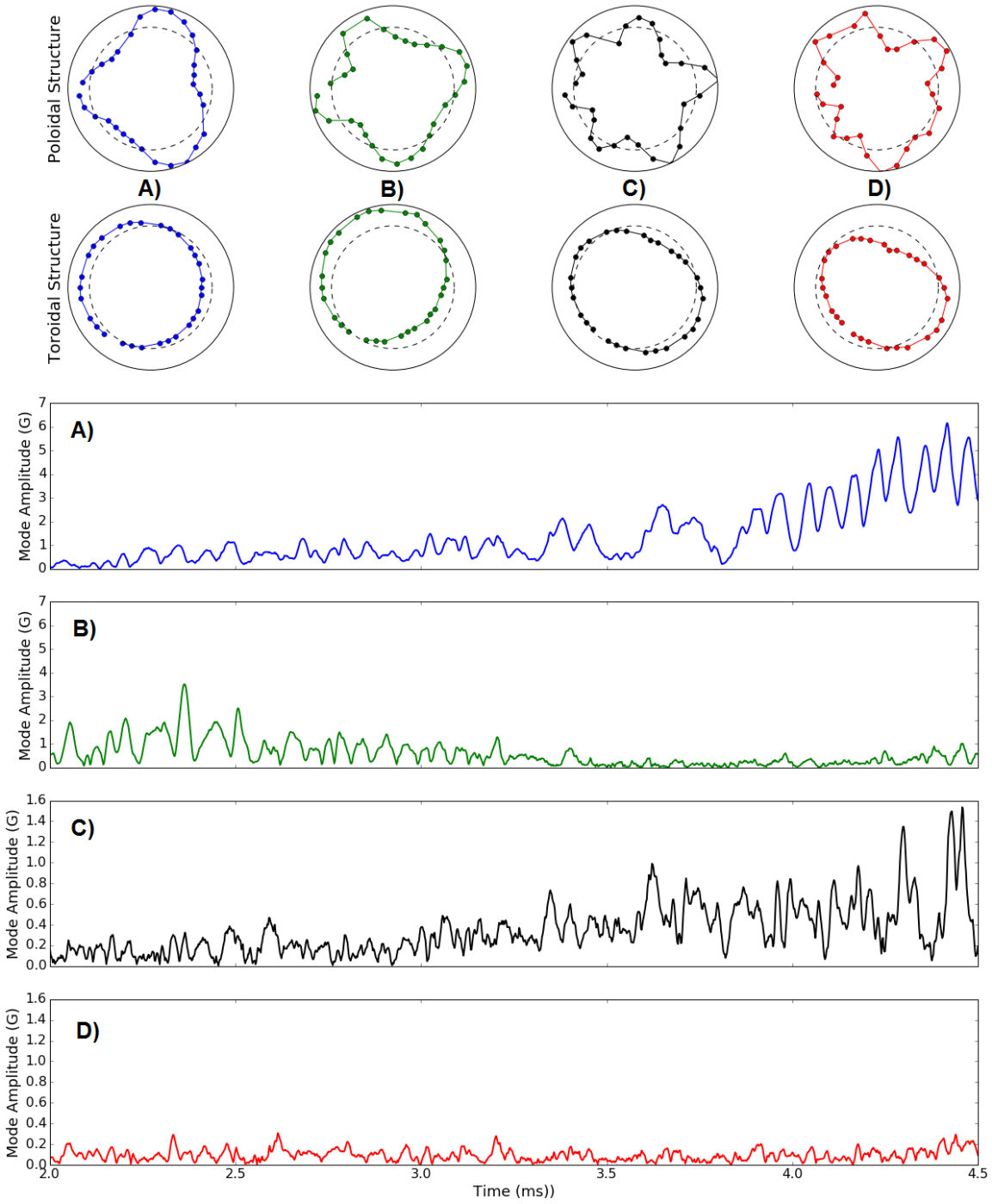

Figure 5.7: BD topo and chrono-derived amplitude, first 4 coherent modes, 2-4.5ms in shot 89200. A) $m = -3$, $n = 1$ and B) $m = -4$, $n = 1$ modes are isolated as in Figures 5.3 and 5.4, but individual amplitudes are now disambiguated. Further, two $n = 2$ modes with poloidal mode numbers C) $m = -6$ and D) $m = -7$ are also distinguishable. Note the differing scales for the $n = 1$ and $n = 2$ amplitudes.

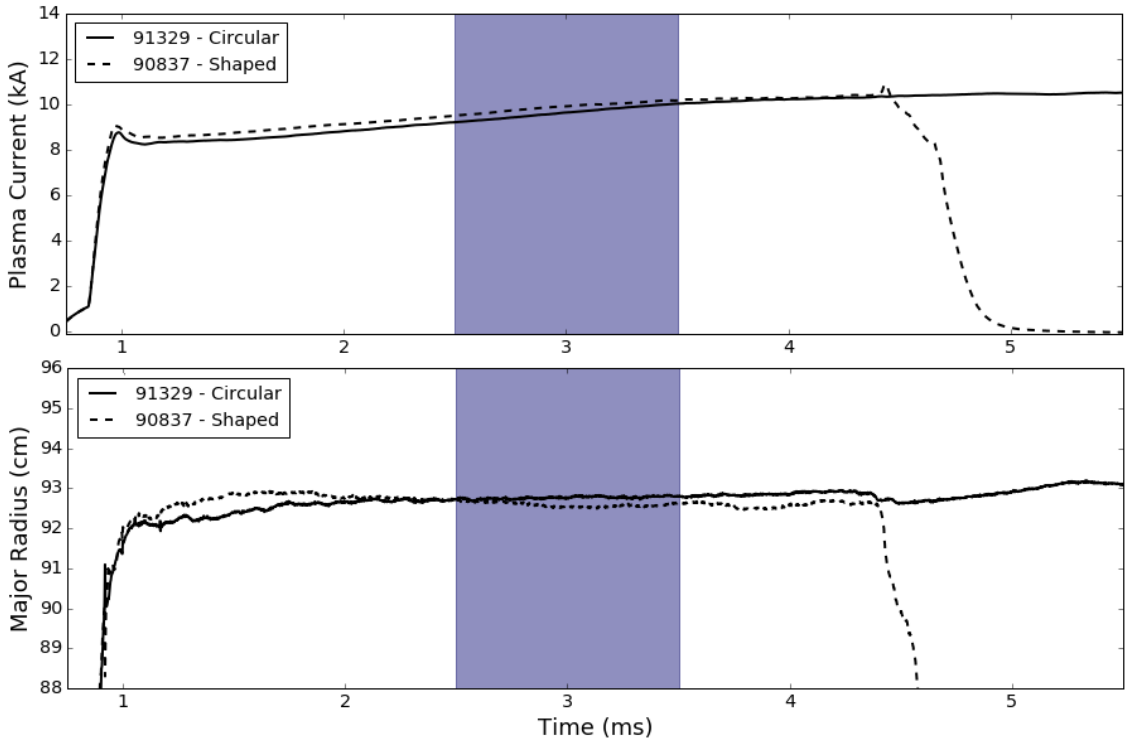

Figure 5.8: Equilibrium parameters for circular shot 91329 and 90837. Similar equilibrium quantities (vacuum fields, I_p, MR) would indicate similar MHD structure, if plasma shapes were the same. The time window in which the BD is performed in the same in both cases, the shaded region from 2.5-3.5ms.

X-point in the shaped plasma ($\theta \sim 150°$).

The shaped plasma is next compared to a circular plasma with similar q_*. The time periods during which the BD analysis is performed for each shot are shown in Figure 5.10. The plasma in shot 89200, being 2cm inboard with respect to shot 90837, has less poloidal field amplification from the conducting shells, but the number and poloidal locations of the peaks in both plasmas correspond well. Figures 5.11. We see that the modes are largely similar, again, except at the X-point.

This represents the first observation of this X-point localized feature in diverted equilibria using magnetic sensors. This feature is consistently observed in the external kinks of diverted equilibria, at this poloidal angle, with this short wavelength, and at this amplitude relative to the rest of the mode. As will be discussed in Chapter 7, the MHD response of these equilibria to external magnetic perturbations also displays this feature.

Detection of such a high m-number signal requires densely placed sensors to resolve the feature at all. The sensors must also be close to the plasma surface, as high-m components of the field

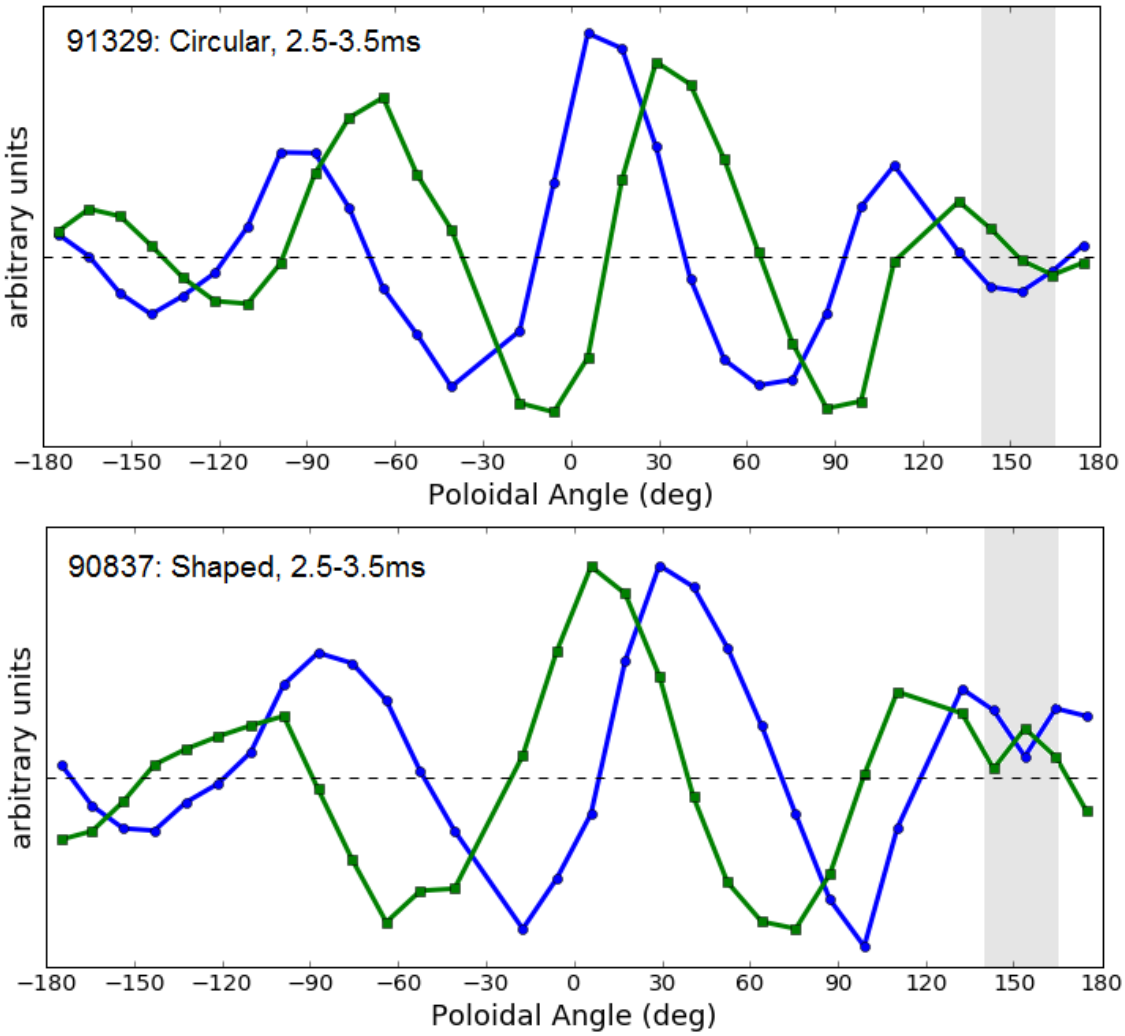

Figure 5.9: The dominant $m = -4$ mode pair extracted from unshaped shot 91329 and the dominant mode pair extracted from shaped shot 90837. Note that in both cases, amplitude is peaked where $-90° \leq \theta \leq 90°$, due to eddy current amplification of the poloidal field, and the plasma position in the chamber. The mode in the shaped plasma is primarily $m = -3$, but note the distinct modulation of the structure at the X-point near $\theta = 150°$.

spectrum decay more rapidly away from the plasma surface, as $(\frac{a}{r})^(m+1)$. And finally, most advanced tokamaks exhaust far too much heat at their X-point to locate magnetic sensors in that region. In order to establish that this feature is the more prominent feature that is calculated to exist at the[54] X-point, we will turn to simulation in the next chapter to compensate for fall-off of field strength away from the plasma surface and the effect of eddy currents driven near the sensors by the rotating mode.

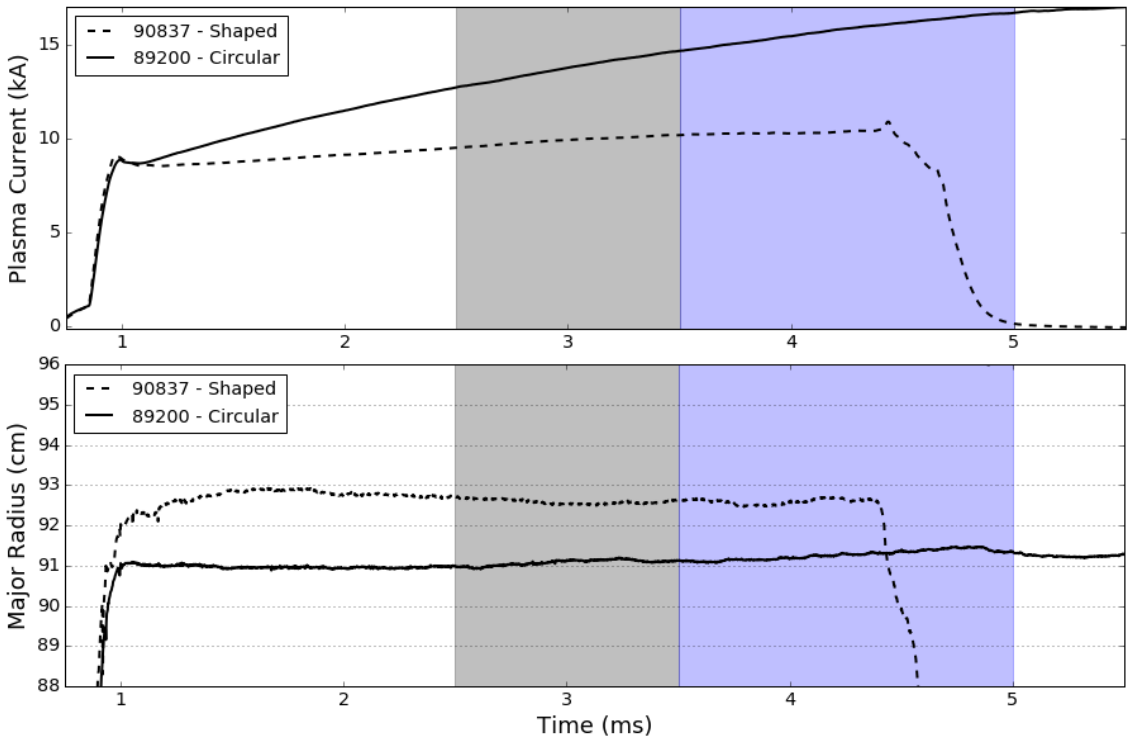

Figure 5.10: Circular shot 89200 and shaped shot 90837, predicted to have similar edqe q. Shot 89200 is fully 15cm in minor radius, but at the inboard limit of the range in the chamber where such large minor radii are possible. Time regions for the BD analysis are different in the two plasmas. 2.5-3.5ms for 90837(grey shading), as before, but 3.5-5ms for shot 89200(blue shading)

5.4 Disruptions in Shaped and Circular Equilibria

It has been found to be the case that stable shaped plasma equilibria are more difficult to develop and generate than stable circular equilibria, in agreement with the experience of other limited experiments that transitioned to diverted operation[85]. HBT-EP plasmas generally show significant shot-to-shot variation, and this variation increases with the imposition of shaping. The percentage of acceptable shaped shots in a given run day, defined as those that persist for at least 2.5 ms after full imposition of shaping without minor or major disruption and with steady major radius, will be much less than the number of unshaped plasmas that satisfy those criteria.

5.4.1 Shaped Plasma Lifetime

Shaped plasmas tend to disrupt earlier than circular plasmas that exhibit similar MHD modes. While unshaped plasmas with $m = -3$, $n = 1$ mode activity can persist for 6-7ms, similar shaped

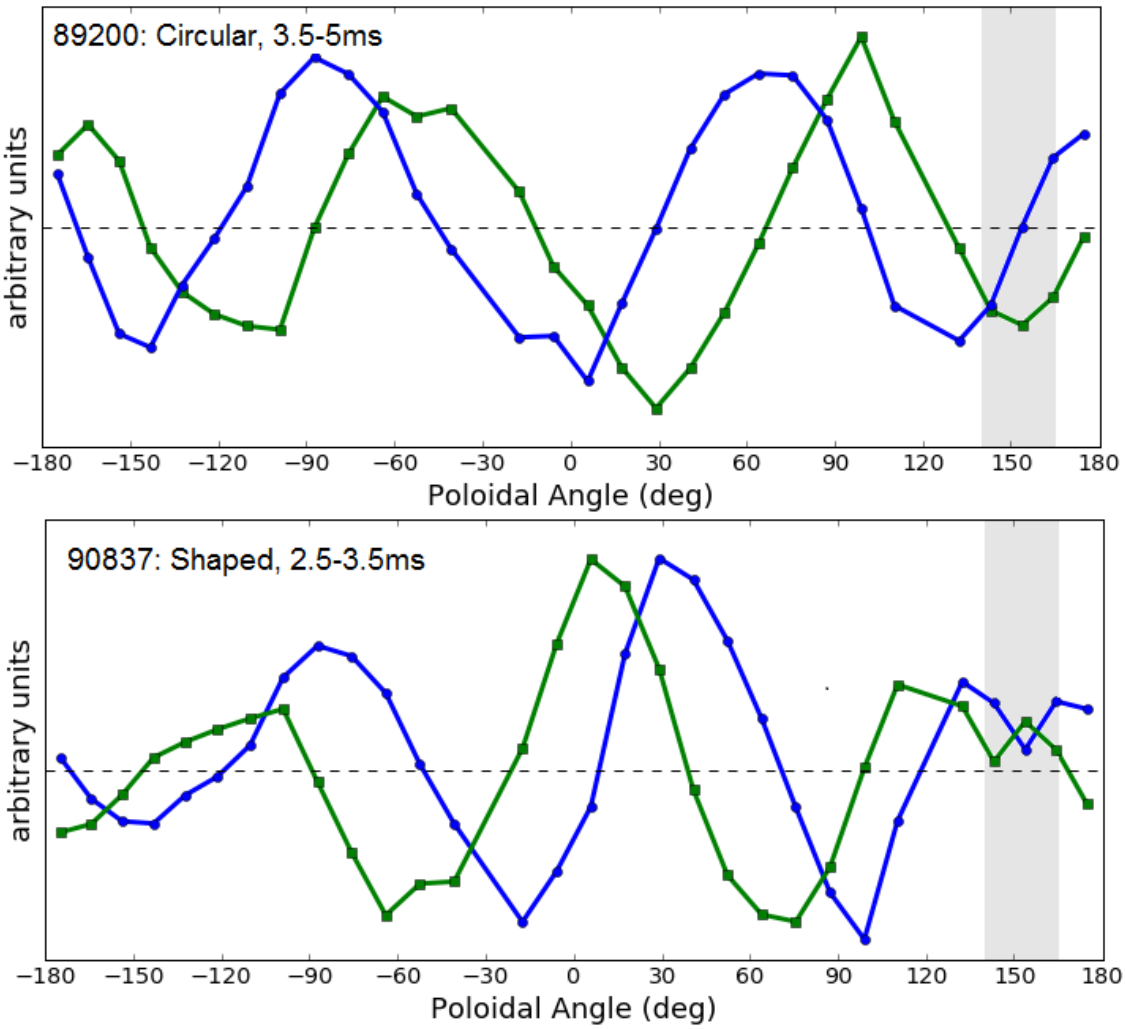

Figure 5.11: The dominant $m = -3$ mode pair extracted from unshaped shot 89200, compared with the dominant $m = -3$ mode pair extracted from shaped shot 90837. Due to its inboard location, coupling to the sensors is roughly constant poloidally for shot 89200, despite the amplification of poloidal fields from the stabilizing shells, and the natural tendency of the external kink to have larger amplitude outboard. No X-point localized feature is seen in the circular plasma mode.

plasmas tend to disrupt within 3ms of the imposition of shaping. The reasons for this are not well understood, but the method by which the plasma equilibrium development is determined on HBT-EP presents a strong constraint on our ability to develop shaped equilibria.

All vacuum field coils are powered by multi-stage capacitor banks, as discussed in Chapter 2. The start phases all involve very rapid impositions of their fields to a set start-point, and the crowbar banks determine the slower evolution that those fields will follow from those points. In the case of a circular equilibrium this is sufficient, but in shaped plasmas, after the start banks have discharged

and the crowbar banks have begun to conduct, the equilibrium is put through a dramatic and rapid development. The degrees of freedom allowed by the capacitive banks which power the vacuum field coils are limited in the first place, and are exhausted before the plasma is shaped. Bank presets must be selected that satisfy the creation of a stable circular plasma equilibrium that can then survive the imposition of shaping and persist for a useable time as a shaped equilibrium, and the difficulty of reconciling those demands to the degree of control we can exert is a potential limit on the performance of shaped plasmas.

5.4.2 Speed of Disruptions

Disruptions on HBT-EP are characterized by the following pattern. First rapid loss of thermal energy leads the plasma to collapse under the force of the vertical field acting on the plasma current. As this thermal quench occurs, the plasma moves rapidly inwards. This leads to an inductively driven spike in plasma current of several percent on the timescale of the collapse. As the plasma becomes cooler and more resistive, the plasma current decays and the plasma continues to fall inwards. Figure 5.1 illustrates this, as well as the short lifetime of a shaped plasma and the rapidity with which the disruption occurs compared to circular plasmas. The current spike is a distinctive and reliable feature of disruptions for both plasma geometries, and will be used as a reference point throughout this analysis. A 20 shot set is analyzed, with 10 shaped and 10 unshaped shots in order to get a sense of the averages and variances in how each type of plasma disrupts.

The external kink that exists before disruption in both plasmas are observed to grow rapidly in amplitude just before the plasma current spike that follows the initial major radial collapse and signals the beginning of the current quench. It is at this point that the behavior of shaped and circular plasmas diverge. Figure 5.12 shows the subtracted signal of two toroidal array sensors located opposite each other in the chamber for a collection of shaped and circular shots. Subtracting signals from sensors toroidally 180° out of phase from one another leaves n = odd Fourier components of the signal. As the mode spectrum is dominated by lower n modes, as seen in Figure 5.6, $n = 1$ signal is expected to dominate over $n = 3$ and higher modes so it is assumed the n= odd signal is primarily $n = 1$.

The shaped plasma signal rapidly grows to a level of $\sim$ 25G and remains at that level until the plasma discharge terminates, while speeding up to a rotation frequency of 20kHz. The time to termination of the discharge after the current spike in a shaped plasma is generally 0.25ms -

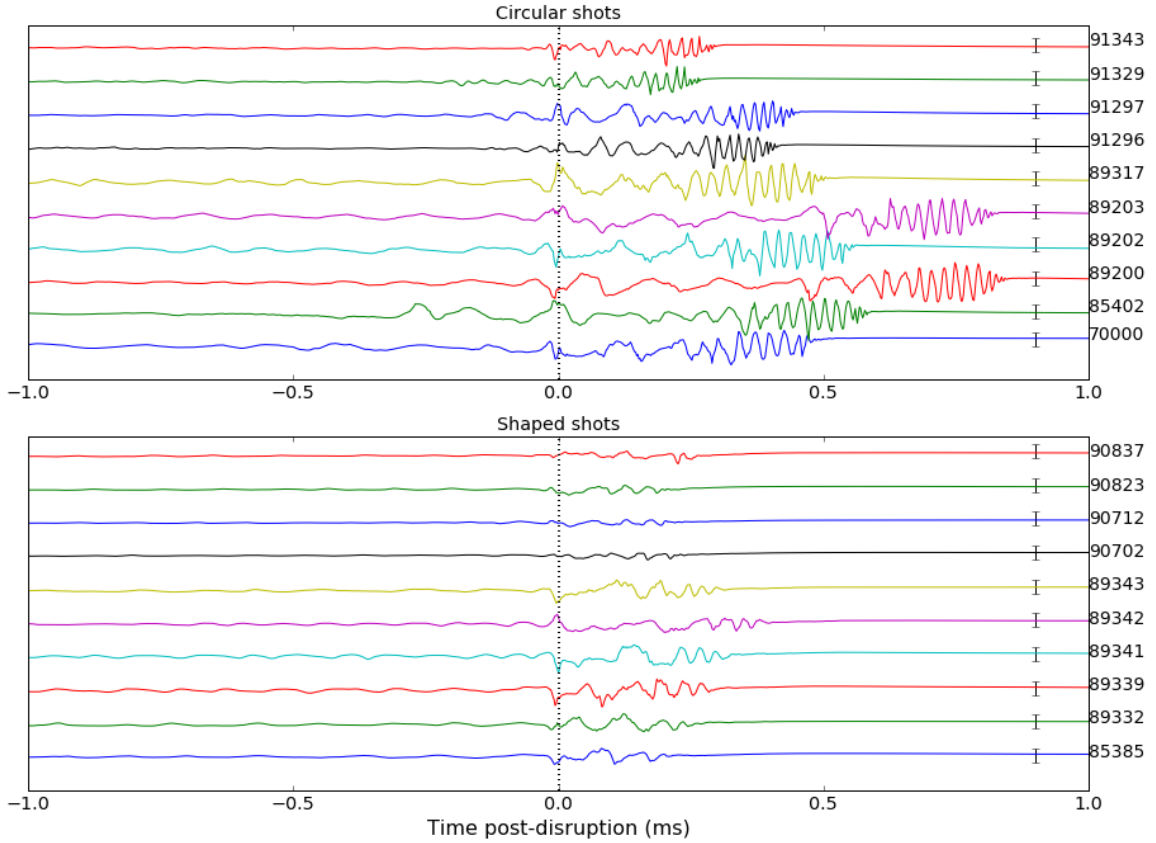

Figure 5.12: $n = 1$ subtraction of Toroidal Array sensor signal on either side of the disruption for a set of shaped and circular shots. Brackets to the right of each trace represent ±25G. Both plots are to the same scale.

0.3ms. In circular plasmas, the disruption occurs in two stages. Just after the current spike, without changing frequency, the mode amplitude grows to a value roughly equal to that of a shaped plasma post-disruption. This phase persists for longer than in shaped plasmas, in some cases over 0.5ms, before giving way to the second stage of the disruption. The second phase begins as the plasma has fallen far inboard, and involves the n = odd signal growing to very large amplitude, over 50G in some cases. The mode rotates more quickly, at about 40kHz, for 0.25ms-0.3ms before rapidly declining in amplitude as the discharge terminates. Two representative shots from the ensemble are shown in greater detail in Figure 5.13.

Circular shots 85402, 91296, 91297, 91329 and 91343 have lower plasma current at disruption versus the rest of the circular data set. Pre-disruption, the fluctuations are generally lower in amplitude, but the freqeuency increase is seen. Shaped shots 90702, 90712, 90823, 90837 have

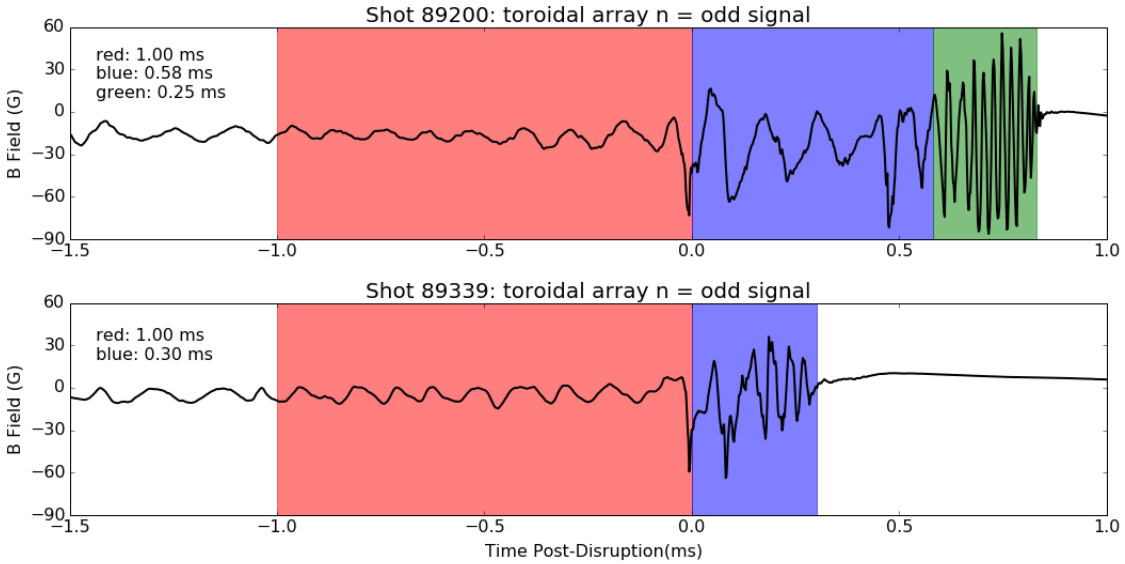

Figure 5.13: n = odd subtraction of toroidal array sensor signal for a representative shaped and circular plasma. Differences in mode amplitude are minor until the circular plasma begins the second phase of the disruption. The frequency of the mode in the shaped plasma disruption is larger than that of the mode during a circular plasma disruption's first stage, and slower than that of the second.

lower current at disruption and we see that fluctuations are smaller in amplitude as well but do not accelerate during their disruptions.

5.5 Summary

External kinks in a diverted plasma equilibrium are compared to those in two different circular equilibria. One circular plasma has similar major radius and plasma current, while the other has a similar edge q. The methodology of equilibrium subtraction was described, showing how mode structure can be isolated from raw fluctuations. A small-amplitude, short-wavelength fluctuation near the X-point in a shaped plasma was observed, which was not present in either circular plasma. This is a feature of the structure of the external kink in diverted plasmas that has been calculated to exist[33, 54], and our measurements are consistent with those calculations while building upon measurements made using soft X-ray tomography of diverted plasma mode structure that did not include the outer edge region of the plasma[54]. It is worth noting that these measurements of the highly resistive HBT-EP equilibria are consistent with the model of a resistive external kink in Huysman's 2005 paper, rather than the peeling ballooning mode predicted to arise in diverted,

resistive plasmas. The amplitude of the modes were seen to vary with poloidal angle, and this variation is a function of plasma major radius. Background signal due to subdominant modes and residual equilibrium signal are removed by using the biorthogonal decomposition. The structure of the mode isolated by the BD is similar in all cases to those seen in the raw fluctuations, in particular the X-point localized fine structure near the X-point in the diverted discharge.

This represents the first observation of the structure of an external kink in a diverted plasma in the divertor region using magnetic diagnostics that could be found in the literature. HBT-EP is uniquely situated to further explore X-point localized MHD activity and to magnetically probe the divertor region. The disruptions in shaped and circular plasmas were compared. It is seen that shaped plasmas disrupt earlier and more rapidly than circular plasmas. The MHD disruption precursors and behavior immediately following disruption are similar in amplitude and frequency, though the circular plasmas display a distinct phase of disruption not shared by shaped plasmas, in which the mode increases in frequency and amplitude for the final 0.25ms of the discharge termination.

Chapter 6

Kink Mode Simulation in Shaped and Circular Plasmas

Equilibria reconstructed from measurements of both shaped and unshaped plasmas are input to the ideal MHD code DCON[22, 23] to calculate the structure of external kink modes in HBT-EP. The calculated structure of the kink is then compared to the measured structure of kinks. Similarities are found, such as number of peaks and the prediction of fine structure near the X-point, but disagreement is also found, particularly in the location and amplitude of peaks. The VALEN code[27] is used to estimate the measured magnetic field at the sensors from the DCON calculated mode structure. The effect of separation between sensors and plasma as well as the effect of eddy currents induced by mode rotation on sensor measurements are calculated by VALEN. Very good agreement is found, and these calculations of expected signal illustrate a computational technique that can be applied to other fusion devices with rotating kink modes.

This chapter is organized into four parts. Ideal, no-wall calculations of the structure of the eigenmodes for various diverted and circular equilibria are calculated using the code DCON. The similarities and differences between the computed mode structure and the structure of the modes measured in Chapter 5 are discussed, as well as the potential causes for the disagreements, including plasma-sensor separation and eddy currents driven by mode rotation. These effects are accounted for using the code VALEN, which models the plasma surface currents and nearby conducting structures as an electromagnetically coupled system of finite elements. After accounting for sensor position

and eddy currents, the computed mode structure at the location of the sensors is compared to the structure of the modes as measured and found to agree.

6.1 Ideal No-Wall Calculations: DCON

DCON[22, 23] is an ideal MHD stability code that takes a computed plasma equilibrium and determines the shape and stability of the kink eigenmodes throughout the plasma cross section. Comparing the DCON calculations for the stability and structure of the kink modes at the Ψ_{99} surface to the empirically measured edge-localized kink modes establishes the degree of understanding of the observed instabilities and helps to identify the modes.

Figure 6.1 shows the DCON computed mode structure for the three equilibria under consideration. The circular equilibria were analyzed just as the edge safety factor passed below a resonant value, $q_* \leq 4$ in shot 91329, and $q_* \leq 3$ in shot 89200. The diverted equilibrium was analyzed at a time well removed from both the turn-on phase of the shaping coil (concluding at 2ms), and the disruption of the plasma, to allow clean separation of the mode information from magnetic measurements.

DCON computes a mode structure for the circular equilibria that corresponds to the safety factor at the plasma edge. The structure of the mode in the shaped shot is dominantly $m = -3$, $n = 1$, with a low-amplitude, short wavelength feature near the X-point. Recall, the direction of the plasma current with respect to our toroidal field, and the conventions by which we define toroidal and poloidal angle lead to a left-handed helicity on HBT-EP, and negative m-numbers for the observed modes.

This low-amplitude, short-wavelength, X-point localized feature is similar to the feature calculated to exist on other diverted experiments[33, 54]. The poloidal array sensors detected a similar feature near the X-point, and in the observations of mode structure discussed in Chapter 5, it is located at roughly the same poloidal angle as the feature as calculated by DCON.

6.2 Plasma-Sensor Coupling

DCON provides a sine/cosine like pair of modes for every eigenvalue. These modes are overlaid on the TokaMac predicted LCFS for each of the three equilibria under consideration in Figure 6.2. Each

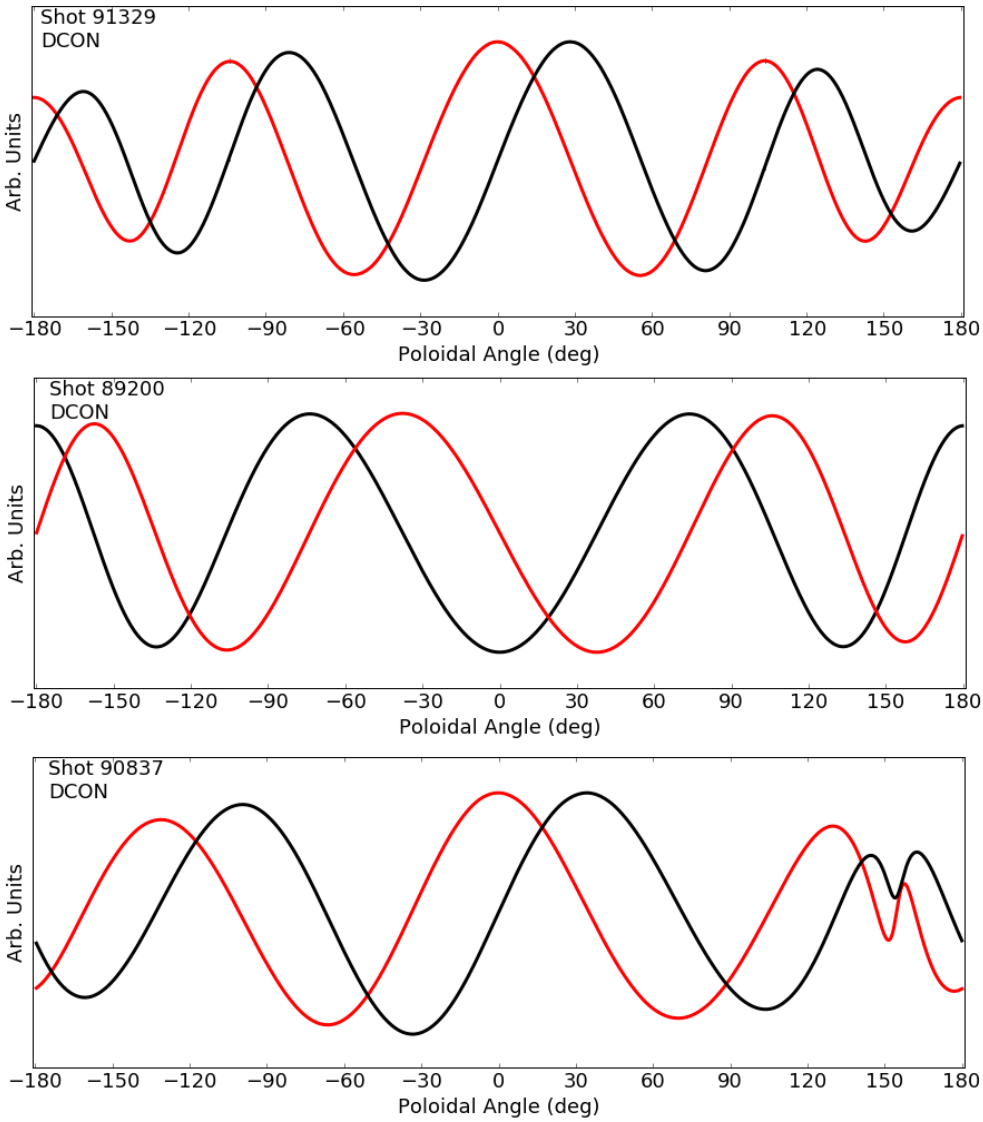

Figure 6.1:
Top: DCON predicted dominant mode pair structure of circular shot 91329, at 3ms. Note the poloidal amplitude variation. Middle: DCON predicted dominant mode pair structure of circular shot 89200, at 3ms. Amplitude is nearly constant along the plasma perimeter. Bottom: DCON predicted dominant mode pair structure of shaped shot 90837, at 3ms. Note the slight amplitude variation and fine structure near the X-point (150°).

poloidal array sensor's separation from the plasma edge is different, with the largest sensor-to-sensor variation in the case of the shaped plasma. The m-spectrum of fields generated by helical surface currents on a plasma with minor radius a will be distorted as the amplitude of each component decays with distance r roughly as[86] $B(r) \propto (a/r)^{m+1}$. Even controlling for overall reduction in

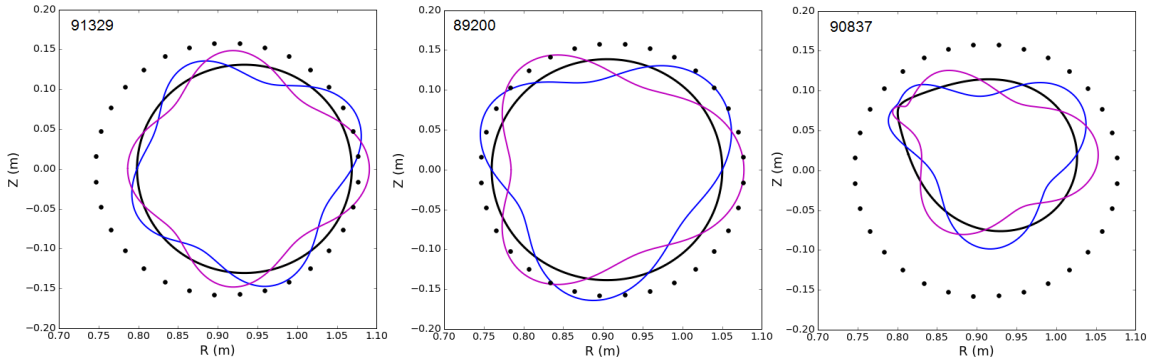

Figure 6.2: TokaMac predicted LCFS of the plasma in three equilibria, with the DCON predicted dominant external kink mode structure superimposed. Black circles represent the Poloidal Array sensors. The varying distance from the plasma to the mode will affect the measured amplitude of the mode, and in the case of the shaped plasma, the poloidal spectrum.

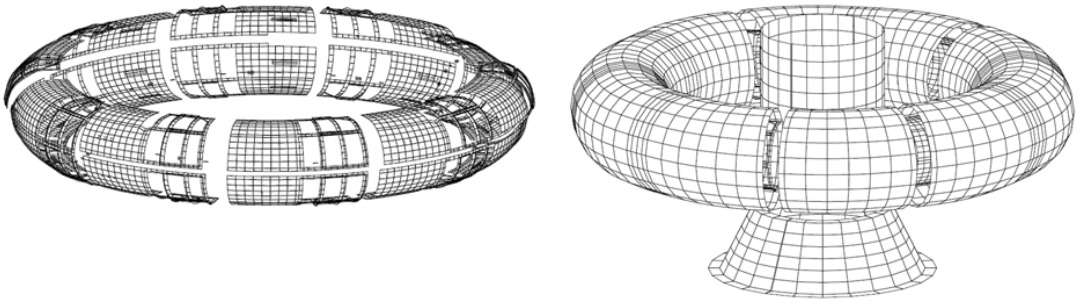

Figure 6.3: Two of the meshes used by VALEN to simulate eddy currents in external conductors. On the left, the in-vessel modular shells. On the right, the vacuum vessel segments, with insulating breaks, central cylinder, and base cone. Not shown; Plasma surface mesh, which is generated from TokaMac reconstructions and varies based on plasma position, minor radius and shaping.

signal strength with plasma-sensor distance, the measured structure of the mode at the wall will be different from that at the surface due to the unequal decay of Fourier components with distance. Finally, if the mode rotates, eddy currents are driven that will couple to the mode and distort the structure of the field in a way that is dependent on the geometry and electrical characteristics of the conducting structures.

6.3 Eddy Currents and Geometric Effects: VALEN

VALEN is a finite element code[27] that solves circuit equations for a mesh of conducting elements (see Figure 6.3) on which either the current through each element, the flux through a loop of elements, or both, is specified. The interaction between currents in multiple unconnected meshes

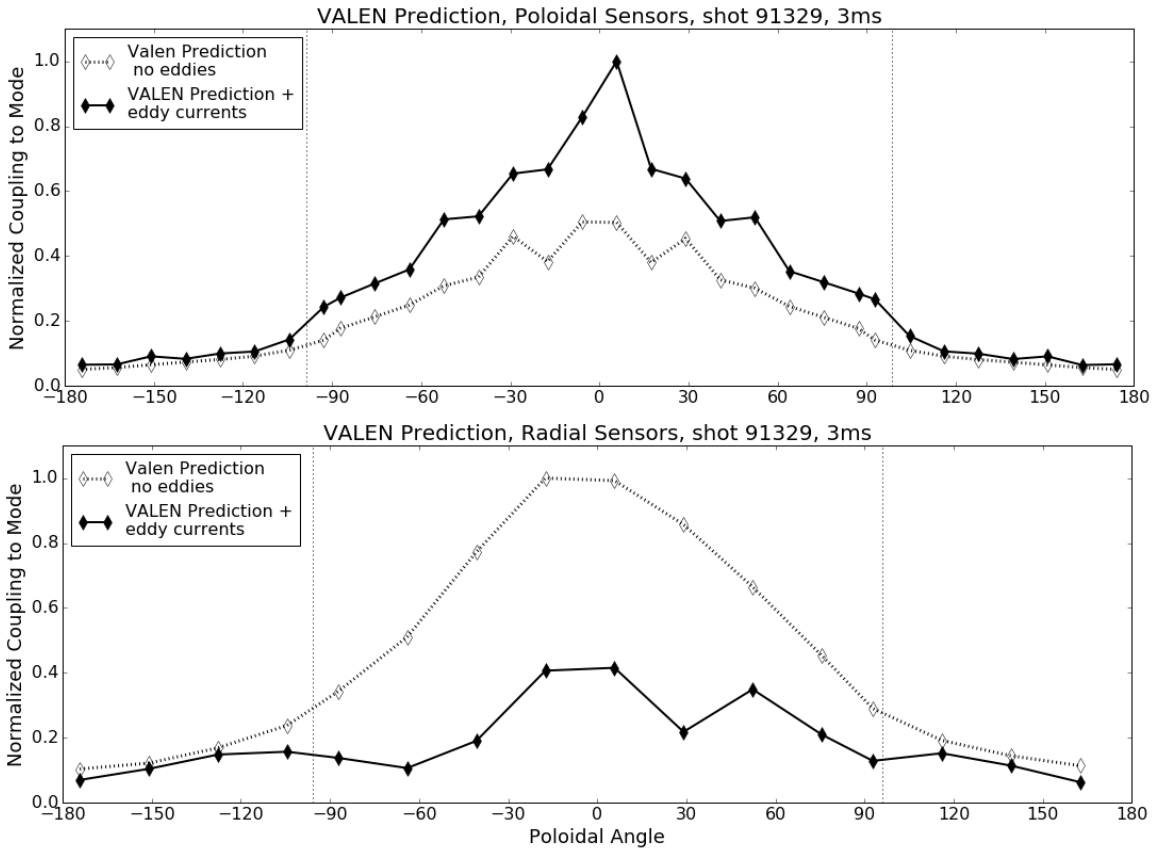

Figure 6.4: Relative strength of measured signal on the poloidal array sensors from the $m = -4$, $n = 1$ mode in circular shot 91329. Effects of mode rotation on degree of eddy current effect on poloidal and radial fields are shown. Shell locations are $-95^\circ \geq \theta \geq 95^\circ$. Top: VALEN calculation of the measured mode amplitude at the poloidal array B_p sensors with a non-rotating mode, and one rotating at 10kHz. Bottom: VALEN calculation of measured mode amplitude at the poloidal array B_r with a non-rotating mode and one rotating at 10kHz.

can be modeled, and for this research, meshes representing the plasma LCFS and the conducting structures including sensors, shells, vacuum vessel, and external field coils are used. Currents are specified on the surface of the plasma mesh to create a mode-resonant normal field[87] and phased at a given frequency to calculate the eddy response. A self-consistent solution is found for the structure of the plasma currents and conductor eddy currents, and the conducting structures' (sensors and control coils in particular) coupling to any non-equilibrium currents in the plasma/vessel system.

VALEN is able to account for the geometric effects of surface-sensor coupling, as well as the uneven decay of the m-spectrum of the perturbed field. It can also sum the sine and cosine components of a DCON calculated eigenmode with a time varying phasing to to determine magnetic interaction of the rotating kink with conducting structures. The coupling of sensors to plasma surface currents,

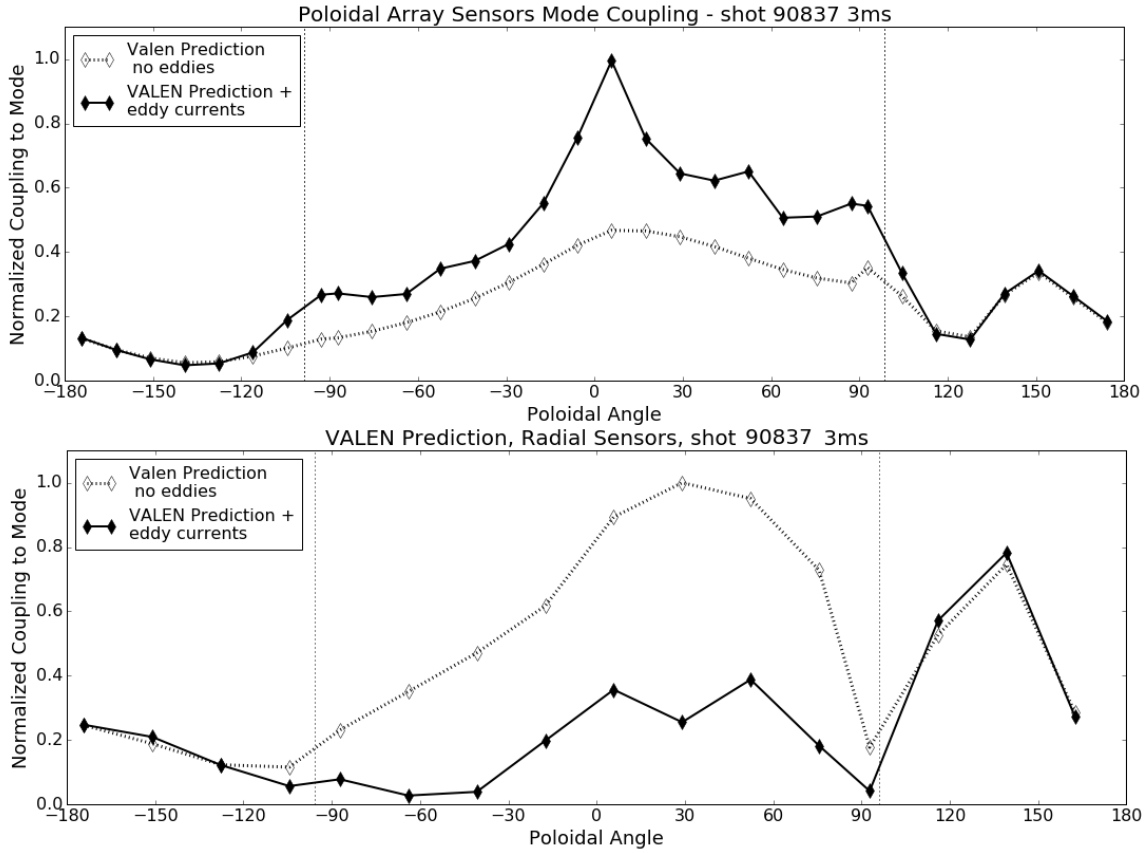

Figure 6.5: Relative strength of measured signal on the poloidal array sensors from the $m = -3$, $n = 1$ mode in shaped shot 90837. Effects of mode rotation on degree of eddy current effect on poloidal and radial fields are shown. Shell locations are $-95° \geq \theta \geq 95°$. Top: VALEN calculation of the measured mode amplitude at the poloidal array B_p sensors with a non-rotating mode, and one rotating at 10kHz. Bottom: VALEN calculation of measured mode amplitude at the poloidal array B_r with a non-rotating mode and one rotating at 10kHz. Note the asymmetry about the midplane, due to a calculated 1cm vertical offset in the plasma magnetic axis.

the decay of the full mode spectrum with distance, and the effect on sensor measurements of direct pickup of the eddy current fields are then accounted for.

The coupling of the dominant mode in circular shot 91329 to the poloidal array sensors as a function of rotation speed is plotted in Figure 6.4 and Figure 6.5 for shaped plasma shot 90837. Eddies driven by mode rotation in the close fitting shells are seen to affect the expected structure of the mode, increasing the amplitude of the poloidal field of the mode, and suppressing the amplitude of the radial field.

These modes, which were observed to rotate at $\sim$ 10kHz, are calculated to present an outboard ballooning as measured by B_p sensors on the shell due to the eddy currents, as well as their outboard

location, and indeed this was observed in Figure 5.8. Referring back to the surface fields on the DCON mode that provided the input for the VALEN frequency response calculations in Figure 6.1, we see such ballooning is not a feature of the mode on the plasma surface. These sensor-by-sensor predictions of coupling to the DCON predicted mode allows investigation of mode structure agreement between simulation and measurement.

Quantifying coupling of control and detection systems to modes of interest in the presence of conducting structures is a topic of active study[88], and measurements of sensor pickup of control fields applied at different frequencies in vacuum have been used[89] to benchmark VALEN models of conducting structures. In this research, that methodology is inverted, and we will use a detailed VALEN model of HBT-EP to calculate the coupling between control coils, plasma surface modes, magnetic sensors, and eddy currents in a self consistent way.

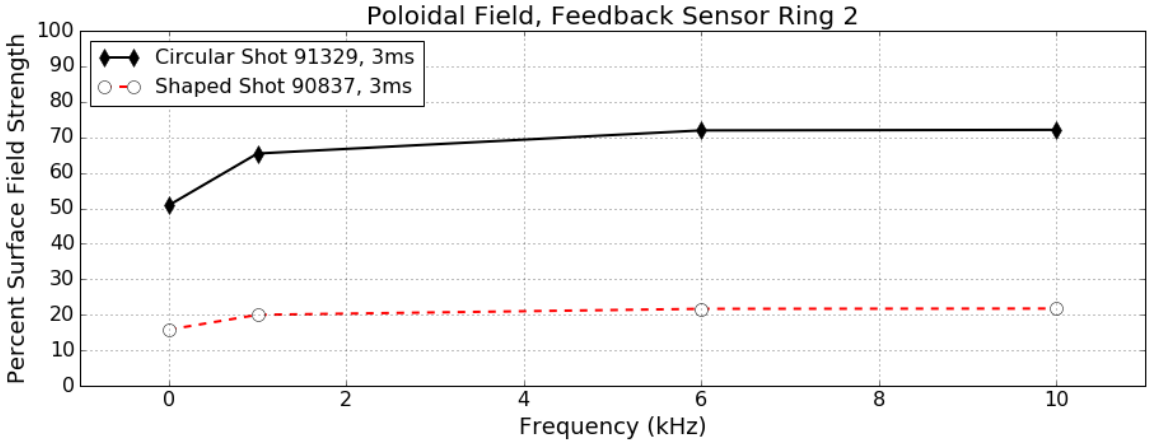

Figure 6.6: VALEN predictions for perturbed field amplitude of the lower midplane ring ($\theta = -29.3°$) of feedback array B_p sensors due to the dominant DCON mode for two different TokaMac equilibria. The field strength at the plasma surface is equal in both shots, demonstrating the effect of geometric coupling.

Cross Section	**0 Hz**	**1kHz**	**6kHz**	**10kHz**
Circular	0.51 G	0.65 G	0.72 G	0.72 G
Shaped	0.16 G	0.20 G	0.22 G	0.22 G

Table 6.1: DCON/VALEN predicted $n = 1$ field strength on the lower midplane ring ($\theta = -29.3°$) of feedback array B_p sensors due to 1 Gauss of perturbed normal field strength.

The ratio of the normal field strength of the DCON mode at the plasma surface to the VALEN calculated amplitude of the $n = 1$ poloidal field signal measured by the feedback sensor arrays is used to quantify the coupling between sensors and the kink mode normal field strength at the plasma

surface. These ratios are tabulated in Table 6.1, and displayed graphically in Figure 6.6. There can be significant falloff in amplitude of the field from plasma surface to sensors. As the plasma rotation increases, the poloidal field is amplified for those shell-mounted sensors.

6.4 Comparison of Measurement and Simulation

When the DCON prediction of mode structure, as in Figure 6.1, is given as input to a VALEN frequency response simulation using the measured mode rotation frequency, a set of predicted measurements of the mode is returned. This is illustrated in Figures 6.7, 6.8 and 6.9. The predictions are compared to measurement by appropriately phasing the BD mode pair into alignment with the VALEN prediction of measurement structure, shown in Figures 6.10, 6.11 and 6.12. By including VALEN estimates of mode-sensor coupling, the agreement between simulation and measurement is increased.

The poloidal shifts of the peaks are also accounted for, as well as the measured poloidal variation of the amplitude of the mode. Finally, we see that in the case of shaped plasmas, the predicted X-point localized fluctuation is reduced to an equivalent amplitude to the measured amplitude and is predicted to be measured at the location in which we observe it. Strong predictive ability through this simulation technique suggests good understanding of the kink mode structure.

The BD algorithm constructs a spatio-temporal basis set to describe the observed fluctuations with no reference made to the underlying physics of the MHD modes. There is thus no requirement that the BD selected basis match the MHD mode basis computed by DCON. The agreement between the BD isolated mode and the DCON/VALEN calculation demonstrates the algorithm returns eigenmodes of the measured field that are representative of the physical eigenmodes of the system.

6.5 Summary

DCON calculations of the structure of the ideal MHD kink modes for three equilibria are compared to the measured structure. The calculated modes are similar to the modes observed in the plasmas from which the equilibria are reconstructed. However, in some cases the amplitudes and locations of the peaks of the modes are measured to vary with poloidal angle in a way that is not in agreement with DCON calculations, due to sensor separation, and eddy currents generated by and coupled to

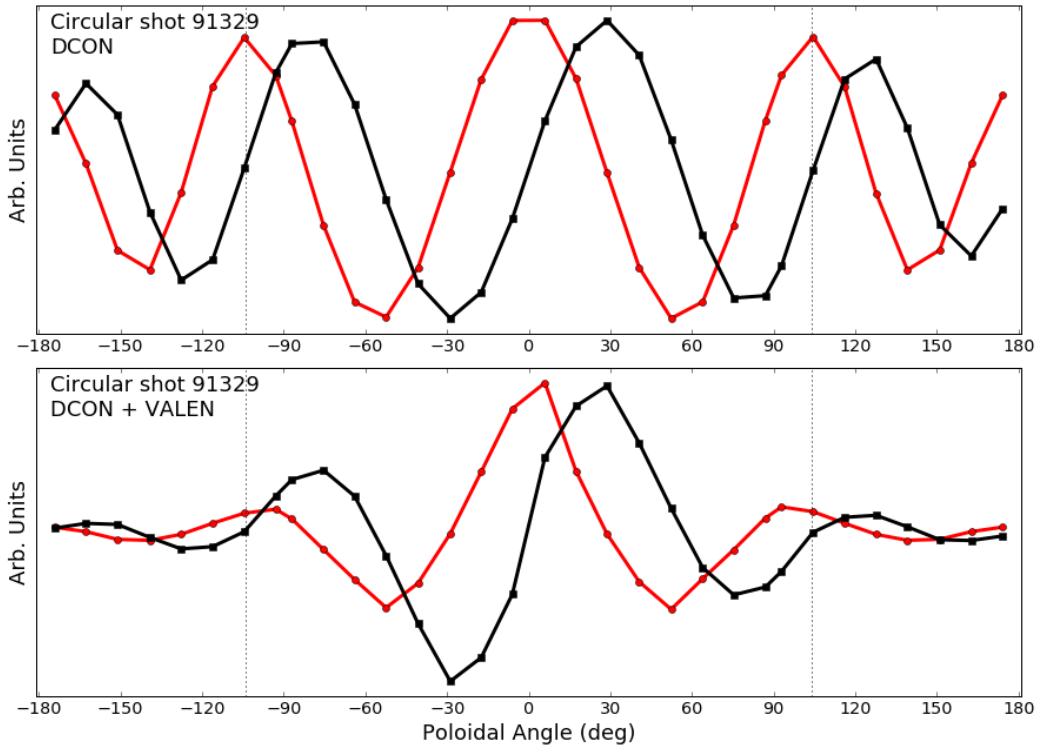

Figure 6.7: DCON prediciton for shot 91329 sampled only at the locations of the Poloidal Array sensors (red circles and black squares), and the VALEN prediction for the measurement of that mode. Strong poloidal variation of mode amplitude is predicted. Note the shifts in the poloidal locations of the peaks relative to the dotted lines.

the rotation of the mode. VALEN is used to account for the effect of plasma/sensor distance and mode rotation-coupled eddy currents driven in conductors near the sensors. The computed field at each sensor, after including these effects, agrees well with measurements. This method accounts for the location of HBT-EP's sensor set relative to the plasma surface as well as eddy currents driven in conducting structures. This method can be generalized to any fusion device, allowing verification of the predictions of MHD theory with an arbitrary set of sensors, in the vicinity of arbitrary wall currents.

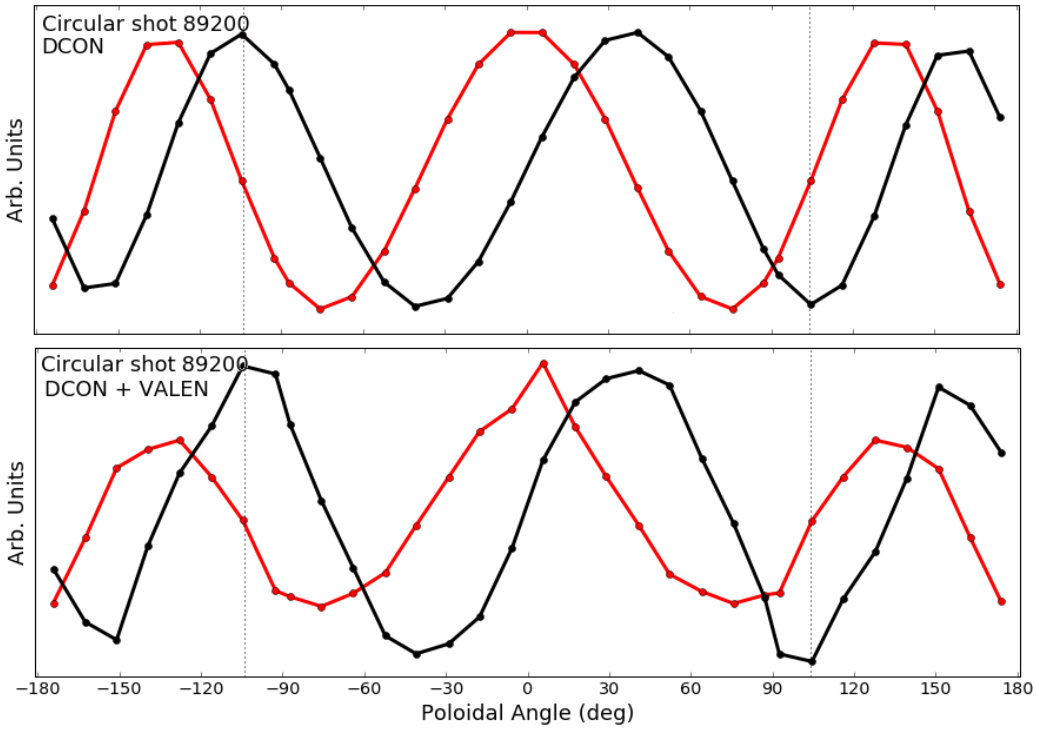

Figure 6.8: DCON prediciton for shot 89200 sampled only at the locations of the Poloidal Array sensors (red circles and black squares), and the VALEN prediction for the measurement of that mode. Amplitude and peak locations are not predicted to significantly change.

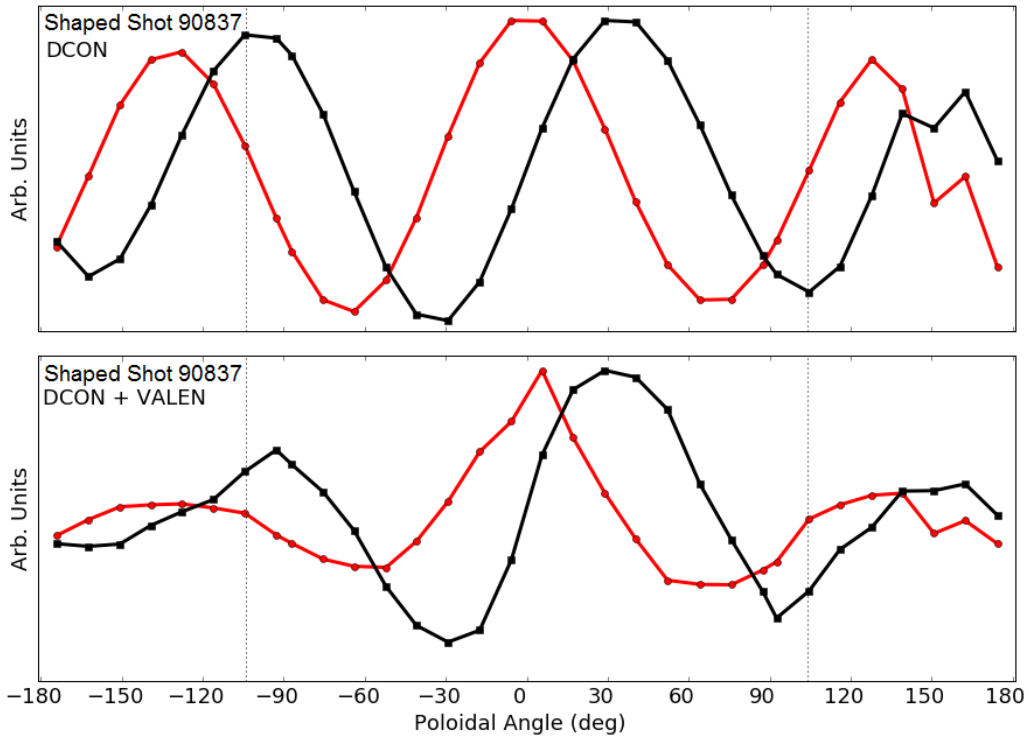

Figure 6.9: DCON prediciton for shot 90837 sampled only at the locations of the Poloidal Array sensors (red circles and black squares), and the VALEN prediction for the measurement of that mode. Note amplitude variation, downsampling and suppression of the X-point structure, and the shifts in the poloidal locations of the peaks relative to the dotted lines.

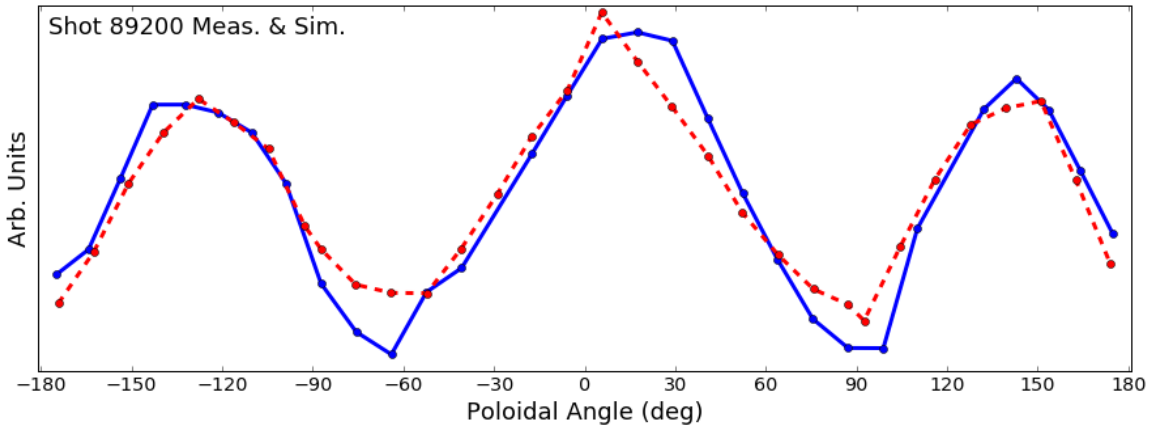

Figure 6.10: The dominant BD mode, solid blue line, compared to the DCON + VALEN calculation of the mode structure, dashed red line, for shaped shot number 89200,each appropriately phased.

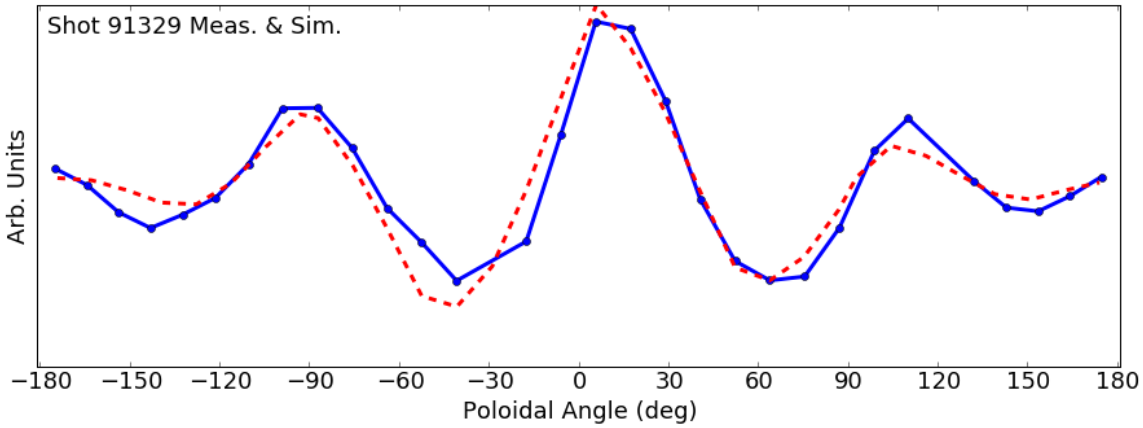

Figure 6.11: The dominant BD mode, solid blue line, compared to the DCON + VALEN calculation of the mode structure, dashed red line, for unshaped shot number 91329, each appropriately phased.

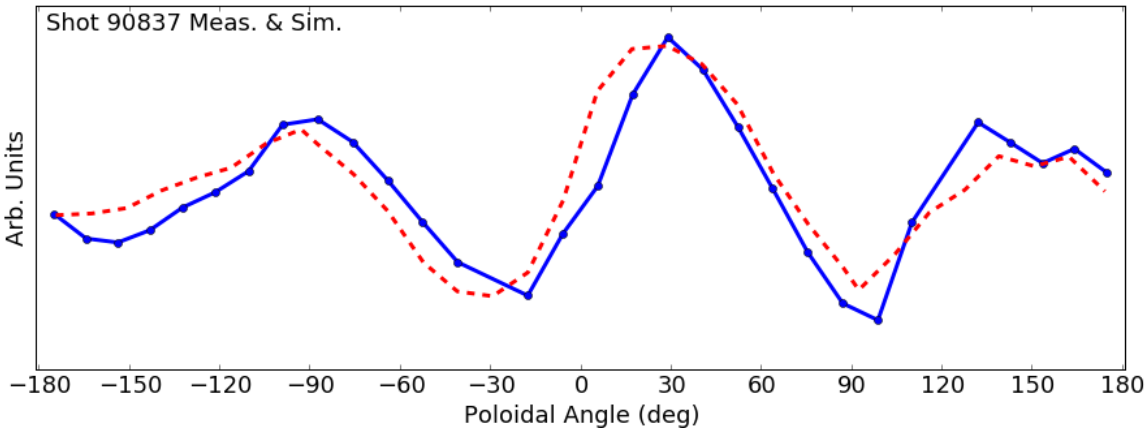

Figure 6.12: The dominant BD mode, solid blue line, compared to the DCON + VALEN calculation of the mode structure, dashed red line, for shaped shot number 90837,each appropriately phased.

Chapter 7

Excitation of MHD Modes in Shaped Plasmas

In addition to observing MHD kink instabilities, we can directly interact with them by applying 3D magnetic perturbations using our control coils. Circular and shaped plasmas are subjected to phase-flip[43, 44] resonant magnetic perturbations (RMPs). The plasma response is quantified as the ratio of measured response field and applied control coil currents[42, 86]. Differing plasma coupling to sensors is resolved through the use of VALEN, though the characteristic frequency of the perturbations, and the influence of eddies, is less.

7.1 Resonant Magnetic Perturbations

As described in Chapter 2.5.2, the control coils are arranged in a 4x10 grid around the outboard surface of the plasma. Each coil is independently operable, with open-loop or closed-loop control of the coil possible. The waveform applied to the control coil set is as described in Eq. 2.2, with the time-dependent amplitude $A(t)$ taking the form of a single pulse of a square wave. The period of the square wave is 1ms and the maximum current that can be driven through the coils is 40A, which establishes the maximum waveform amplitude. The positive/negative flip is performed to provide greater contrast against the background equilibrium signal.

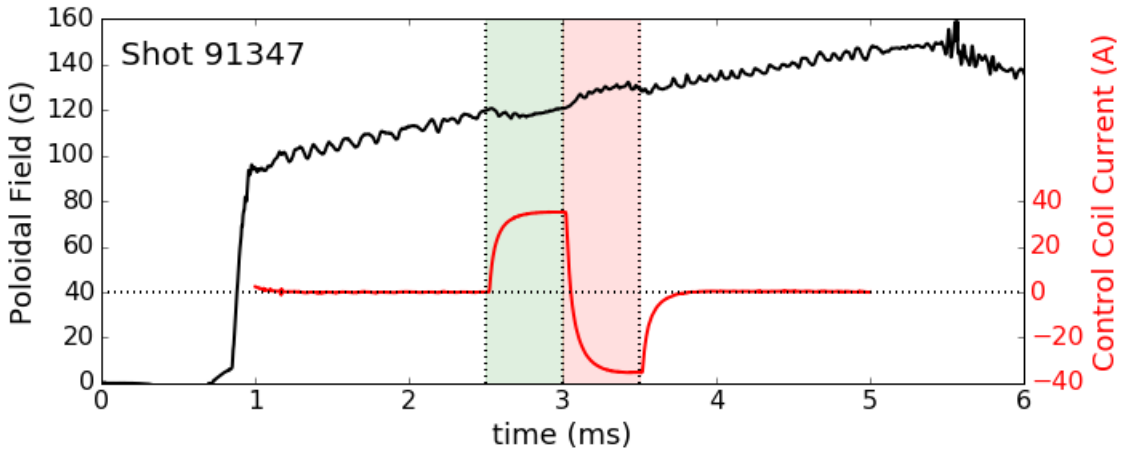

Figure 7.1: Signal on a poloidal array sensor during circular shot 91347, during which the plasma is subjected to an RMP. Overplotted is the current in a representative control coil. The influence of the RMP is clearly visible.

7.2 Equilibrium Subtraction

Figure 7.1 shows that the RMP waveform applied to the control coils. It is a single oscillation of a square wave, with a period of 1ms. The response of the control coil current to demand is limited by the 60 μs inductive response time of the control coils. The applied current reaches $\geq$90% of its peak value within 250μs. The principal frequency component of this pulse is 1kHz, slow enough for the response signal to be included in a polynomial fit to the equilibrium signal over the lifetime of a diverted equilibria. The polynomial is therefore fit to a time window that is non-contiguous, and excludes time periods during which the plasma equilibrium is responding to a perturbation. This is shown in Figure 7.2, and Shiraki et. al.[43] describe the procedure in greater detail.

7.3 Quantification of Plasma Response

The response C_i of the MHD mode is calculated in the same manner as previous work[42, 43] from the measured signal B_i in each sensor i during the time the RMP is imposed, T, and the amplitude of the current waveform $I(t)$:

$$C_i = \frac{\int I(t) B_i(t) dt}{\sqrt{T \int I(t) I(t) dt}} \tag{7.1}$$

The isolated fluctuations of a circular and a shaped plasma in the presence of an RMP is shown in

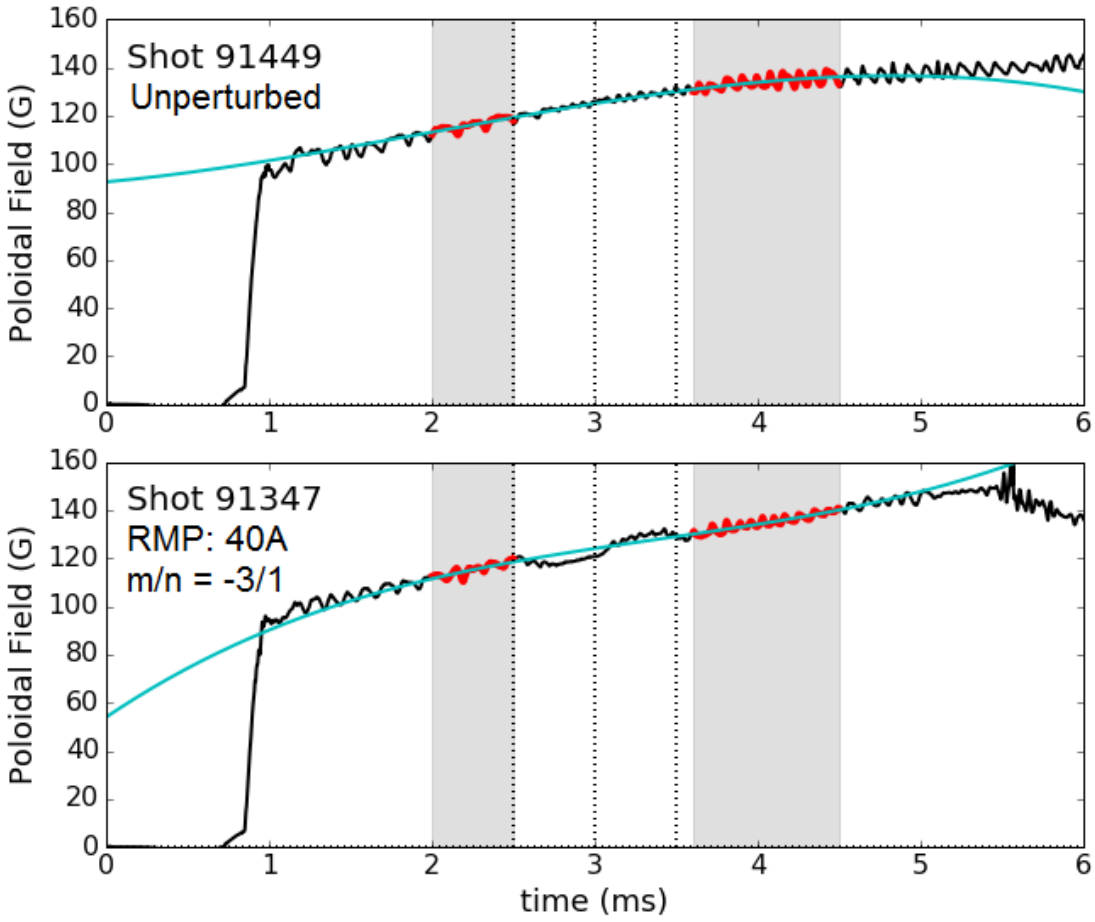

Figure 7.2: Fits to an unperturbed and a perturbed circular equilibrium. The periods used to fit to the equilibrium are bolded in red, and shaded. The on/flip/off changes in control coil currents are marked by dashed lines. The deviation from the fit is clearly correlated in time with the RMP, and the flip allows added contrast with which to observe the effect. Note that it requires a few tens of microseconds for the plasma to fully respond and transition to each new phase of the perturbation, and so the fit excludes a 20μs period after the end of the perturbation.

Figure 7.3. There is clear lag between control coil current and plasma response, the effects of which are reduced by calculating the integrals in Eq 7.1 over two disconnected time intervals. By ignoring a 0.25ms interval following the initial imposition of the perturbation and following the phase flip we consider only periods in which the coil current and plasma response have reached a steady state. The regions in which the correlation is calculated are shaded in the figure. The response measured by every sensor can be correlated to a single control coil current $I(t)$ as all coils have the same temporal waveform $A(t)$.

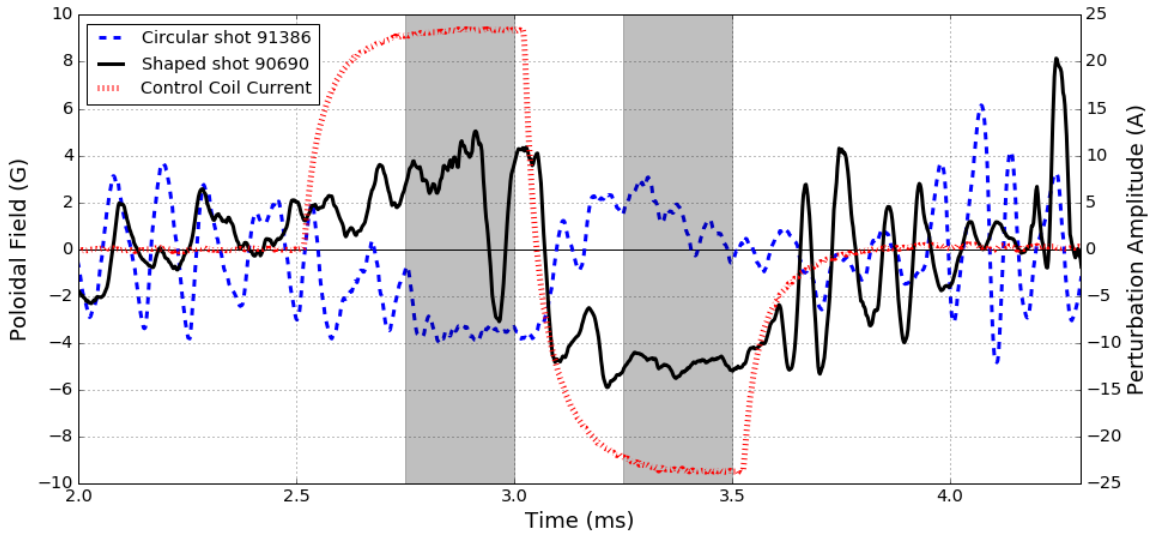

Figure 7.3: Magnetic fluctuations excited by the same perturbation for both shaped and circular plasmas, measured on a feedback array sensor, and current waveform amplitude $I(t)$. High-frequency rotating plasma-mode kinks will integrate to a small value when correlation is calculated.

7.4 Interpretation of Response

By calculating the correlations C_i for a grouping of sensors as in Eq. 7.1, we can infer the shape of the resonant response fields. The response as measured by the feedback sensors and poloidal array sensors is plotted for both shaped and circular plasmas with the BD structure of the dominant mode from a similar, unperturbed shot overplotted, in Figures 7.4, 7.5, 7.6, and 7.7. For the feedback sensor array, the BD mode pair is phased to agree with the feedback array sensor ring at $-89.4°$ (the lower, inboard, complete array) only. Good agreement is seen across the other 27 functioning sensors in the set in both cases, as well as across the poloidal array in both cases. The similarity in structure establishes that in both the shaped and the unshaped case, we are interacting with the already present, unstable MHD kink without distorting its structure, and the assumption that interaction with less resonant and/or more stable sidebands can be ignored[43] is appropriate. We can now quantify the degree to which the mode responds to a perturbation.

To establish a level of response, an $n = 1$ sine will be fit to the RMP response coefficients of the lower midplane ($\theta = -29.3°$) ring of feedback sensors, as this ring of sensors has good coupling to both equilibria. The method by which the response level is calculated is shown for a circular shot, number 91347 in Figure 7.8. The amplitude of the best-fit sine wave will be taken to be the response, in Gauss, of the plasma to the perturbation. The perturbation strength is quantified by

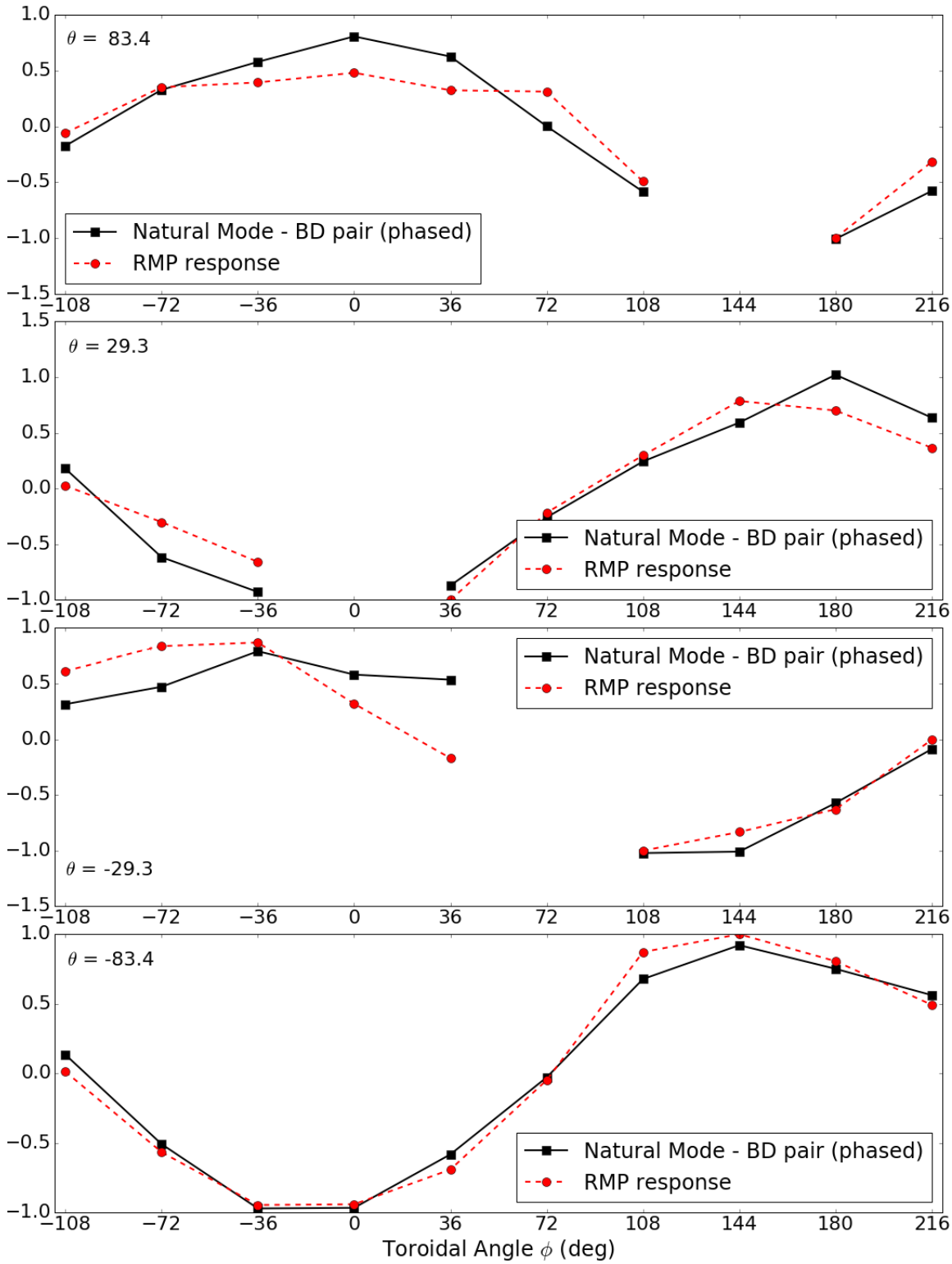

Figure 7.4: Natural and RMP driven MHD mode geometry for circular shots. 91329: Dominant BD topo (black, solid line, squares) for the 4 toroidal Feedback sensor arrays. 91347: RMP response (red, dashed, circles) for those same sensors. Topo mode pair is phased to agree with the RMP on the FB array 1 only. Good agreement is seen on the other three arrays. Traces are normalized on the Y-axis to allow comparison of structure. Gaps in the trace represent broken sensors.

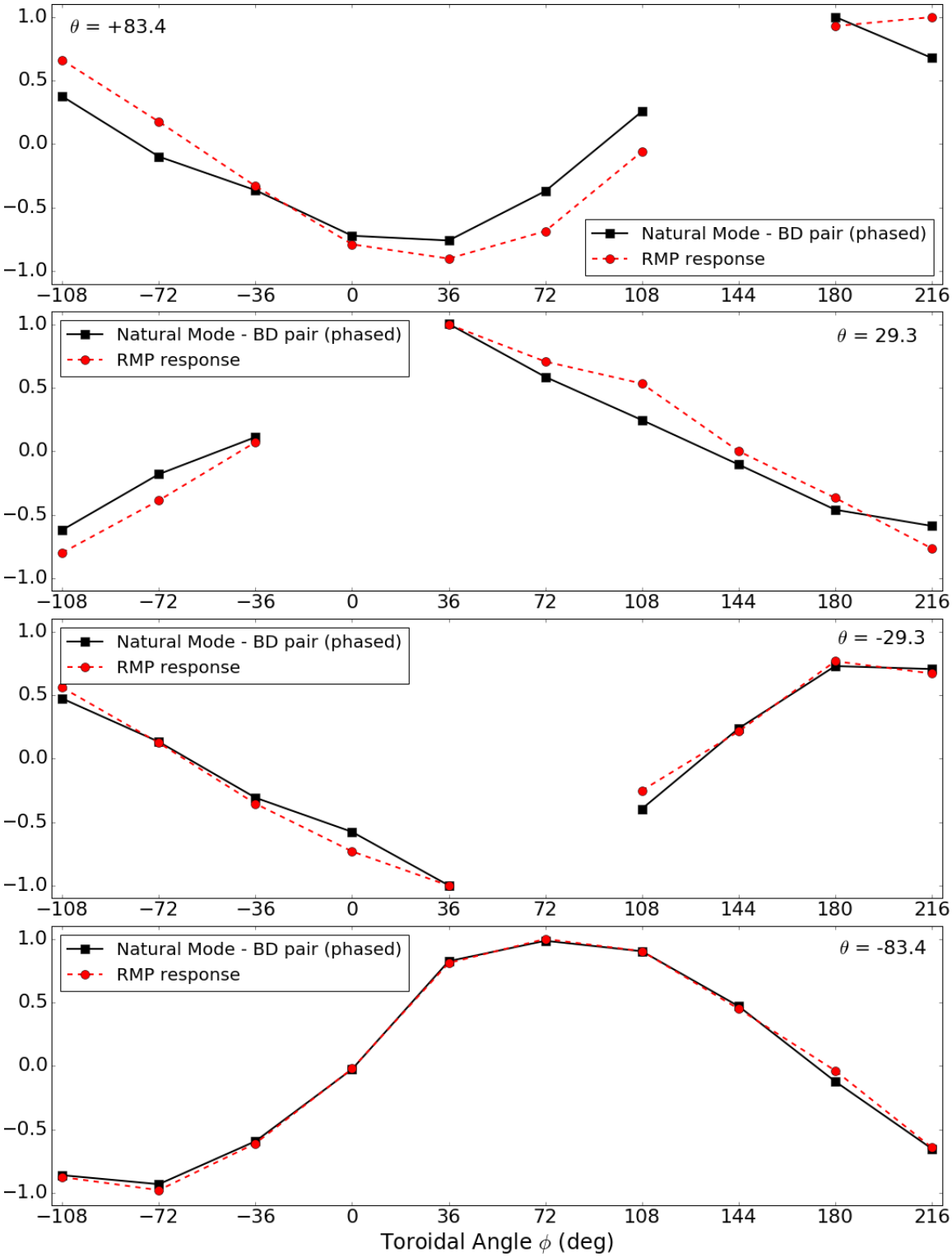

Figure 7.5: Natural and RMP driven MHD mode geometry for shaped shots. 90679: Dominant BD topo (black, solid line, squares) for the 4 toroidal Feedback sensor arrays. 90733: RMP response (red, dashed, circles) for those same sensors. Topo mode pair is phased to agree with the RMP on the FB array 1 only. Good agreement is seen on the other three arrays. Traces are normalized on the Y-axis to allow comparison of structure. Gaps in the trace represent broken sensors.

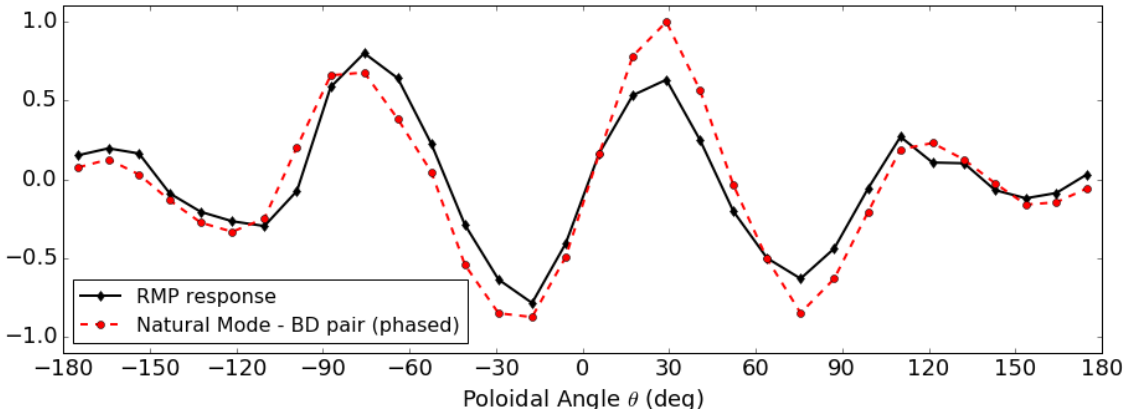

Figure 7.6: Natural and RMP driven MHD mode geometry for circular shots. 91329: Dominant BD topo (black, solid line, diamonds) for the Poloidal Array 1 sensors. 91347: RMP response (red, dashed, circles) for those same sensors. Topo mode pair is phased to agree with the RMP signal. Traces are normalized on the Y-axis to allow comparison of structure.

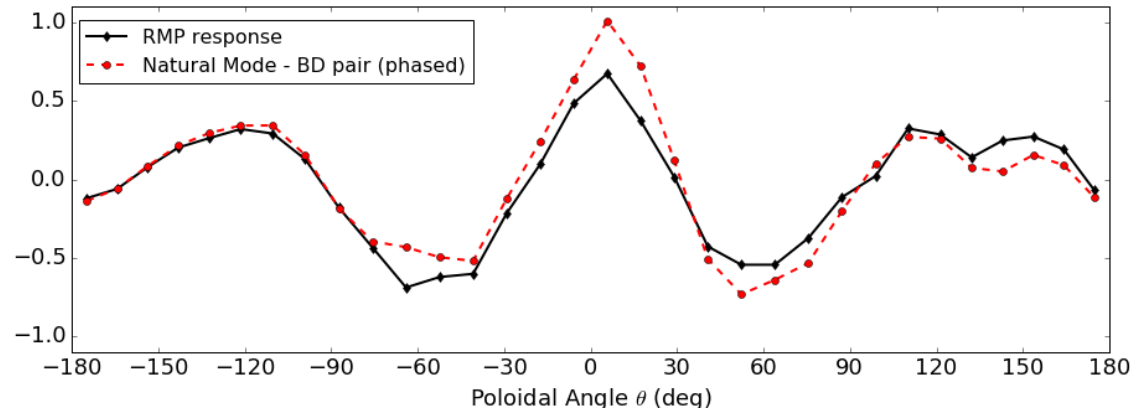

Figure 7.7: Natural and RMP driven MHD mode geometry for shaped shots. 90679: Dominant BD topo (black, solid line, diamonds) for the Poloidal Array 1 sensors. 90733: RMP response (red, dashed, circles) for those same sensors. Topo mode pair is phased to agree with the RMP signal. Traces are normalized on the Y-axis to allow comparison of structure. Note the presence of the short wavelength, X-point localized feature.

the amplitude of the current waveform in the control coils.

Figure 7.9 shows the response of the circular and shaped equilibria, as measured at the wall, and for a given amount of control coil current. The response is very similar between the two equilibria, and the response of both equilibria saturate after about 20A of control coil current is used to apply perturbations. The response of the shaped equilibrium is larger than the response of the circular equilibrium on the sensor ring at $\theta = 29.3°$, and both equilibria have the strongest coupling to the sensor ring at $\theta = -29.3°$. We should expect the circular coupling to be symmetric above and below

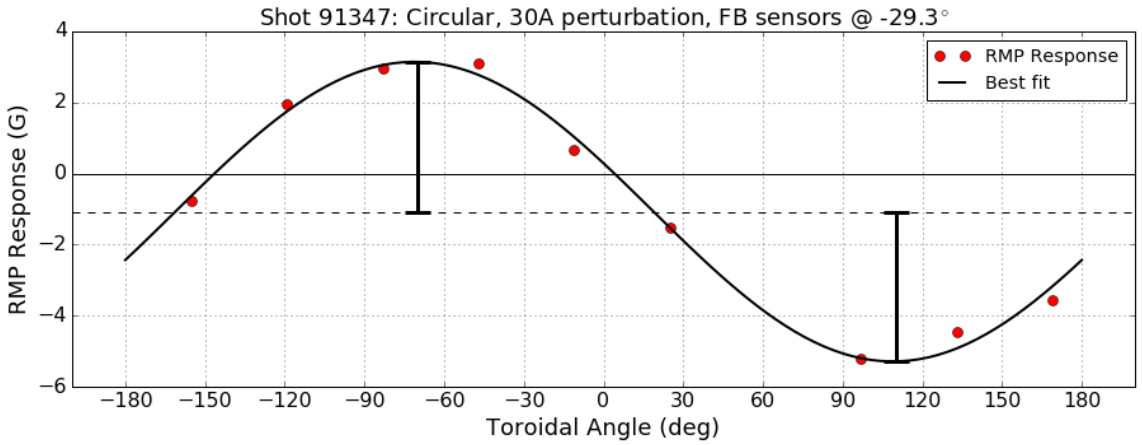

Figure 7.8: Correlation coefficients C_i, as determined using Eq. 7.1, for the $\theta = -29.3°$ ring of feedback array B_p sensors, for shot 91347. A curve of the form $y = a\sin(n\phi + \delta) + b$ is fit to the data. The solid line is the fit, the dashed line the DC offset b, and the bars the $n = 1$ amplitude a.

the midplane and the shaped coupling to be largest above the midplane, due to the vertical offset in equilibrium reconstructions of shaped plasmas. This is suggestive of a downward vertical offset in the position of both plasmas relative to the midplane of the chamber.

The edge safety factor of the circular plasma was ~ 3.5 during the $m = -3$, $n = 1$ perturbation, and both the measurements and modeling in Chapter 4 showed an $m = -4$ edge mode. Yet the response is roughly the same as that for the shaped plasma, which has an an m-spectrum heavily dominated by $m = -3$. An $m = -3$, $n = 1$ RMP weakly interacting with an $m = -4$, $n = 1$ mode is in keeping with previous results on HBT-EP[42, 59], but the similar level of response from a more resonant shaped plasma equilibrium motivates further analysis. The control coils and feedback array sensors used to calculate the response are closer and more conformal to the circular, high-m plasma, but these effects are not accounted for in our analysis. This ambiguity motivates exploration of the further use of DCON and VALEN to calculate the strength of the response at the plasma surface.

7.5 Summary

Two plasma equilibria, one circular and one shaped, were perturbed by phase-flip magnetic perturbations of varying strength. In order to calculate the plasma response to perturbation, the method used in previous work[43] to exclude the equilibrium signal measured by a sensor while still capturing the response to the perturbation was employed. The response is calculated from the post-subtraction

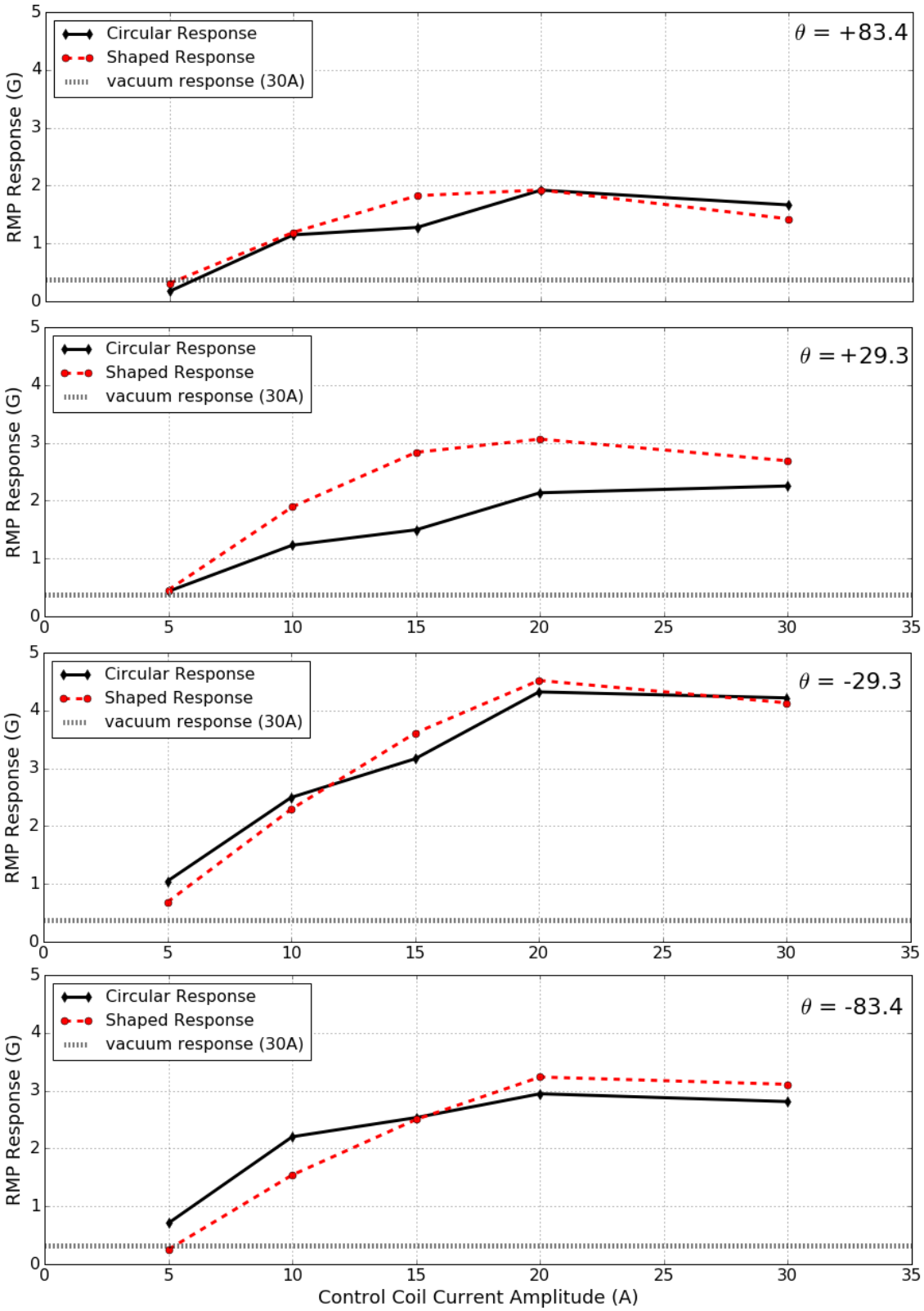

Figure 7.9: Response of shaped and unshaped plasmas to $m = -3$, $n = 1$ perturbations of varying strength. Each data point is a single plasma shot. Dashed line is the vacuum response to a 30A perturbation, establishing a noise floor.

fluctuation by considering only the perturbation and response after both have reached steady state. The correlation coefficient was then used to examine the structure of the response, which was found to be similar to the structure of the mode that naturally dominates the MHD spectrum in unperturbed equilibria in both shaped and circular plasmas. The degree of response to perturbation was then calculated by measuring the strength of the $n = 1$ response on a toroidal ring of feedback array sensors. This response was found to be roughly similar in both shaped and circular plasmas, despite the structure of the perturbation being more resonant with that of the shaped equilibrium's kink mode structure.

Chapter 8

Conclusions and Future Work

This thesis describes the design, construction, installation and qualification of a new poloidal field shaping coil on HBT-EP. Fully diverted plasmas are generated, and methods to aid reliable generation of shaped plasmas are demonstrated. The general performance parameters of diverted HBT-EP plasmas are discussed; MHD behavior has been observed and compared to theory and simulation; a method of estimating the measured field from ideal calculations that takes into consideration sensor location and eddy currents is developed; the response of shaped equilibria to external magnetic perturbations is quantified and compared to circular equilibria.

The equilibrium of shaped plasmas has been computed and the location of the last closed flux surface experimentally verified with a moveable Langmuir probe. The measured structure of the modes in shaped plasmas have been compared to those of limited, circular cross section plasmas, as well as the predictions of theory and computation. A significant difference, near the X-point, is both calculated and consistently observed. The finite element circuit solving code VALEN is used to add the effects of eddy currents driven by the rotation of the kink mode fields to the predictions of DCON for the modes observed on the edge of shaped and circular plasmas.

The intention of this work was to answer four questions about shaped plasmas on HBT-EP. Those four questions have been answered as follows:

1. In regards to whether or not fully diverted operation is possible on HBT-EP, shaped plasma equilibria are numerically determined to be fully diverted and calculated to be stable for many growth times of the no-wall positional instability, allowing study of shaped plasmas in HBT-EP.

2. In regards to the structure of the external kink in a diverted equilibrium, naturally occurring external kink modes are observed to have a structure that is similar to circular plasmas with similar q_*, but with a short-wavelength feature near the X-point. This feature is not observed in circular plasmas, but is consistent with prior calculations and observations of the core and near-edge region of diverted equilibria unstable to external kinks[54]. These modes rapidly grow before the plasma disrupts, and maintain large amplitudes throughout the disruption. Shaped plasmas are found to have shorter lifetimes, more rapid disruptions, and qualitatively different MHD behavior during disruption.

3. In regards to the agreement of the measurements with established theory and simulation, the structure of the external kink modes calculated using the ideal MHD stability code DCON[22, 23], used in combination with the finite-element electromagnetic code VALEN[27], predicts the measured structure of the modes with good accuracy.

4. In regards to the response of diverted plasma equilibria to external magnetic perturbations, shaped equilibria were actively perturbed and the static response has the structure of the naturally occurring, rotating kink mode. Shaped equilibria are observed to have a similar response level, as measured at the sensors, to perturbations as circular plasmas with similar plasma current and major radius.

8.1 The Shaping Coil

A high current, low impedance poloidal field coil is now installed on HBT-EP. It creates local fields sufficient to fully divert HBT-EP plasmas, while having low enough mutual coupling to other coils to allow installation in situ with minimal impact on other vacuum field coils and plasma diagnostics. The pickup on the diagnostic primarily affected, the major radius cosine Rogowski, was quantified and a method of removal derived. After removing the pickup, the plasma current centroid position can be measured with millimeter accuracy.

The location and operating parameters of the shaping coil were selected based on a filamentary model of the plasma, and reconstructions of the plasma shape were performed with TokaMac. The reconstructed equilibria were confirmed using direct measurements of the fields in the vacuum region. The shaping coil is found to apply sufficient poloidal field for diverted operation. The HBT-EP

experiment can now generate diverted plasmas that persist for $\sim$ 4ms, sufficient to observe kink instability mode structure and evolution and to observe the kink response to an applied perturbation.

8.2 Simulations

The free boundary shaped plasma equilibrium is reconstructed from measurements of equilibrium parameters including the outboard edge location by using a floating Langmuir probe. Incorporating this constraint into the reconstruction showed a plasma that is unambiguously diverted. Direct measurement of the poloidal field structure predicted by the model confirms this result, demonstrating studies of diverted or shaped-limited equilibria are possible on HBT-EP.

The ideal MHD stability code DCON was used to predict the $n = 1$ eigenmode spectrum of the equilibrium. Shaped plasmas were found to have unstable eigenmodes with m-spectra dominated by lower m numbers than circular plasmas with similar plasma current and major radius. This is due to the smaller cross sectional area of a shaped plasma, as well as slight oblate ellipticity. This result was confirmed by measurement of the poloidal structure of external kink modes.

The finite element code VALEN was then used to predict the fields measured by sensors, given the plasma cross section, mode helicity, mode rotation frequency, plasma-sensor distance, and eddy currents in nearby conducting structures. Applied to the output of DCON, the agreement between simulation and measurement improved.

8.3 Analysis Methods and Techniques

The imposition of shaping changes the equilibrium fields. The equilibrium subtraction necessary to ensure good separation of modes from the background is made more difficult by the necessity of treating the shaping fields and the associated eddies, as well as the reduction in plasma lifetime after the imposition of shaping. Polynomial fits to the equilibrium signal to isolate both natural fluctuations and response to magnetic perturbations. In the case of a phase flip RMP, a polynomial fit to the equilibrium was found to work well whether the time window was contiguous or not, as long as minor disruptions or other significant and rapid changes to the equilibrium did not occur during the gap. Biorthogonal decomposition was used to separate and reconstruct individual modes from the larger fluctuation set.

8.4 External Kink Structure

The poloidal structure of kinks in the diverted plasma edge was observed with $\sim 11^\circ$ poloidal resolution. They were observed to be similar to the modes as measured in a circular, limited plasma across most of the poloidal circumference of the plasma. Near the location of the X-point the mode is seen to oscillate with a locally shorter poloidal wavelength. This agrees with calculations of both ideal and resistive external kink structure, rather than the predicted peeling-ballooning mode structure[33]. This result further builds on optical diagnostics of the perturbation structure that did not include the plasma edge or scrape-off layer region[54]. The measured modes agree quite well with the predicted structure returned by a combined DCON and VALEN simulation. In particular, the X-point localized features were predicted at the poloidal angle and at the relative amplitude at which they were observed. As far as we are aware, this represents the first observation of this X-point localized feature of an external kink mode in a diverted plasma.

The MHD behavior leading to and following major disruptions are also observed. Odd-n fluctuations were observed using the inboard toroidal array during shaped and circular disruptions. The precursors to the disruption were observed to be roughly similar in frequency and amplitude, with a μsec-scale growth in amplitude immediately before the current spike. Following the current spike, circular plasmas underwent a two-stage disruption, in which the mode persisted at a large amplitude and high frequency, then grew in both amplitude and frequency 0.25ms before the discharge terminates. Shaped plasma disruptions post current spike experienced only the first stage before termination of the discharge.

8.5 RMP Response

Shaped and circular plasmas were perturbed using $m = -3$, $n = 1$ control coil perturbations. The perturbation was applied as a phase flip to allow contrast between the opposing periods of the flip with respect to the equilibrium, and the strength of the response was quantified in such a way as to be insensitive to the growth time of the plasma response. The structure of the excited response was found to be the same as that of the naturally occurring mode.

The response strength as measured at the sensors was found to be similar in amplitude between both cross sections, with both reaching a saturated point after the application of 20A of control coil current. The responses of both shaped and unshaped plasmas are seen to be asymmetric about the

midplane, with the plasmas' response measured to be strongest below the midplane in both cases.

8.6 Future Work

The recent HBT-EP upgrade plan[90] includes the installation of a new dedicated high power horizontal positioning control system. It may be possible to extend the lifetime of a shaped plasma by modifying the vertical field strength with active feedback control.

Shaped plasmas or circular plasmas that are not well centered in the chamber will have poloidally varying coupling (see Figures 8.1 and 8.2) between coils and mode-resonant surface currents. The analysis performed with VALEN to account for geometric and eddy current effects on measured mode signal suggests an extension to the control coils. Coupling between control coils and surface currents, once computed, would allow optimized coupling of any perturbation to a mode of interest. Optimized coupling will reduce demand on power supplies, reducing sidebands and permitting the re-direction of unused power supply overhead to imposition of other external fields for purposes such as static error field control or plasma positioning.

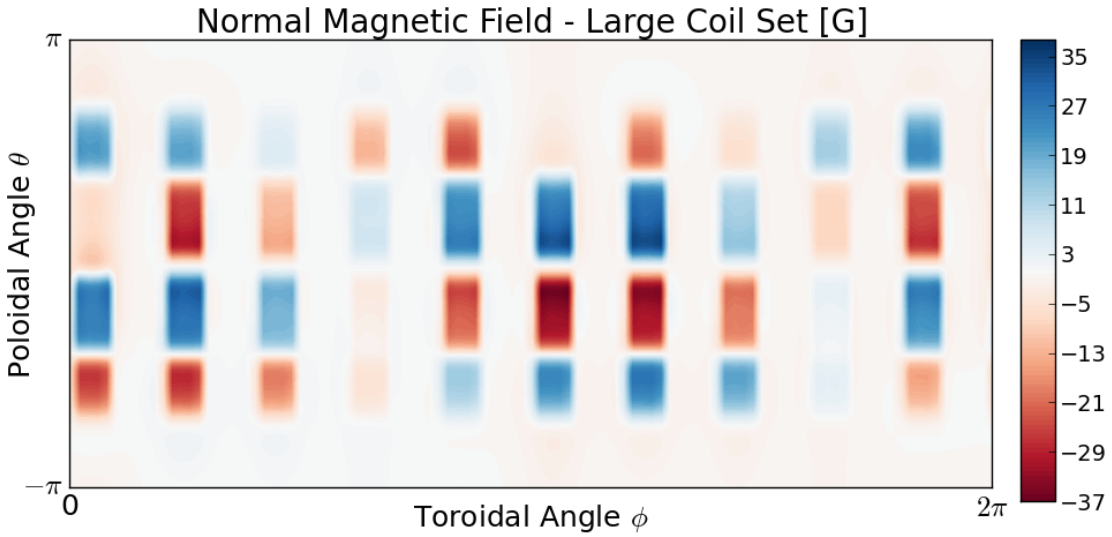

Figure 8.1: The applied normal field on the surface of circular plasma 91347. Plasma is offset outboard from the center of the chamber by 1cm. Note the different poloidal extent of the field applied by midplane vs off-midplane control coils.

The results of the RMP response calculations suggest that the plasma is offset relative to the vertical midplane of the vacuum vessel. There have been indications in past experiments[77] that

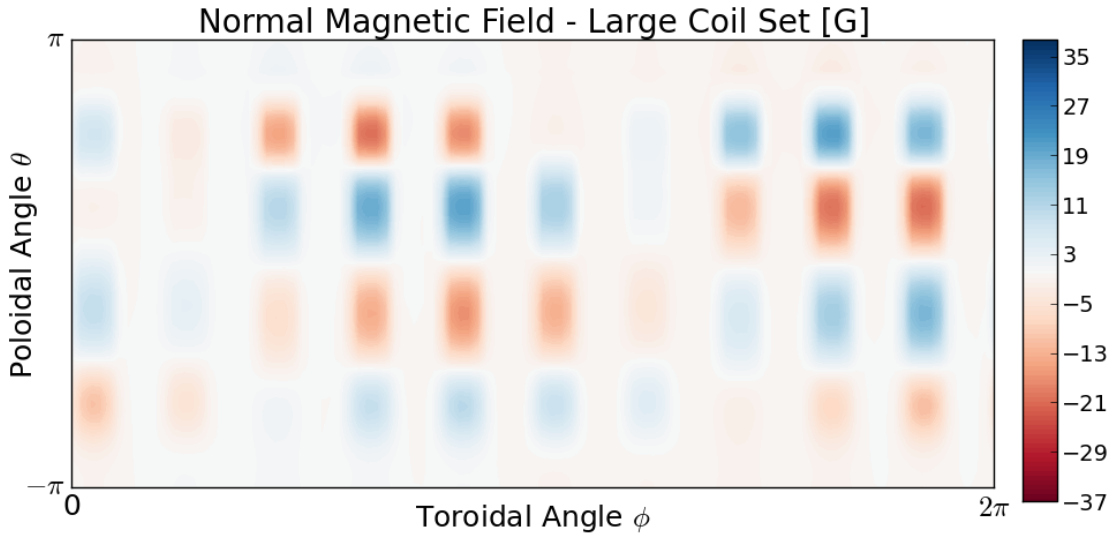

Figure 8.2: The applied normal field on the surface of shaped plasma 90691. Plasma is diverted and offset outboard from the center of the chamber by 1cm. Note the different poloidal extent of the field applied by midplane vs off-midplane control coils, and the poloidally varying strength of the field.

a circular plasma equilibrium is vertically centered below the machine midplane and these results are consistent. By recalculating the VALEN results with the plasma displaced downwards until agreement is found between the VALEN calculations and the results of the RMP response, we can diagnose the vertical offset, and begin to determine if this is due to a misplacement of the vacuum field coils or the chamber in which the plasma is created. A soft X-ray fan array is also scheduled to be installed[90], which will possess a horizontal view centered at the midplane. This should also assist in diagnosing the vertical location of the plasma in the chamber. This array is located at a toroidal location of 18°, and will have a view that is directed towards the X-point, allowing diagnosis of the effects of static errors in the shaping field at that location.

With a corrected model of the chamber and sensors relative to the plasma column, it would be possible to invert the analysis performed in Chapter 6.4. The plasma response to 3D perturbations has been demonstrated to be similar to that of the naturally dominant rotating kink mode in Section 7.4. The observations of the natural mode have in turn been demonstrated to be consistent with the DCON calculated ideal kink mode structure in Chapter 6.5, after using VALEN to include the effects of eddy currents and plasma surface/sensor separation. Rather than using VALEN with DCON to predict the structure of sensor measurements, VALEN could be used with sensor measurements to

estimate the amplitude of the surface mode. Mutual inductances between the sensors and surface mode, as well as for the control coils would allow conversion of coil current and measured mode amplitude could be converted to resonant field applied to the surface, and the resonant response strength at the plasma surface. HBT-EP is instrumented with a 20-point positionable Hall-effect sensor array[91], which could be used to confirm the calculations of near-surface field strength.

Calculating the plasma response after compensating for the effects of plasma location and cross section, as well as the relative location and eddy current environment of sensors on the measurements of those sensors, represents a significant advancement in HBT-EP's mode control and measurement. This would permit accurate mode analysis with arbitrary shell/plasma configurations, and full utilization of HBT-EP's shell positioning and plasma cross section control. This method of parameterizing the response of the plasma to perturbations in terms of the strength of the applied and response fields at the plasma surface could be generalized to other experiments, giving a machine-independent calculation of resonant field amplification.

Upgrades to HBT-EP will allow equilibrium reconstructions that are more precise than have been previously possible. A high-power Thomson Scattering laser system has been acquired and installed on HBT-EP and work is being performed to allow multi-point measurements of electron density and temperature[92]. The planned soft X-ray array will compose multiple views of the plasma, along multiple chords from each viewpoint. Additionally, HBT-EP is instrumented with many diamagnetic loops and flux loops that are currently not operable, but could be refurbished and used to more sharply define the current profiles and plasma shape[74]. With added precision in diagnosis of the plasma current and pressure profiles, it would be possible to develop circular and shaped equilibria that are more similar in MHD structure and stability than was possible for this research.

Given shaped and circular plasmas with significantly similar core pressures, plasma currents, and associated profiles, direct quantification of the response to perturbations and/or feedback of unstable MHD kinks would be possible. Combining our ideal MHD models of the plasma and kink modes with VALEN models of the conductors will permit the MHD of these equilibria to be examined without regard for plasma location in the chamber or sensor/actuator coupling.

A project to study and characterize currents driven outside the LCFS on HBT-EP is underway[93]. Upgrades are planned that will install biasable plates at several locations that will protrude into the scrape-off layer (Figure 8.3). When activated, currents will be driven along the field lines that

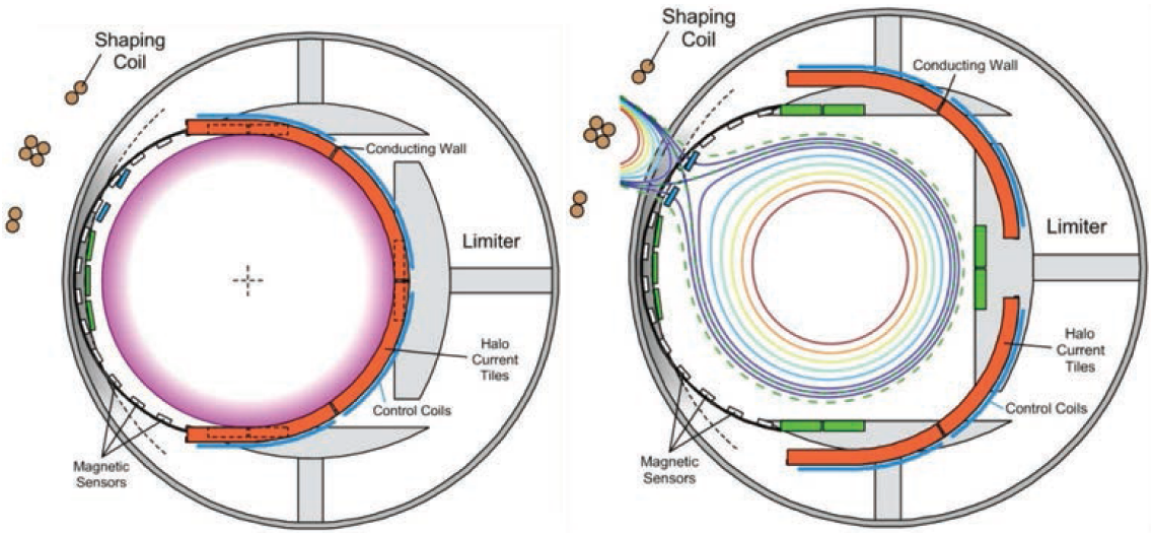

Figure 8.3: Planned upgrade to HBT-EP. Multiple tiles will be installed to capture and measure currents located in the scrape off layer within 1cm of the LCFS. Certain tiles will drive currents along the SOL field lines. Highly edge-resonant fields will be imposed by SOL currents.

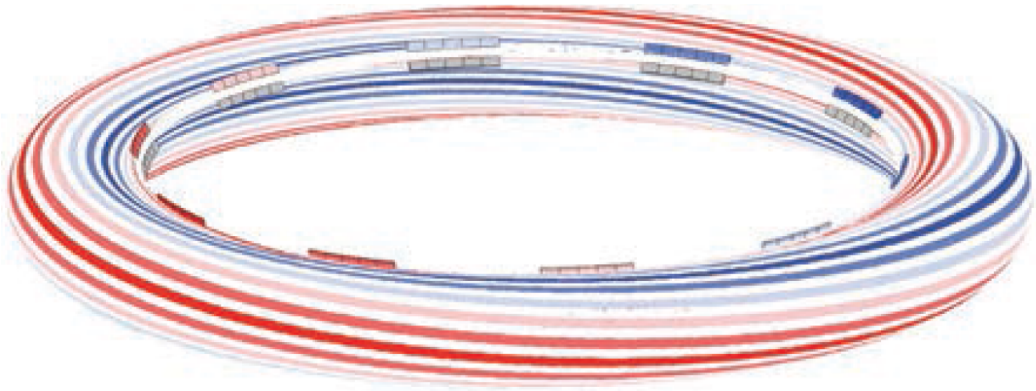

Figure 8.4: The scrape-off layer of a shaped plasma, biased by the X-point localized biasing plates. Biased field lines/surface currents are color coded with regards to the plates that bias them. Highly resonant nature of the currents, and large amount of surface coverage is seen.

intersect these plates. The field lines just outside the plasma edge will conduct field-aligned currents that are highly resonant with the plasma edge, very near to the plasma edge, and widely and smoothly distributed across the outer surface of the plasma. Ensuring this effect for shaped plasmas represents a greater engineering challenge due to the strong radial shear near the LCFS[94, 95] in a diverted plasma. But if the currents can be sufficiently localized in the minor radial direction, then the SOL currents can traverse almost 360° of poloidal angle before intersecting another material surface (see Figure 8.4), and interaction with the plasma can be quite strong. The same analysis

performed in this thesis, of using VALEN to predict the applied field from a set of currents and to calculate the response field from a measured signal, can be applied to these experiments as well.

Bibliography

[1] Gaye, A. Access to Energy and Human Development. *United Nations Development Program - Human Development Report*, **25**:1–22, 2008.

[2] Hoffert, M.I., Caldeira, K., Benford, G., Criswell, D.R., Green, C., Herzog, H., Jain, A.K., Kheshgi, H.S., Lackner, K.S., Lewis, J.S., Lightfoot, H.D., Manheimer, W., Mankins, J.C., Mauel, M.E., Perkins, L.J., Schlesinger, M.E., Volk, T., Wigley, T.M.L. Advanced Technology Paths to Global Climate Stability: Energy for a Greenhouse Planet. *Science*, **298**:981–987, 2002.

[3] Smith, C.L., Cowley, S. The Path to Fusion Power. *Philosophical Transactions of the Royal Society*, **368**:1091–1108, 2010.

[4] Jacquinot, J. Fifty Years in Fusion and the Way Forward. *Nuclear Fusion*, **50**(1):014001, 2010.

[5] Ongena, J., Koch, R., Wolf, R., Zohm, H. Magnetic-Confinement Fusion. *Nature Physics*, **12**:398–409, 2016.

[6] Jacquinot, J., Keilhacker, M., and Rebut, P. Chapter 2: Mission And Highlights Of The Jet Joint Undertaking: 1978-1999. *Fusion Science and Technology*, **53**(4):866–890, 2008.

[7] Strait, E.J. Stability of High Beta Tokamak Plasmas. *Physics of Plasmas*, **1**(5):1415–1431, 1994.

[8] Artisimovich, L. A., Shafranov, V.D. Tokamak with Non-Round Section of the Plasma Loop. *Journal of Experimental and Theoretical Physics Letters*, **15**(1):51–4, 1972.

[9] Pitts, R.A., Kukushkin, A., Loarte, A., Martin, A., Merola, M., Kessel, C.E., Komarov, V., Shimada, M. Status and Physics Basis of the ITER Divertor. *Physica Scripta*, **T138**:014001, 2009.

[10] Najmabadi, F., Bathke, C.G., Billone, M.C., Blanchard, J.P.., Bromberg, L., Chin, E., Cole, F.R., Crowell, J.A., Ehst, D.A., El-Guebaly, L.A., Herring, S., Hua, T.Q., Jardin, S.C., Kessel, C.E., Khater, H., Lee, D., Malang, S., Mau, T., Miller, R.L., Sidorov, M., Steiner, D., Sviatoslavsky, I., Sze, D. Thayer, R., Tillack, M.S., Titus, P., Wagner, L.M., Wang, X., Wong, C.P.C. Overview of the ARIES-RS Reversed-Shear Tokamak Power Plant Study. *Nuclear Fusion*, **56**(6):066008, 2016.

[11] Mauel, M.E., Navratil, G.A., Sabbagh, S.A., Bell, M.G., Budny, R.V., Fredrickson, E.D., Hawryluk, R.J., Janos, A.C., Johnson, D.W., McCune, D.C., McGuire, K.M., Medley, S.S., Mueller, D., Owens, D.K., Park, H.K., Ramsey, A.T., Stratton, B.C., Synakowski, E.J., Taylor, G., Wieland, R.M., Zarnstorff, M.C., Kesner, J., Marmar, E.S., Terry, J.L. Operation at the Tokamak Equilibrium Poloidal Beta Limit in TFTR. *Nuclear Fusion*, **32**(8):1468–73, 1992.

[12] Martins, Caroline G.L., Roberto, M., Caldas, I.L. Delineating the magnetic field line escape pattern and stickiness in a poloidally diverted tokamak. *Physics of Plasmas*, **21**(8):082506, 2014.

[13] Bateman, G. *MHD Instabilities*. The MIT Press, 1978.

[14] Mukhovatov, V.S., Shafranov, V.D. Plasma Equilibrium In a Tokamak. *Nuclear Fusion*, **11**(8):605–633, 1971.

[15] Lipschultz, B., Praeger, S.C., Todd, A.M.M., Delucia, J. Axisymmetric Instability in a Non-Circular Tokamak: Experiment and Theory. *Nuclear Fusion*, **20**(6):683, 1980.

[16] Fukuyama, A., Seki, S., Momota, H., Itatani, R. Positional Instabilities in a Tokamak with a Resistive Shell. *Japanese Journal of Applied Physics*, **14**(6):871, 1975.

[17] Lawson, J. D. Some Criteria for a Power Producing Thermonuclear Reactor. *Proceedings of the Physical Society*, **70**(1), 1956.

[18] Wesson, J. *Tokamaks*. Clarendon Press, 1997.

[19] Troyon, F., Gluber, R. A Semi-Empirical Scaling Law For The β-Limit in Tokamaks. *Physics Letters*, **110A**(1), 1985.

[20] Ferron, J.R., Casper, T.A., Gohil, P., Greenfield, C.M., Hyatt, A.W., Jayakumar, R.J., Kessel, C., Luce, T.C., Makowski, M.A., Menard, J., Murakami, M., Petty, C.C., Politzer, P.A., Taylor, T.S., Wade, M.R. Optimization of DIII-D Advanced Tokamak Discharges with Respect to the β Limit. *Physics of Plasmas*, **5**(12), 2004.

[21] Sabbagh, S.A., Sontag, A.C., Bialek, J.M., Gates, D.A., Glasser, A.H., Menard, J.E., Zhu, W., Bell, M.G., Bell, R.E., Bondeson, A., Bush, C.E., Callen, J.D., Chu, M.S., Hegna, C.C., Kaye, S.M., Lao, L.L., LeBlanc, B.P., Liu, Y.Q., Maingi, R., Mueller, D., Shaing, K.C., Stutman, D., Tritz, K., Zhang, C. Resistive Wall Stabilized Operation in Rotating High Beta NSTX Plasmas. *Nuclear Fusion*, **5**(46), 2006.

[22] Glasser, A.H. The Direct Criterion of Newcomb For the Ideal MHD Stability of an Axisymmetric Toroidal Plasma. *Physics of Plasmas*, **23**(7):072505, 2016.

[23] Glasser, A.H., Chance, M.S. Determination of Free Boundary Ideal MHD Stability with DCON and VACUUM. *Bulletin of the American Physics Society*, **42**:1848, 1997.

[24] Freidberg, J.P. *Ideal Magnetohydrodynamics*. Cambridge University Press, 2014.

[25] Hanson, J.M., De Bono, B., James, R.W., Levesque, J.P., Mauel, M.E., Maurer, D.A., Navratil, G.A., Pedersen T.S., Shiraki, D. Feedback Suppression of Rotating External Kink Instabilities in the Presence of Noise. *Physics of Plasmas*, **15**(8):080704, 2008.

[26] Jahns, G.L., Chance, M.S., Kaye, S.M., Manickam, J., Takahashi, H., LeBlanc, B., Morris, A.W., Reusch, M., Sesnic, S. MHD Analysis of high $\langle\beta_t\rangle$ Disruptions in PBX. *Nuclear Fusion*, **28**(5):881–9, 1988.

[27] Bialek, J., Boozer, A., Mauel, M., Navratil, G.A. Modeling of Active Control of External Magnetohydrodynamic Instabilities. *Physics of Plasmas*, **8**(5):2170–80, 2001.

[28] Gimblett, C., Hastie, R. J., Van der Linden, R. A. M., Wesson, J. A. Non-Uniform Rotation and the Resistive Wall Mode. *Physics of Plamas*, **3**(10):3619–3627, 1996.

[29] Cates, C., Shilov, M., Mauel, M.E., Navratil, G.A., Maurer, D., Mukherjee, S., Nadle, D., Bialek, J., and Boozer, A. Suppression of Resistive Wall Instabilities with Distributed, Independently Controlled, Active Feedback Coils. *Physics of Plasmas*, **7**(8):3133–6, 2000.

[30] Sabbagh, S.A., Berkery, J.W., Bell, R.E., Bialek, J.M., Gerhardt, S.P., Menard, J.E., Betti, R., Gates, D.A., Hu, B., Katsuro-Hopkins, O.N., LeBlanc, B.P., Levinton, F.M.,Manickam, J., Tritz, K, Yuh, H. Advances in Global MHD Mode Stabilization Research on NSTX. *Nuclear Fusion*, **50**(2):025020, 2010.

[31] Goedbloed, J.P., Pfirsch, D. Tasso, H. Instbility of a Pinch Surrounded by a Resistive Wall. *Nuclear Fusion*, **12**(6):649–57, 1972.

[32] Turnbull, A.D., Hanson, J.M., Turco, F., Ferraro, N.M., Lanctot, M.J., Lao, L.L., Strait, E.J., Piovesan, P., Martin4, P. The External Kink Mode in Diverted Tokamaks. *Journal of Plasma Physics*, **82**(3), 2016.

[33] Huysmans, G.T.A. External Kink (Peeling) Modes in X-point Geometry. *Plasma Physics and Controlled Fusion*, **47**(12), 2005.

[34] C. Gimblett. On free boundary instabilities induced by a resistive wall. *Nuclear Fusion*, **26**(5):617, 1986.

[35] Strait, E.J., Taylor, T. S., Turnbull, A. D., Ferron, J.R., Lao, L.L. Rice, B., Sauter, O., Thompson, S.J., Wroblewski, D. Wall Stabilization of High Beta Tokamak Discharges in DIII-D. *Physical Review Letters*, **74**(13):2483–6, 1995.

[36] Rath, N., Byrne, P.J., Levesque, J.P., Angelini, S., Bialek, J., DeBono, B., Hughes, P., Mauel, M.E., Navratil, G.A., Peng, Q., Rhodes D.J., Stoafer, C.C. Adaptive feedback control of rotating external kink modes in HBT-EP. *Nuclear Fusion*, **53**:073052, 2013.

[37] Peng, Q., Levesque, J.P., Stoafer, C.C., Bialek, J., Byrne, P., Hughes, P.E., Mauel, M.E., Navratil, G.A., Rhodes, D.J. Improved feedback control of wall stabilized kink modes with different plasma-wall couplings and mode rotation. *Plasma Physics and Controlled Fusion*, **58**:045001, 2016.

[38] Ryutov, D.D., Cohen, R.H., Rognlien, T.D., Umansky, M.V. The Magnetic Field Structure of a Snowflake Divertor. *Physics of Plasmas*, **15**(9):092501, 2008.

[39] Schmitz, O., Becoulet, O.M., Cahyna, P., Evans, T.E., Feng, Y., Frerichs, H., Loarte, A., Pitts, R.A., Reiser, D., Fenstermacher, M.E., Harting, D., Kirschner, A., Kukushkin, A., Lunt, T., Saibene, G., Reiter, D., Samm, U., Wiesen, S. Three-Dimensional Modeling of Plasma Edge Transport and Divertor Fluxes During Application of Resonant Magnetic Perturbations on ITER. *Nuclear Fusion*, **56**(6):066008, 2016.

[40] Unterberg, E.A., Schmitz, O., Evans, T.E., Maingi, R., Brooks, N.H., Fenstermacher, M.E., Mordijck, S., Moyer, R.A., Orlov, D.M. The Effects of an Open and Closed Divertor on Particle Exhaust During Edge-Localized Mode Suppression by Resonant Magnetic Perturbations in DIII-D. *Nuclear Fusion*, **50**(3):034011, 2010.

[41] Shafer, M.W., Unterberg, E.A., Wingen, A., Battag, D.J. Plasma Response Measurements of Non-Axisymmetric Magnetic Perturbations on DIII-D via Soft X-ray Imaging). *Physics of Plasmas*, **21**(12), 2014.

[42] Shiraki, D. *High-Resolution MHD Spectroscopy of External Kinks in a Tokamak Plasma*. PhD thesis, Columbia University, 2012.

[43] Shiraki, D., Angelini, S.M., Byrne, P., DeBono, B.A., Hughes, P.E., Levesque, J.P., Mauel, M.E., Maurer, D.A., Navratil, G.A., Peng,Q., Rath, N., Rhodes, D.J., Stoafer, C.C. Measurement of 3D Plasma Response to External Magnetic Perturbations in the Presence of a Rotating External Kink. *Physics of Plasmas*, **20**(10):102503, 2013.

[44] Shilov, M.A. *Measurement of the Response of External Kink Modes to Resonant Magnetic Perturbation in HBT-EP Tokamak Plasmas*. PhD thesis, Columbia University, 2005.

[45] Robinson, D. C. Ten Years of Results from the TOSCA Device. *Nuclear Fusion*, **25**(9):1101, 1985.

[46] Helton, F. J., Wang, T. S. MHD Equilibrium in Non-Circular Tokamaks with Field-Shaping Coil Systems. *Nuclear Fusion*, **18**(11):1523, 1978.

[47] Bol, K., Okabayashi, M., Fonck R. The Poloidal Divertor Experiment (PDX) and the Princeton Beta Experiment (PBX). *Nuclear Fusion*, **25**(9):1149, 1985.

[48] Evans, T.E., Fenstermacher, M.E., Moyer, R.A., Osborne, T.H., Watkins, J.G., Gohil, P., Joseph, I., Schaffer, M.J., Baylor, L.R., Bécoulet, M.B., Boedo, J.A., Burrell, K.H., deGrassie, J.S., Finken, K.H., Jernigan, T., Jakubowski, M.W., Lasnier, C.J., Lehnen, M., Leonard, A.W., Lonnroth, J., Nardon, E., Parail, V., Schmitz, O., Unterberg B., West W.P. RMP ELM Suppression in DIII-D Plasmas with ITER Similar Shapes and Collisionalities. *Nuclear Fusion*, **48**(2):024002, 2008.

[49] Evans, T.E., Moyer, R.A., Watkins, J.G., Osborne, T.H., Thomas, P.R., Bécoulet, M., Boedo, J.A., Doyle, E.J., Fenstermacher, M.E., Finken, K.H., Groebner, R.J., Groth, M., Harris, J.H., Jackson, G.L., La Haye, R.J., Lasnier, C.J., Masuzaki, S., Ohyabu, N., Pretty, D.G., Reimerdes, H., Rhodes, T.L., Rudakov, D.L., Schaffer, M.J., Wade, M.R., Wang, G., West W.P., Zeng L. Suppression of Large Edge Localized Modes With Edge Resonant Magnetic Fields in High Confinement DIII-D Plasmas. *Nuclear Fusion*, **45**(7):595607, 2005.

[50] Loarte, A. Effects of Divertor Geometry on Tokamak Plasmas. *Plasma Physics and Controlled Fusion*, **43**(6):R183–224, 2001.

[51] Gates, D. A., Maingi, R., Kaye, S, Sabbagh, S. A., et. al. Effect of Plasma Shaping on Performance in the National Spherical Torus Experiment. *Physics of Plasmas*, **13**(5):056122, 2006.

[52] Turnbull, A.D., Lin-Liu, Y.R., Miller, R.L., Taylor, T.S., Todd, T.N. Improved Magnetohydrodynamic Stability Through Optimization of Higher Order Moments in Cross-Section of Tokamaks. *Physics of Plasmas*, **55**:095009, 1998.

[53] Camenen, Y., Bortolon, A., Duval, B.P., Federspiel, L., Peeters, A. G., Casson, F. J., Hornsby, W. A., Karpushov, A. N., Piras, F., Sauter, O., Snodin, A. P., Szepesi, G. Experimental Demonstration of an Up-Down Asymmetry Effect on Intrinsic Rotation in the TCV Tokamak. *Plasma Physics and Controlled Fusion*, **52**:124037, 2010.

[54] Huysmans, G.T.A., Hender, T.C., Alper B. Identification of External Kink Modes in JET. *Nuclear Fusion*, **38**(2):901, 1998.

[55] Sankar, M.K., Eisner, E., Garofalo, A., Gates, D., Ivers, T.H., Kombargi, R., Mauel, M.E., Maurer, D., Nadle, D., Navratil, G.A., Xiao Q. Initial High Beta Operation of the HBT-EP Tokamak. *Journal of Fusion Energy*, **12**(3):303–310, 1993.

[56] Maurer, D.A., Bialek, J., Byrne, P.J., DeBono, B., Levesque, J.P., Li, B.Q., Mauel, M.E., Navratil, G.A., Pedersen, T.S., Rath, N., Shiraki, D. The High Beta Tokamak-Extended Pulse Magnetohydrodynamic Mode Control Research Program. *Plasma Physics and Controlled Fusion*, **53**(7):074016, 2011.

[57] P.E. Hughes, J.P. Levesque, N. Rivera, M.E. Mauel, and G.A. Navratil. Design and installation of a ferromagnetic wall in tokamak geometry. *Review Scientific Instruments*, **86**(10):103504, 2015.

[58] Shiraki, D., Levesque, J.P., Bialek, J., Byrne, P.J., DeBono, B.A., Mauel, M.E., Maurer, D.A., Navratil, G.A., Pedersen, T.S., Rath, N. In Situ "Artificial Plasma" Calibration of Tokamak Magnetic Sensors. *Review of Scientific Instruments*, **84**(69):063502, 2013.

[59] Maurer, D., Shiraki, D., Levesque, J.P., Bialek, J., Angelini, S., Byrne, P.J., DeBono, B., Hughes, P.E., Mauel, M.E., Navratil, G.A., Peng, Q., Rhodes, D., Rath, N., Stoafer, C.C. High Resolution detection and Excitation of Resonant Magnetic Perturbations in a Wall-Stabilized Tokamak. *Physics of Plasmas*, **19**(5):056123, 2012.

[60] Levesque, J.P., Rath, N., Shiraki, D., Angelini, S., Bialek, J., Byrne, P.J., DeBono, B.A., Hughes, P.E., Mauel, M.E., Navratil, G.A., Peng, Q, Rhodes, D.J., Stoafer, C.C. Multimode Observations and 3D Magnetic Control of the Boundary of a Tokamak Plasma. *Nuclear Fusion*, **53**(7):073037–45, 2013.

[61] Levesque, J.P., Rath, N., Shiraki, D., Angelini, S., Bialek, J., Byrne, P., DeBono, B., Mauel, M.E., Navratil, G.A., Peng, Q., Rhodes, D., Stoafer, C. High-Resolution Detection and 3D Magnetic Control of the Helical Boundary of a Wall-Stabilized Tokamak Plasma. *IAEA Fusion Energy Conference, San Diego, CA, 2012*, **44**(27):074016, 2012.

[62] Angelini, S., Levesque, J.P., Mauel, M.E., Navratil, G.A. High-Speed Imaging of the Plasma Response to Resonant Magnetic Perturbations in HBTEP. *Plasma Physics and Controlled Fusion*, **57**(4):074016, 2015.

[63] Rath, N., Angelini, S., Bialek, J., Byrne, P.J., DeBono, B., Hughes, P., Levesque, J.P., Mauel, M.E., Navratil, G.A., Peng, Q., Rhodes D.J., Stoafer, C. Adaptive control of rotating magnetic perturbations in HBT-EP using GPU processing. *Plasma Physics and Controlled Fusion*, **55**(8):073052, 2013.

[64] J.P. Levesque, P.E. Hughes, J. Bialek, P.J. Byrne, M.E. Mauel, G.A. Navratil, Q. Peng, D.J. Rhodes, C.C. Stoafer. Active and passive kink mode studies in a tokamak with a movable ferromagnetic wall. *Physics of Plasmas*, **22**(5):056102, 2015.

[65] Wadhwa, C.L. *High Voltage Engineering - 2nd Ed.* New Age International, 2007.

[66] Hutchinson, I.H. *Principles of Plasma Diagnostics.* Cambridge University Press, 2002.

[67] Hughes, P.E. *MHD Effects of a Ferritic Wall on Tokamak Plasmas.* PhD thesis, Columbia University, 2016.

[68] Stoafer, C.C. *Study of kink modes and error fields through rotation control with a biased electrode.* PhD thesis, Columbia University, 2016.

[69] Humphreys, D.A. *Axisymmetric Control in Tokamaks.* PhD thesis, Massachusetts Institute of Technology, 1991.

[70] Swain, D.H., Neilson, G.H. An Efficient Technique for Magnetic Analysis of Non-Circular, High-Beta Tokamak Equilibria. *Nuclear Fusion*, **22**(8):1015–30, 1982.

[71] Mauel, M.E., Ivers, T.H., Che, H.Y., Chen, D., Gates, D., Marshall, T.C., Navratil, G.A., Wang, J. Measurement of MHD Instabilities in High Beta Tokamaks. *Proceedings of the Twelfth International Conference on Plasma Physics And Controlled Nuclear Fusion Research, IAEA, Nice 1988*, **1**:415–421, 1988.

[72] Garofalo, A.M., Eisner, E., Ivers, T.H., Kombargi, R., Mauel, M.E., Maurer, D., Nadle, D., Navratil, G.A.,Vijaya Sankar, M.K., Taylor, E., Xiao, Q. Stabilization of Kink Instabilities by Eddy Currents in a Segmented Wall and Comparison With Ideal MHD Theory. *Nuclear Fusion*, **38**(7):1029, 1998.

[73] Johnson, J.L., Dahlhed, H.E., Greene, J.M., Grimm, R.C., Hsieh, Y.Y., Jardin, S.C., Manickam, J., Okabayashi, M., Storer, R.G., Todd, A.M.M., Voss, D.E., and Weimer, K.E. Numerical Determination of Axisymmetric Toroidal Magnetohydrodynamic Equilibria. *Journal of Computational Physics*, **6**:212–34, 1979.

[74] Lao, L.L., St. John, H., Stambaugh, R.D., Kellman, A.G., Pfieffer, W. Reconstruction of Current Profile Parameters and Plasma Shapes in Tokamaks. *Nuclear Fusion*, **25**(11):1611–22, 1985.

[75] Levesque, J. P., Litzner, K. D., Mauel, M. E., Maurer, D. A., Navratil, G. A., Pedersen, T. S. A High-Power Spatial Filter for Thomson Scattering Stray Light Reduction. *Review of Scientific Instruments*, **82**:033501, 2016.

[76] Levesque, J.P. *Multimode Structure of Resistive Wall Modes near the Ideal Wall Stability Limit.* PhD thesis, Columbia University, 2012.

[77] Levesque, J.P., Byrne, P.J., DeBono, B., LI, B., Mauel, M.E., Maurer, D.A., Navratil, G.A., Rath, N., Shiraki, D. Control of Static and Dynamic Non-axisymmetric Magnetic Fields in HBT-EP. *52nd Annual Meeting of the APS Division of Plasma Physics*, 2010.

[78] Van Der Veen, A., Deprettre, E.F, Sindlehurst, A.L. Subspace-Based Signal Analysis Using Singular Value Decomposition. *Proceedings of the IEEE*, **81**(9):1277, 1993.

[79] Dudok de Wit, T., Pecquet, A.L., Vallet, J.-C., Lima, R. Biorthogonal Decomposition as a Tool for Investigating Fluctuations in Plasmas. *Physics of Plasmas*, **1**(10):3288, 1994.

[80] Dudok de Wit, T. Enhancement of Multichannel Data in Plasma Physics by Biorthogonal Decomposition. *Plasma Physics and Controlled Fusion*, **37**(2):117–35, 1995.

[81] Ravoux, J.F., Le Gal,P. Biorthogonal Decomposition Analysis and Reconstruction of Spatiotemporal Chaos Generated by Coupled Wakes. *Physical Review E. Statistical Physics, Plasmas, Fluids, and Related Interdisciplinary Topics*, **58**(5):5233–36, 1998.

[82] Dong, L.F., Zhang, Q.L., Wang, L. Identification of Short-Lived and Localized Coherent Structures in Plasma Turbulence by Window Biorthogonal Decomposition. *Review of Scientific Instruments*, **74**(12):5093–6, 2003.

[83] Angelini, S. *High-Speed Videography on HBT-EP*. PhD thesis, Columbia University, 2014.

[84] Rath, N. *GPU-based, Microsecond Latency, Hecto-Channel MIMO Feedback Control of Magnetically Confined Plasmas*. PhD thesis, Columbia University, 2012.

[85] Hender, T.C., Allfrey, S.J., Akers, R., Appel, L.C., Bevir, M.K., Buttery, R.J., Gryaznevich, M., Jenkins, I., Kwon, O.J., McClements, K.G., Martin, R., Medvedev, S., Nightingale, M.P.S., Ribeiro, C., Roach, C. M., Robinson, D.C., Sharapov, S.E., Sykes, A., Villard, L., Walsh, M. J. Magneto-hydro-dynamic Limits in Spherical Tokamaks. *Physics of Plasmas*, **6**(5):1958–68, 1999.

[86] Reimerdes, H., Hender, T.C., Sabbagh, S.A., Bialek, J.M., Chu, M.S., Garofalo, A.M., Gryaznevich, M.P., Howell, D.F., Jackson, G.L.. La Haye, R.J., Liu, Y.Q., Menard, J.E., Navratil, G.A., Okabayashi, M., Pinches, S.D., Sontag, A.C., Strait, E.J., Zhu, W., Bigi, M., de Baar, M., de Vries, P., Gates, D.A., Gohil, P., Groebner, R.J., Mueller, D., Raman, R. Cross-machine comparison of resonant field amplification and resistive wall mode stabilization by plasma rotation. *Physics of Plasmas*, **13**(5):056107, 2006.

[87] Atanasiu, C.V., Boozer, A.H., Zakharov, L.E., Subbotin, A.A., Miron, G.I. Determination of the Vacuum Field Resulting From the Perturbation of a Toroidally Symmetric Plasma. *Physics of Plasmas*, **6**(7):2781–90, 1999.

[88] Park, Y.S., Sabbagh, S.A., Bak, J.G., Bialiek, J.M., Berkery, J.W., Lee, S.G., Oh, Y.K. Resistive Wall Mode Active Control Physics. *Physics of Plasmas*, **21**:012513, 2014.

[89] Hanson, J.M., Bialek, J., Turco, F., King, J., Navratil, G.A., Strait, E.J., Turnbull, A.D. Validation of Conducting Wall Models Using Magnetic Measurements. *Nuclear Fusion*, **56**(10):106022, 2016.

[90] G.A. Navratil. High Beta Tokamak Research. *Grant proposal*, 2016.

[91] Liu, Y., Maurer, D.A., Navratil, G.A., Rivera, N. High Spatial Resolution Hall Sensor Array for Edge Plasma Magnetic Field Measurements. *Review of Scientific Instruments*, **79**:093501, 2005.

[92] Stoafer, C.C., Levesque, J.P., Mauel, M.E., Navratil, G.A., McLean, H.S. Multi-Point Thomson Scattering Upgrade and Measurements on HBT-EP. *55th Annual Meeting of the APS Division of Plasma Physics*, 2013.

[93] Levesque, J.P., Brooks, J.W., Abler, M.C., Bialek, J., Byrne, P.B., Hansen, C.J., Hughes, P.E., Mauel, M.E., Navratil, G.A., Rhodes, D.J. Measurement of Scrape-Off-Layer Current Dynamics During MHD Activity and Disruptions in HBT-EP. *Nuclear Fusion*, **Submitted**, 2017.

[94] Joseph, I., Cohen, R.H., Ryutov, D.D. Driving Toroidally Asymmetric Current Through the Tokamak Scrape-off layer. I. Potential For Edge Localized Mode Suppression. *Physics of Plasmas*, **16**:052510, 2009.

[95] Joseph, I. Driving Toroidally Asymmetric Current Through the Tokamak Scrape-off Layer. II. - Magnetic Field Structure and Spectrum. *Physics of Plasmas*, **16**:052511, 2009.

Appendix A

Mechanical Drawings

This Appendix contains CAD drawings of the strike point limiter and the coil holders, with a brief explanation of the theory of operation for each subsystem.

A.1 The Strike-Point Limiters

The 316 stainless steel strike-point limiters are located along the upper half of the inboard side of the chamber piece flange that serves as the inboard limiter. One each is mounted to the flange of chambers at toroidal angles $\phi = -72$ and $\phi = 108$, in which a poloidal array sensor ring is located. With a circular cross section plasma, the plasma is limited to a smaller minor radius than the poloidal array and if the plasma is centered at the midplane, the poloidal array is shadowed by the chamber flange. However, the chamber is not concentric with the plasma, and so the poloidal array is physically behind the flange only along a narrow band of poloidal angle near the inboard midplane. This is acceptable in the case of a circular plasma, as the plasma-sensor separation will be no less than the separation imposed by the flange.

In the case of a shaped plasma, the LCFS will bulge towards the shaping coil, at which angle the PA sensors are unshadowed. Each sensor is shielded with 64μm thick stainless steel shimstock, but this shielding was selected to withstand only the tenuous SOL plasma in that location. As shaping is increased to the point of diversion, not only will the poloidal array sensors at the X-point be the nearest limiting surface to the LCFS, SOL plasma flux will free stream towards the X-point, and the nearby PA sensors. The sensors will then serve as the limiter without added protection.

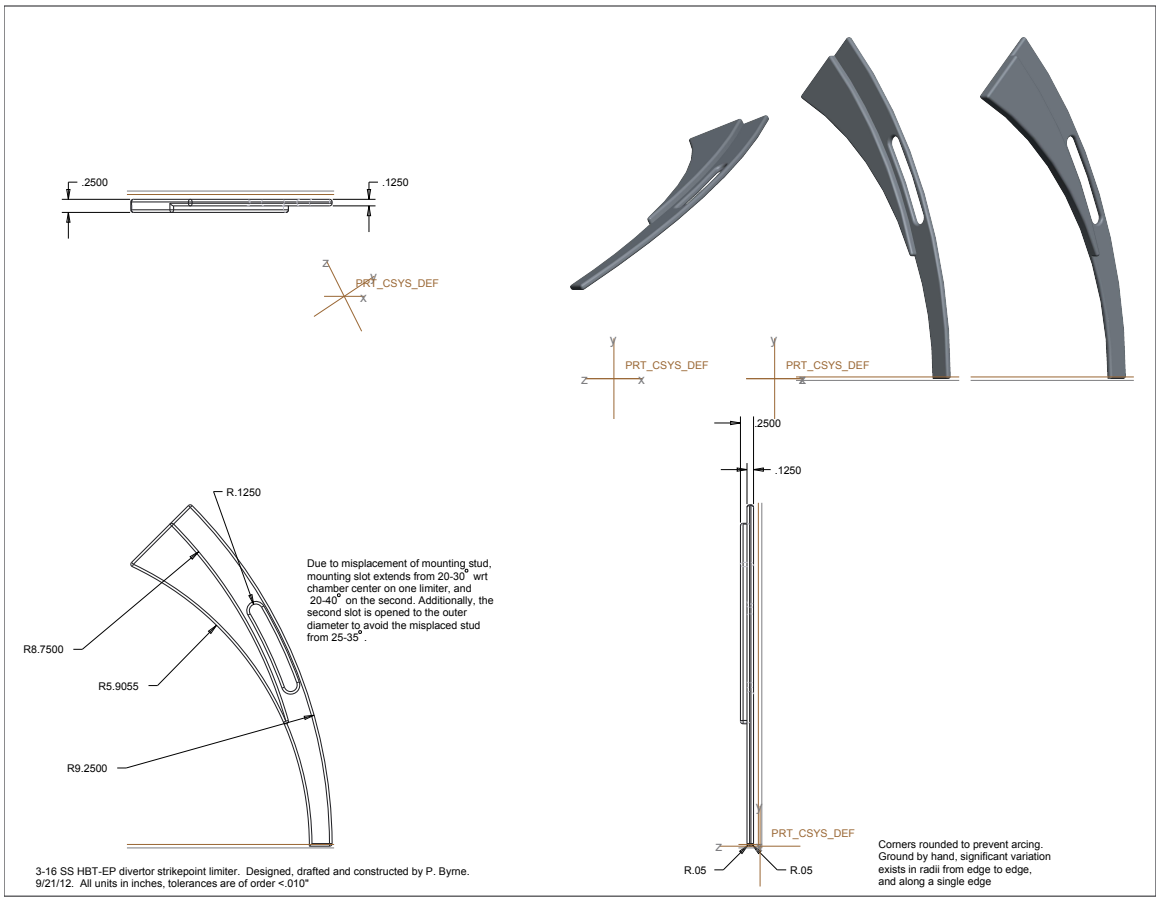

Figure A.1: CAD Drawing of the strike-point limter.

Each strike point limiter mounts directly to the chamber flange. Correct radial positioning is ensured by a cut-out notch into which the flange corner slots. The limiter is fastened to the flange by nuts threaded onto two rods spot-welded to the flange. The inner and outer edges of the limiter have different radii of curvature, and it is thus necessary to ensure that poloidal positioning is precise. This is achieved by ensuring the lower edge of the limiter is even with the machine midplane, demarcated with a laser level. The limiting surface is 0.25" thick and extends to 60 degrees above the inboard midplane, or from 120-180° of poloidal angle, as measured from the outboard midplane. Relevant dimensions for the limiter can be found in Figure A.1

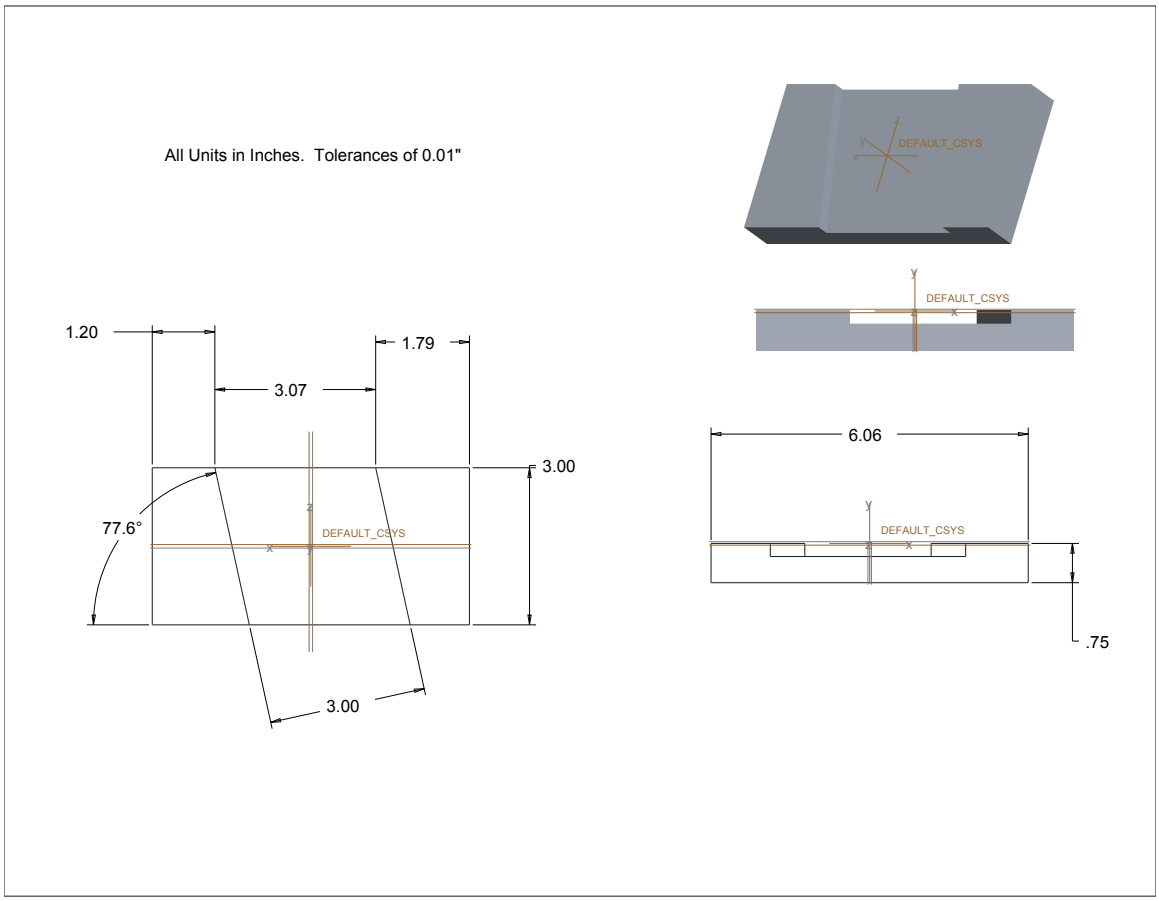

Figure A.2: CAD Drawing of the coil holder mount.

A.2 The Coil Holders

The G-10 epoxy/fiberglass coil holders are designed to locate the coil with precision, provide multiple support locations for the flexible coil against gravity and magnetic forces, and separate the coil from other surfaces to prevent abrasion to the coil insulation and reduce the danger of arcing. The holders were constructed in two stages. The mount is a simple rectangular block, with two tapped holes drilled through. The bolts that clamp the TF coil cases shut have their nuts removed, and instead screw into the mount. This allows the mount to provide the clamping force previously provided by the nuts, while also precisely positioning the holder into the machine-based coordinate system. The mounts all attach to the 7th and 8th bolts as counted from the topmost bolt in a counterclockwise direction. A drawing of the mount can be seen in Figure A.2, the holder in Figure A.3, and detail as to the mounting location in Figure A.4.

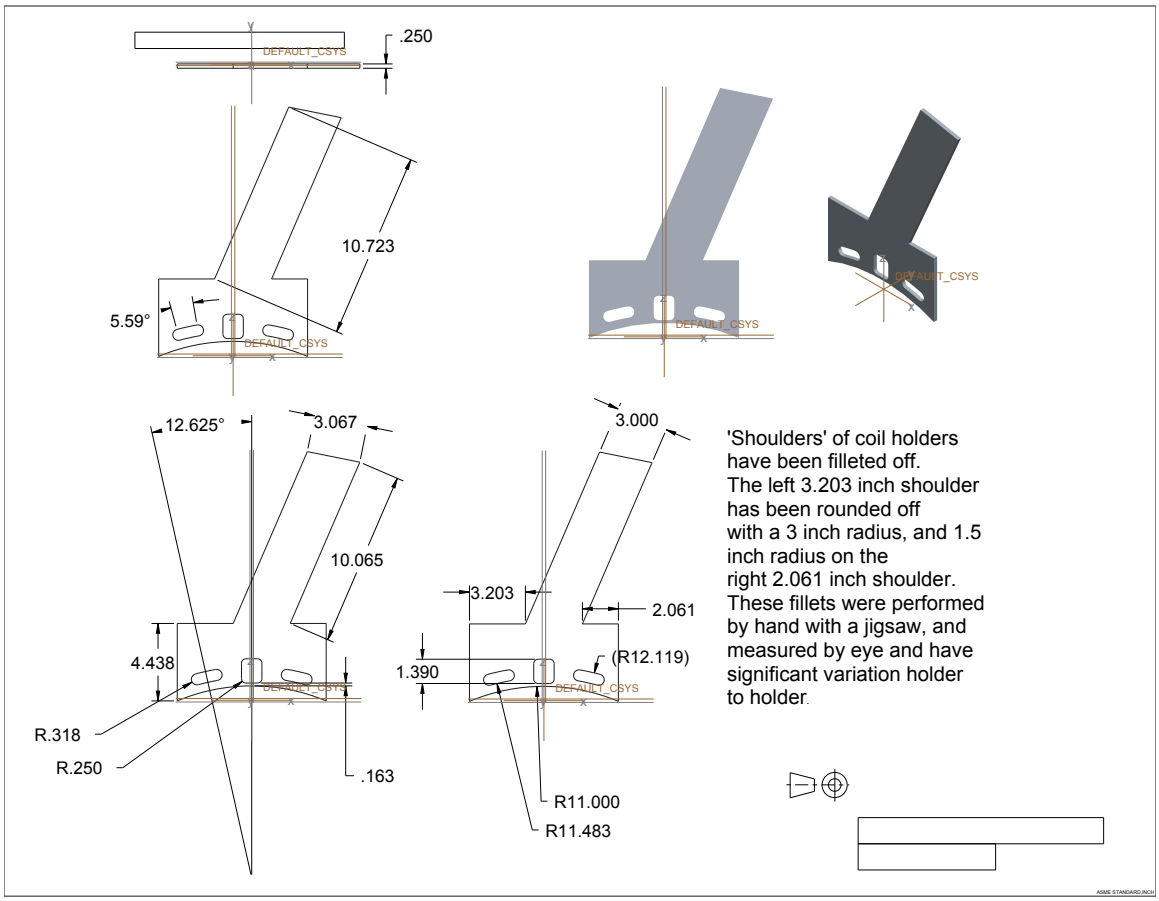

Figure A.3: CAD Drawing of the coil holder. Tapped holes for mounting to TF case not shown.

The mounts have a narrow trench machined into them, that the holder itself slots into. It is cut such that the front face of the mount and holder are flush, as are the top faces of the holder and mount. The holder and mount are fastened using epoxy, with the flush-face constraints ensuring that the holder itself is well referenced to the mount, which is itself located with respect to the machine and plasma by the method of affixation to the TF cases.

The coil is installed by first affixing the holders, then winding the entire length through each hole in each holder in turn. Tight tolerances for the through-holes in the holders would make threading extremely difficult, especially towards the end of the installation, while loose tolerances would allow the coil to move during activation to an unacceptable degree. The compromise reached is for the through holes to have 0.1” of clearance radially, while extending the poloidal extent of the hole itself. The flanking bundle holes extend 0.75” longer in arclength than is needed, while the central through hole is 0.4” taller than required. After the coil was wound, this extra space was taken up

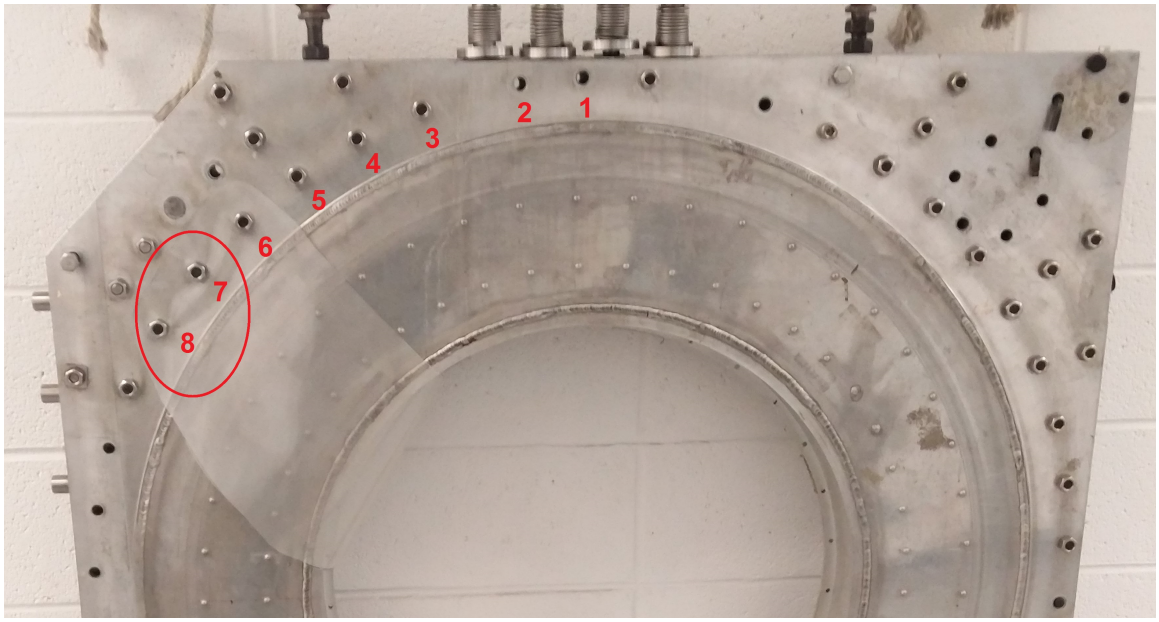

Figure A.4: Photo of spare TF case, showing the bolts to which the holder mounts are attached.

with plastic spacers, fastened with zip ties to the holders.

In addition to the 10 fixed G-10 holders, 10 free-hanging Delrin holders are constructed in two parts. They were designed such that they could be attached to the coil post-installation. Constructed in two parts, they clamp onto the coil and the halves are held together with zipties. Their through holes are precisely cut to the size of the bundles, unlike the fixed holders, and maintain correct interbundle separation.

Appendix B

Electrical Schematics

This Appendix contains circuit diagrams and a partslist of the shaping coil power supply banks, with a brief explanation of the theory of operation for each subsystem.

B.1 The Power Supply

The shaping coil power supply is a two-stage capacitive bank. The bank is switched into the coil using a silicon controlled rectifier, which is itself triggered through a transformer to isolate the high voltage from our control circuitry. The start bank consists of 10 series pairs of 1.5mF capacitors in parallel. The crowbar bank consists of 40 15mF capacitors in parallel. The two banks are themselves connected in parallel with each other through a high-current diode that stands the start bank off from crowbar bank. The start bank is designed to be charged to a voltage of roughly 5 times the crowbar voltage. The diode prevents the start bank from overcharging the crowbar bank, but allows the crowbar bank to begin conducting as the start bank voltage discharges to the level of the crowbar bank, at which point, both banks discharge together.

The capacitance of the start bank combined with the inductance of the shaping coil give an $\frac{1}{\sqrt{LC}}$ frequency of 648 radians/sec. The start bank will conduct for one quarter-cycle, at which point having discharged, the coil current has peaked. At this point the crowbar bank is switched in, and the series resistance of the crowbar bank serves to overdamp the RLC coil-bank system, preventing ringing during normal operation. In the event the crowbar bank is not charged or fails to discharge, a freewheeling diode is installed to shunt coil current away from the banks, and prevent reverse

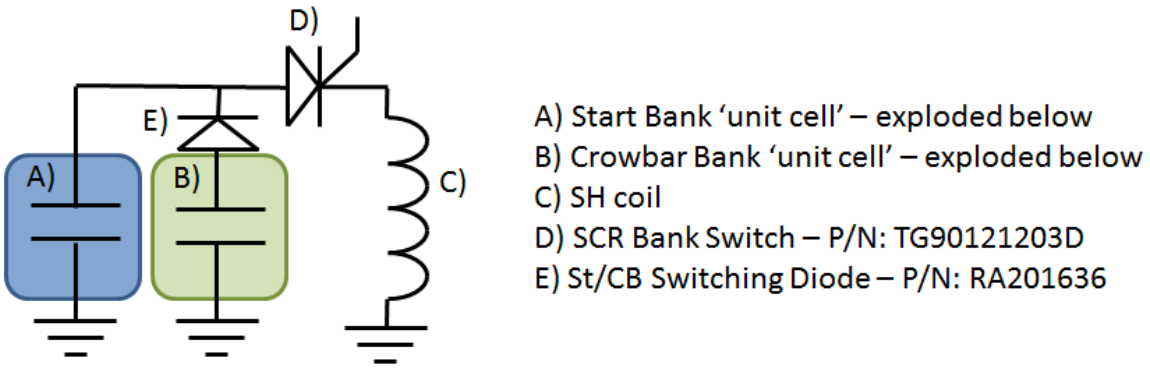

Figure B.1: Top-level schematic of the shaping coil circuit.

biasing.

All capacitors involved are electrolytic, and must therefore be guaranteed against damage from reverse biasing. The crowbar bank has a single diode between hot and ground clamping the bank voltage at ≥ -0.7V. The start bank is constructed of series pairs of capacitors. Both capacitors in the series chain have a diode across the leads to clamp the voltage and prevent either capacitor in the chain from being reverse biased during discharging, as it is possible for the total chain bias to be shared unevenly between each capacitor in the chain.

Both start capacitors in the series chain also have a metal oxide varistor (MOV) with a failure voltage of 500V in parallel across it. The intention is, in the event that a capacitor fails short while the bank is charged above the individual start cap rating of 450V, that the MOV will break down, conduct current around the remaining cap, and allow the bank to discharge to a safe voltage.

Each crowbar capacitor, and start capacitor chain, charges through a fuse to prevent overcurrent, and to remove the capacitor or capacitor chain from the parallel arrangement if one fails short. If the fuse fails, a neon lamp will ignite indicating which capacitor requires service. Both capacitive bank charging power supplies are ground referenced. In order to prevent the supplies being damaged by cross-talk between the two, diodes are placed below the capacitors in each bank that route all charging current through the charging circuit while routing all discharge current away from the power supplies and charging circuit.

The coil current is monitored using a 32 winding/inch Rogowski, integrated using a 22ms RC integrator. The Rogowski was calibrated with a 0.01Ω shunt resistor, which remains in the circuit, unmonitored.

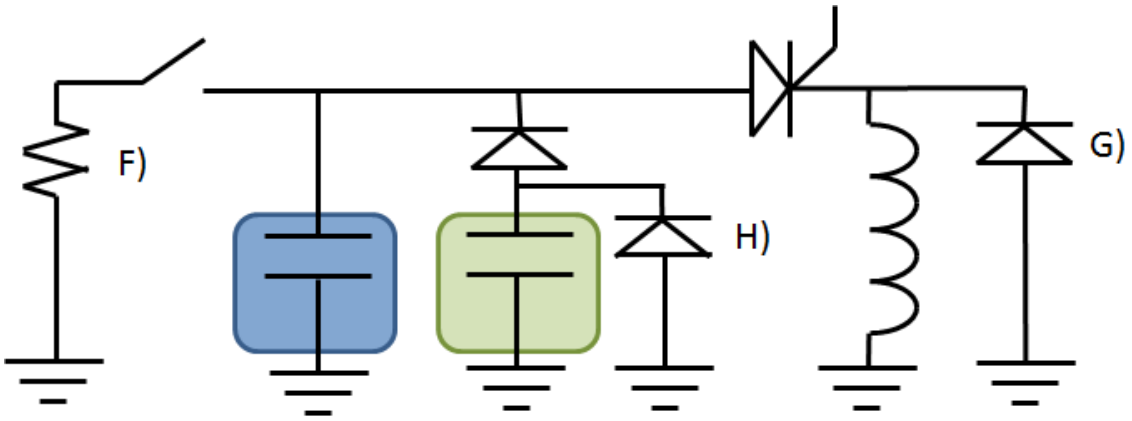

F) Dump Resistor – 35 Ω Oven Heating Element
G) Freewheeling Diode – 70HFR100
H) Crowbar Bank Protection Diode – RG401222XX

Figure B.2: Shaping coil circuit, including circuit-level protection - flywheel diode, dump circuit, and crowbar bank protection diode.

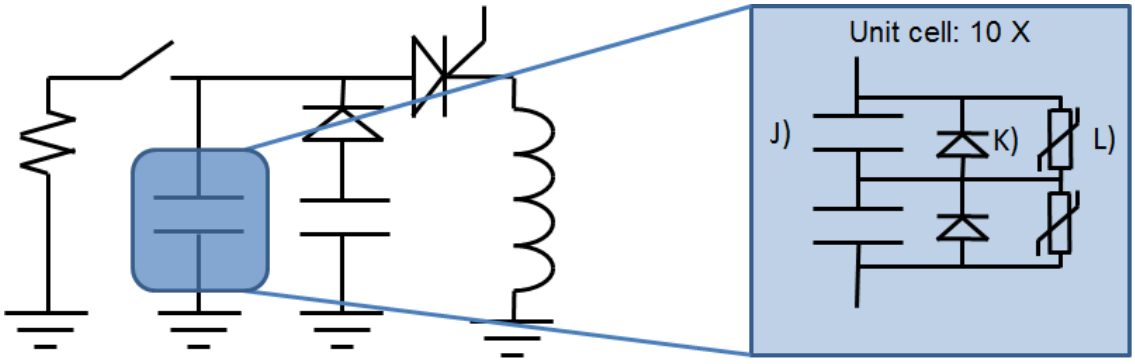

J) 450V, 1.5 mF Capacitor – Mallory HES
K) Start Cap Protection diode – 1N4007
L) Chain Protection MOV – 200621K-ND

Figure B.3: Schematic of a start bank 'unit cell'. 10 such cells are connected in parallel.

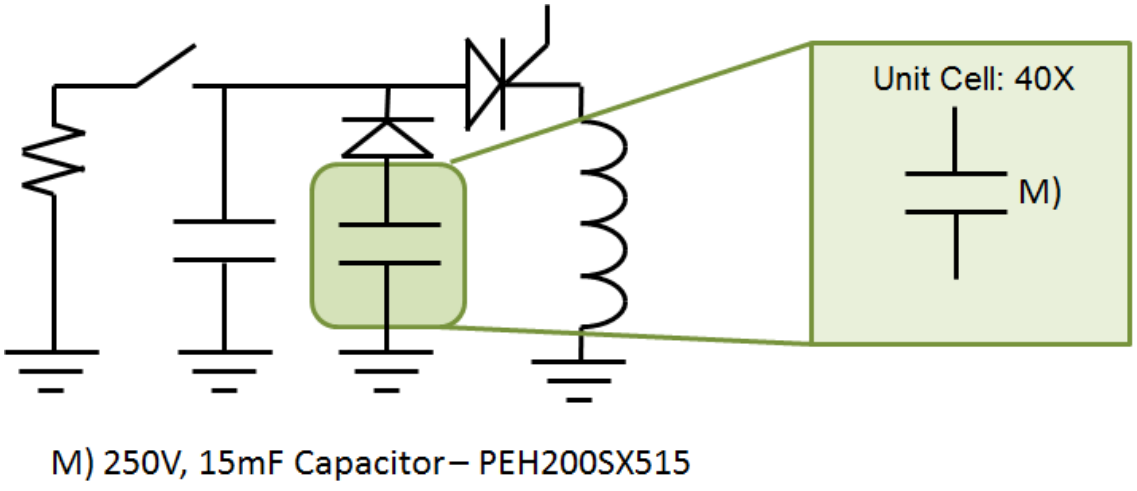

Figure B.4: Schematic of a crwowbar bank 'unit cell'. 40 such cells are connected in parallel.

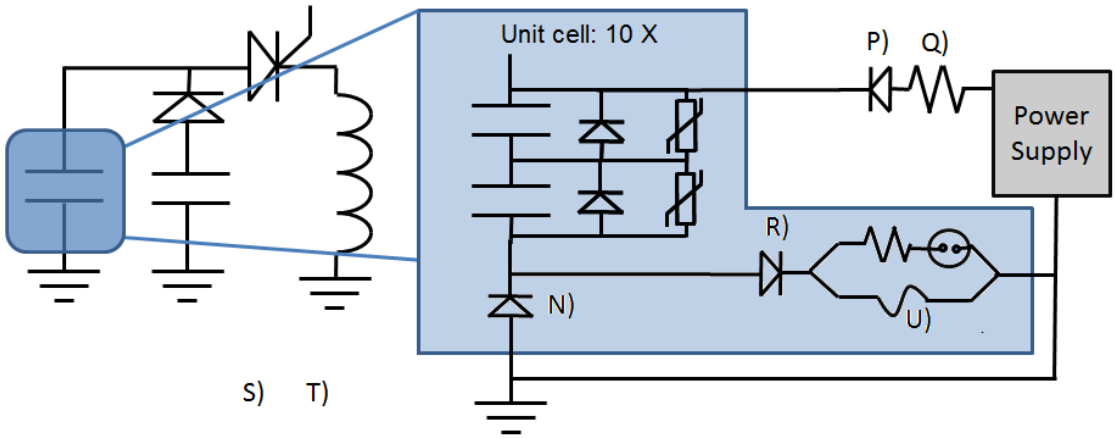

N) Discharge Routing Diode – 40HF100
P) Power Supply Protection Diode – IN4007
Q) Start Charging Resistor – 330Ω 50W
R) Discharge Blocking Diode – IN4007
S) Current Limiting Resistor – 2.7MΩ 0.5W
T) Blown Fuse Indicator Neon – 2ML
U) Charging Fuse – 504-BBS-2/10

Figure B.5: Schematic of a start bank 'unit cell' including current routing circuitry for charging/discharging. 10 such cells are connected in parallel. Only one of each component outside the shaded region.

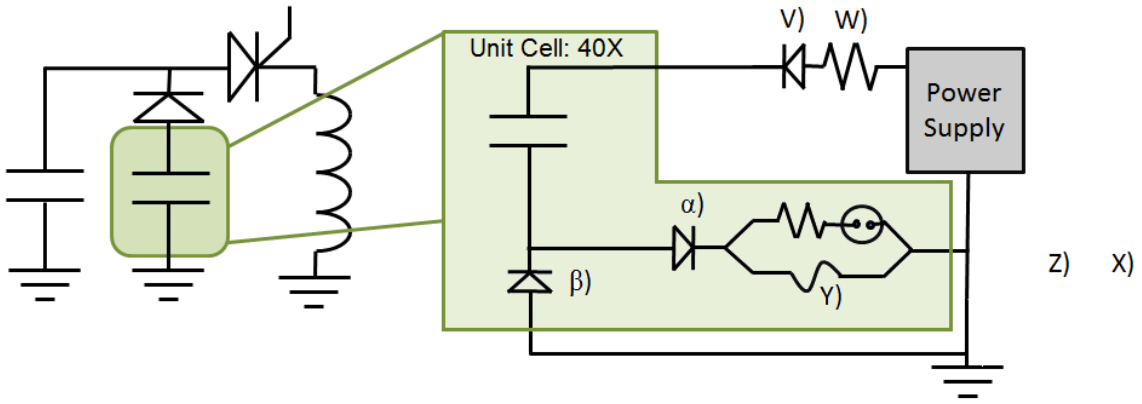

V) Power Supply Protection Diode – 26M3006
W) Crowbar Charging Resistor – 20Ω 300W
X) Blown Fuse Indicator Neon – 2ML
Y) Charging Fuse – 693-001.1007
Z) Current Limiting Resistor – 820kΩ 0.5W
α) Discharge Blocking Diode – IN4007
β) Discharge Routing Diode – 40HF100

Figure B.6: Schematic of a crowbar bank 'unit cell' including current routing circuitry for charging/discharging. 40 such cells are connected in parallel. Only one of each component outside the shaded region.